SANDIA REPORT
SAND2022-17004
Printed December 2022

Final Technical Report: Designing Resilient Communities: Hardware demonstration of resilience nodes concept

Matthew J. Reno, Michael Ropp, Ujjwol Tamrakar, Javier Alvidrez-Hernandez,
Rachid Darbali-Zamora, Adam Summer, Robert J. Broderick.
Sandia National Laboratories

David Lovelady
National Grid

Phil Barker
Nova Energy Specialists

Issued by Sandia National Laboratories, operated for the United States Department of Energy by National Technology & Engineering Solutions of Sandia, LLC.

Available to DOE and DOE contractors from
U.S. Department of Energy
Office of Scientific and Technical Information
P.O. Box 62
Oak Ridge, TN 37831

Telephone: (865) 576-8401
Facsimile: (865) 576-5728
E-Mail: reports@osti.gov
Online ordering: http://www.osti.gov/scitech

Available to the public from
U.S. Department of Commerce
National Technical Information Service
5301 Shawnee Rd
Alexandria, VA 22312

Telephone: (800) 553-6847
Facsimile: (703) 605-6900
E-Mail: orders@ntis.gov
Online order: https://classic.ntis.gov/help/order-methods/

ABSTRACT

As part of the project "Designing Resilient Communities (DRC): A Consequence-Based Approach for Grid Investment," funded by the United States (US) Department of Energy's (DOE) Grid Modernization Laboratory Consortium (GMLC), Sandia National Laboratories (Sandia) is partnering with a variety of government, industry, and university participants to develop and test a framework for community resilience planning focused on modernization of the electric grid. This report provides a summary of the section of the project focused on hardware demonstration of "resilience nodes" concept.

CONTENTS

LIST OF FIGURES

LIST OF TABLES

ACRONYMS AND DEFINITIONS

Abbreviation	Definition
CCT	critical clearing time
CERTS	Electric Reliability Technology Solutions
CT	current transformer
DETL	Distributed Energy Testing Laboratory
DOE	Department of Energy
DOE OE	DOE Office of Energy
DRC	Designing Resilient Communities
DUT	device under test
EMT	Electromagnetic transient
EUT	equipment under test
GFLI	grid-following inverters
GFMI	grid-forming inverters
GFOV	ground fault overvoltage
GMLC	Grid Modernization Laboratory Consortium
HIL	hardware-in-the-loop
NARUC	National Association of Regulatory Utility Commissioners
PUC	Public Utility Comission
PV	photovoltaic
SAG	Stakeholder Advisory Group
Sandia	Sandia National Laboratories
SUNY	State University of New York
TOC	time overcurrent
U.S.	United States

EXECUTIVE SUMMARY

The "Designing Resilient Communities (DRC): A Consequence-Based Approach for Grid Investment" project, funded by the U.S. Department of Energy's (DOE) Grid Modernization Laboratory Consortium (GMLC), sought to enable more resilient communities through consequence-based approaches to grid investment planning through two related goals. First, in collaboration with key stakeholders, to design a framework that aligns community resilience and grid investment planning through a novel consequence-based approach. Second, through iterative implementation and refinement of the framework and analysis of attendant technology, policy, and market dynamics, to establish a clear, actionable path toward widespread adoption of this consequence-based resilience planning approach among electric utilities, municipal governments, and energy regulators. These goals were realized through project workstreams organized under four tasks:

- Task 1: Development of a framework for alignment of community resilience planning and grid investment planning
- Task 2: Implementation and validation of the Resilient Community Design Framework
- Task 3: Investigation of alternative regulatory frameworks and utility business models for incentivizing efficient resilience investments and monetizing resilience benefits
- Task 4: Hardware demonstration of "resilience nodes" concept

This report summarizes Task 4 of the DRC project, focusing on Hardware demonstration of "resilience nodes" concept .

1. INTRODUCTION

1.1. Motivation

The energy sector is one of 16 critical infrastructure sectors designated in Presidential Policy Directive-21 (PPD-21) [1]. This designation recognizes the criticality of these sectors to the functioning of the United States (U.S.) economy, society, and national security [1]. The electricity subsector has been recognized as particularly critical because of its interdependencies with other critical infrastructure sectors, as depicted in Figure 1 [2, 3, 4].

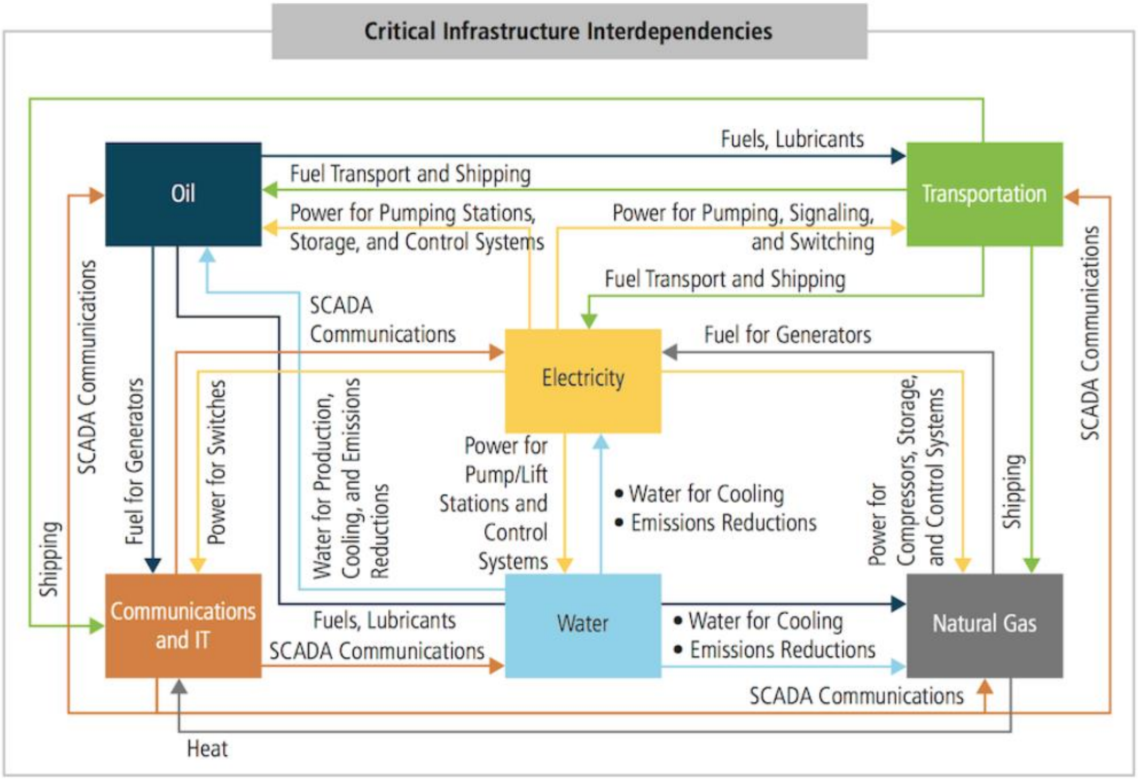

Key critical infrastructure interdependencies represent the core underlying framework that supports the American economy and society. The financial services sector (not pictured) is also a critical infrastructure with interdependencies across other major sectors supporting the U.S. economy.

Acronyms: supervisory control and data acquisition (SCADA).

Figure 1. Electricity System Centrality for Critical Infrastructure Resilience [2]

The consequences of major disruptions to the electric power system—such as Superstorm Sandy, Hurricane Maria, and recent winter storms in Texas—have exemplified its criticality and focused attention on strategies to promote its resilience. Despite substantial interest in the topic of critical infrastructure resilience, definitions vary widely in the literature [5, 6, 7, 8, 9, 10, 11, 12] and among practitioners [13, 4]. This report utilizes the definition of resilience established in PPD-21: "…the ability to prepare for and adapt to changing conditions and withstand and recover rapidly from disruptions" [1]. This definition exemplifies the unique temporal dimensions of resilience, as depicted in Figure 2, which encompasses system performance before, during, and after a disruptive event.

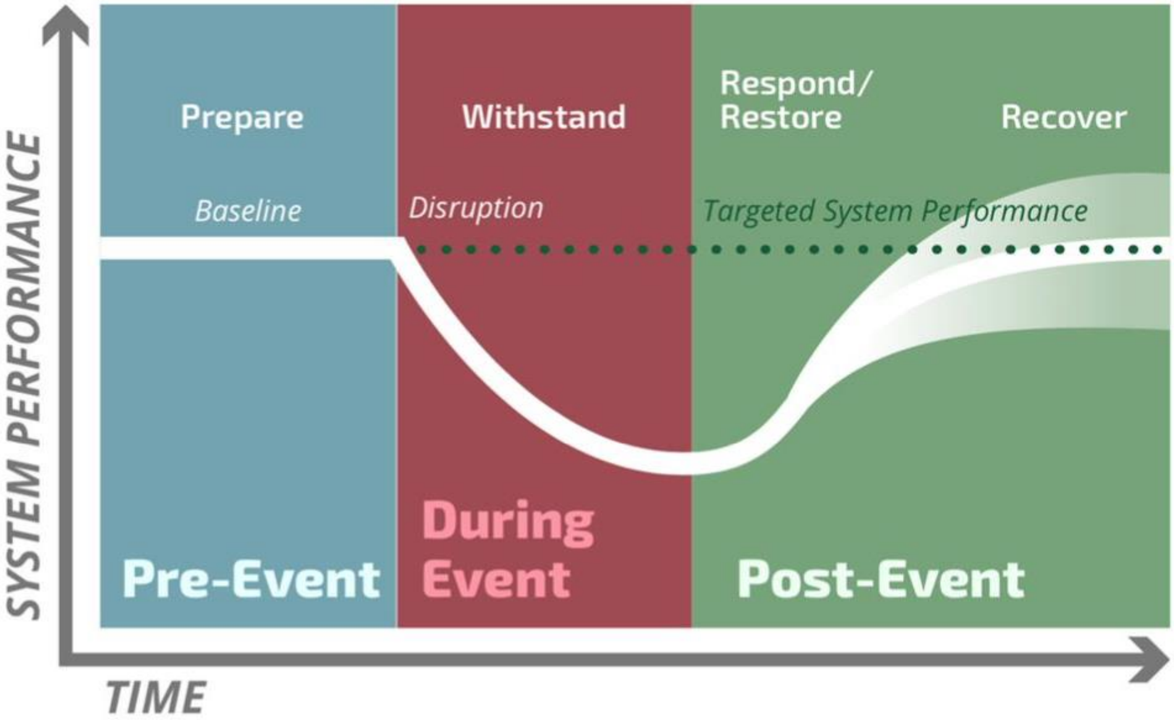

Figure 2. Resilience Curve and Timeline [4]

While there is a growing body of work focused on measuring and enhancing the resilience of the transmission system, strategies to enable distribution system resilience are underexplored. The myriad stakeholders and the diverse market and policy contexts involved in distribution system planning and operation add complexity to the technological and methodological aspects of electric grid resilience planning. In particular, aligning electric grid modernization investment planning with community resilience planning is a key challenge for enabling a more resilient distribution system, and in turn, more resilient communities.

2. DRC PROJECT OVERVIEW

Sandia National Laboratories (Sandia) partnered with a variety of government, industry, and university partners in the development and demonstration of a framework for community resilience planning focused on modernization of the electric grid. To address the gap between community and electric utility resilience planning, the DRC project investigated how coordinated grid investment can support resilient community design and how electric utilities of various configurations can plan for resilience and benefit from resilience investments. This section provides a summary of the DRC project goals, stakeholders, and accomplishments.

2.1. DRC Project Goals

The DRC project sought to enable more resilient communities through consequence-based approaches to grid investment planning through two related goals. First, in collaboration with key stakeholders, to design a framework that aligns community resilience and grid investment planning through a novel consequence-based approach. Second, through iterative implementation and refinement of the framework and analysis of attendant technology, policy, and market dynamics, to establish a clear, actionable path toward widespread adoption of this consequence-based resilience planning approach among electric utilities, municipal governments, and energy regulators. These goals were realized through project workstreams organized under four tasks:

- Task 1: Development of a framework for alignment of community resilience planning and grid investment planning
- Task 2: Implementation and validation of the Resilient Community Design Framework
- Task 3: Investigation of alternative regulatory frameworks and utility business models for incentivizing efficient resilience investments and monetizing resilience benefits
- Task 4: Hardware demonstration of "resilience nodes" concept

2.2. DRC Project Stakeholders

Deep collaboration among a broad set of stakeholders was essential to the DRC project's success. As Figure 3 depicts, Sandia engaged a variety of government, industry, and university partners with shared interest and expertise in community resilience planning and electric grid modernization. Sandia formed a Stakeholder Advisory Group (SAG) to inform the development of the Resilient Community Design Framework and to serve as a community of practice for connecting city, utility, and regulator activities focused on resilience and addressing shared challenges in consequence-focused resilience planning. The SAG consisted of stakeholders from municipal governments and electric utilities, spanning multiple regions, regulatory environments, and utility structures. Over the course of the project, the SAG included representatives from six jurisdictions: New York City (ConEdison), Honolulu (Hawaiian Eclectic Company), Norfolk (Dominion Energy), Atlanta (Southern Company), Los Angeles (Los Angeles Department of Water and Power), and Boston (Eversource). In addition, Sandia engaged three sets of demonstration partners to enable the implementation and validation of the Resilient Community Design Framework and the hardware demonstration for the resilience node concept: City of San Antonio and CPS Energy, El Cano Martin Pena Communities, and National Grid. To support framework development and demonstration as well as investigation of alternative regulatory frameworks and utility business models and the hardware demonstration, Sandia also engaged several project partners, including State University of New York (SUNY) at Buffalo, Synapse Energy Economics, Bosque Advisors, Clemson University, and New Mexico State University. Other organizations, such as the National

Association of Regulatory Utility Commissioners (NARUC) and 100 Resilient Cities also collaborated with SAG members and contributed expertise to the project.

Figure 3. Designing Resilient Communities Project Stakeholders

The SAG and other project stakeholders served three critical roles in the DRC project. First, they provided feedback on unique aspects of their operating contexts that enable or discourage alignment of community resilience planning and electric grid modernization. Second, they informed the technical and regulatory solution space for the project and provided research, analysis, and advice to support the establishment of a clear, actionable path toward widespread adoption of this consequence-based resilience planning approach among electric utilities, municipal governments, and energy regulators. Third, they enabled information exchange about emerging technologies that can provide grid resilience and addressed how these technologies can provide community resilience.

In particular, the SAG played an instrumental role in the design, validation, and implementation of the Resilient Community Design Framework. SAG members provided information about the challenges and opportunities their unique jurisdictions and organization faced in grid resilience planning, which helped frame the gap analysis for the framework. SAG members also provided feedback on several drafts of the framework, enabling an iterative and collaborative framework development process. SAG members suggested direction for analysis and designs being performed with demonstration partners, supporting framework validation. Finally, discussions among SAG members, demonstration partners, and project partners facilitated information exchange about emerging methodologies, technologies, and strategies to enhance grid resilience, thereby supporting ongoing implementation of the framework.

3. TASK 4: HARDWARE DEMONSTRATION OF RESILIENCE NODES CONCEPT

Pursuant to Task 4, Sandia and project partners addressed technical challenges in clean resilience nodes and completed a hardware demonstration of adaptive protection on a resilience node. One of the key challenges for clean inverter-based microgrids is the ability to safely protect them [14]-[19]. While distributed energy resource (DER) can impact distribution system protection [20]-[22], there are potential solutions using machine learning [23], traveling wave [24], [25], and adaptive protection [26], [27]. To overcome technical challenges in clean resilience nodes, Sandia collaborated with New Mexico State University on modeling grid forming inverters for protection studies, and on installing, testing, and validating designs using power hardware in the loop for demonstration at Sandia's Distributed Energy Technologies Laboratory (DETL) [28]-[35]. Additionally, Sandia is collaborating with Clemson University on adaptive protection designs for inverter-dominated microgrids, also for demonstration at Sandia's DETL. Sandia is also working with National Grid on a hardware demonstration of adaptative protection on a resilience node. The demonstration seeks to enhance the resilience of the Old Forge and involves a >70-mile microgrid powered by a large battery energy storage system and includes 5 substations in the microgrid, all connected with a 46 kV sub-transmission line.

3.1. Characterizing IBR Contributions Under Faults

Developing inverter simulation models is a crucial step in understanding and characterizing their dynamics under abnormal operating scenarios such as faults or phase jumps. Of particular interest are the inverter current and voltage variation contributions during such scenarios. The first approach to develop the simulation models was to perform experimental tests using commercially available inverters. The experiments were focused on faults and voltage phase jumps.

3.1.1. Experimental fault tests for grid-forming and grid-following inverters

Experimental tests were performed on grid-forming inverters (GFMIs), which are inverters that regulate their own voltage and frequency; and grid-following inverters (GFLIs), which are inverters that synchronize to the utility frequency reference and inject real and reactive power by varying their phase angle and voltage amplitude respectively. In order to gain insights into their dynamic behavior under unbalanced load and fault scenarios, two GFMIs were evaluated, with one being transformerless, and the second being a transformer-based device. While dynamic response of GFLI is much better understood, test results for a transformerless GFLI are also shown as a comparison to the GFMIs. These are referred to as equipment under test (EUT) #1, #2, and #3, respectively. Table 1 lists the correspondent characteristics of the aforementioned EUTs.

Table 1. Characteristics of equipment under test.

Device	Control Type	Nominal Voltage (V L-N)	Rated Power (kVA)	Transformerless? (Y/N)
EUT #1	GFMI	120	9.0	Y
EUT #2	GFMI	277	100.0	N
EUT #3	GFLI	277	24.0	Y

Three different test setups were utilized; the first two for the GFMIs in a stand-alone mode, and the last for GFLI comparison. The GFMI testbed used a delta or wye load bank as depicted in Figure 4(a) and Figure 4(b), respectively. For EUT #1, a 24 kW 120 Vdc battery simulator was used, whereas for EUT #2, a 100 kW 150-1200 Vdc battery simulator was used. The GFLI testbed utilized an Ametek RS-90 grid simulator/power amplifier and an Ametek TerraSAS photovoltaic (PV) simulator as the input DC source. The grid simulator was set for 90kVA, with a maximum voltage of 300 V L-N, and the PV simulator was set for 1000 Voc, 100 Asc. The GFLI testbed is depicted in Figure 4(c).

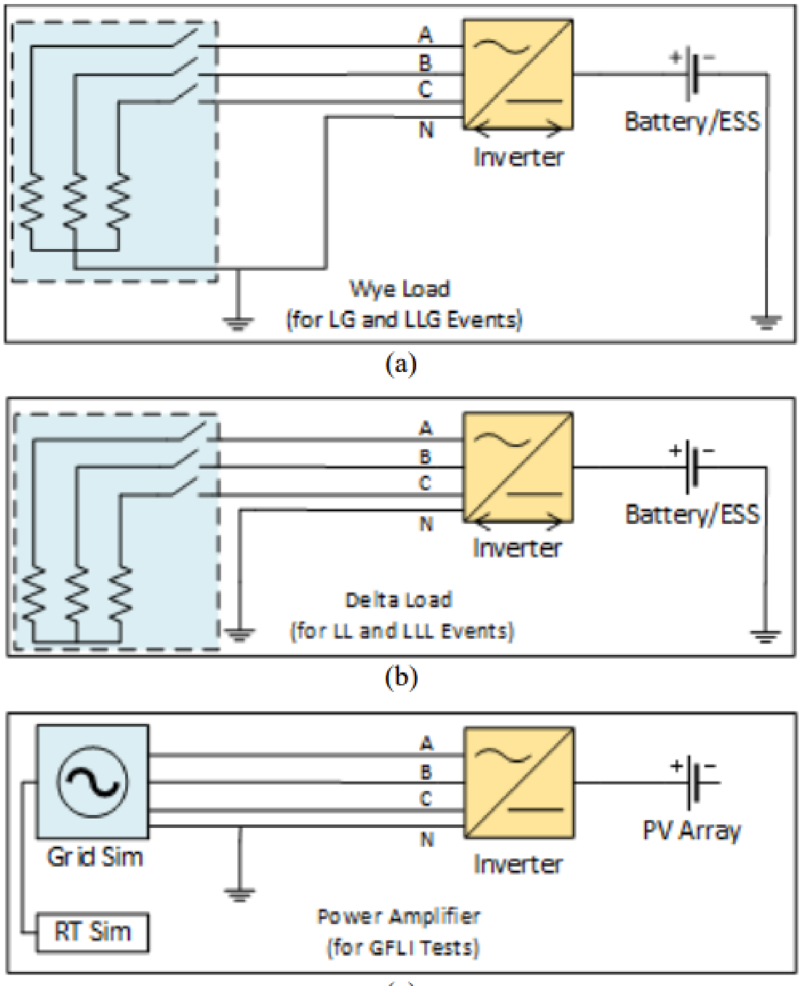

(a)

(b)

(c)

Figure 4. Fault test configurations. (a) GFMI LG and LLG tests, (b) GFMI LL conditions and (c) All GFLI conditions

EUT #1 is a commercial GMFI composed of three individual single-phase inverters connected in grounded wye configuration and tied together through a control scheme to have a master device and two slaves at ±120 degrees from the master reference. EUT #1 was first tested under line to line fault (LL) events up to resistive faults of 9 p.u., as seen in Figure 5(a). The inverter provides both positive and negative-sequence current components to the fault. Notice also that the inverter clips the fault current waveforms as a mechanism to protect the internal circuitry of the device, and the main reason the current waveforms lose their sinusoidal shape during faults. With the negative-sequence current confirmed to be produced by EUT #1, the inverter was subjected to line to ground fault (LG) resistive faults up to 6 p.u. The results of this LG test are shown in Figure 5(b), where all the magnitudes of the current sequence components are equal, which is also the case for traditional power systems fault analyses involving rotating synchronous machines. For a final test, EUT #1 was placed under a line to line to ground fault (LLG) load of 3 p.u. as depicted in Figure 5(c), with the inverter contributing the proper magnitudes of positive-, negative- and zero-sequence currents. Thus, it can be confirmed that this inverter demonstrates similar fault characteristics (although not fault magnitude) to traditional rotating machines and that conventional overcurrent negative-sequence protection schemes could possibly be used.

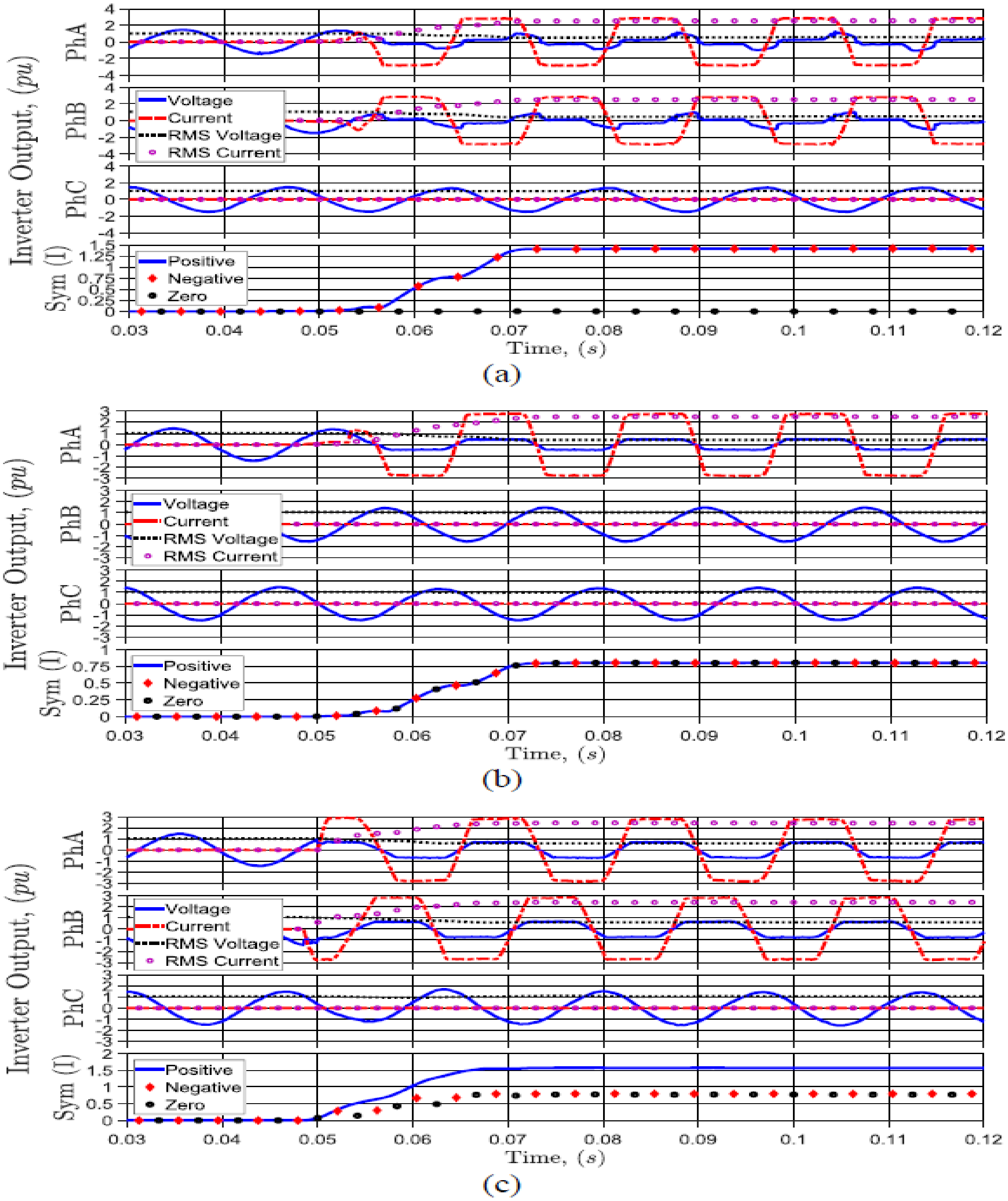

(a)

(b)

(c)

Figure 5. EUT #1 Results During (a) 9 p.u. LL Load, (b) 6 p.u. LG Load, (c) and 3 p.u. LLG Load

EUT #2 is a true three-phase inverter with a nominal voltage of 380 V LL and utilizes a delta to wye transformer (380 V LL to 480 V LL/277 V LN) placed between the inverter and the fault, with the inverter on the delta side. The inverter was rated for 100 kVA.

EUT #2 was put through a 0.75 LG load. While expecting to see positive-, negative-, and zero sequence current components on the wye side of the transformer, it was not expected to see any zero-sequence fault current contribution on the delta side, since such a component is "trapped" inside the delta configuration. From Figure 6, it can be seen that this is the case. EUT #2 outputs both positive and negative-sequence currents but did not supply any zero sequence current. Thus, the transformer is supplying the zero-sequence current. The harmonic content shown in the traces in Figure 6(b) is attributed to the fact that the delta side is directly connected to the inverter output, and thus, some of the switching noise is present. Notice how the transformer filters out much of this noise on the traces from the wye side depicted in Figure 6(a).

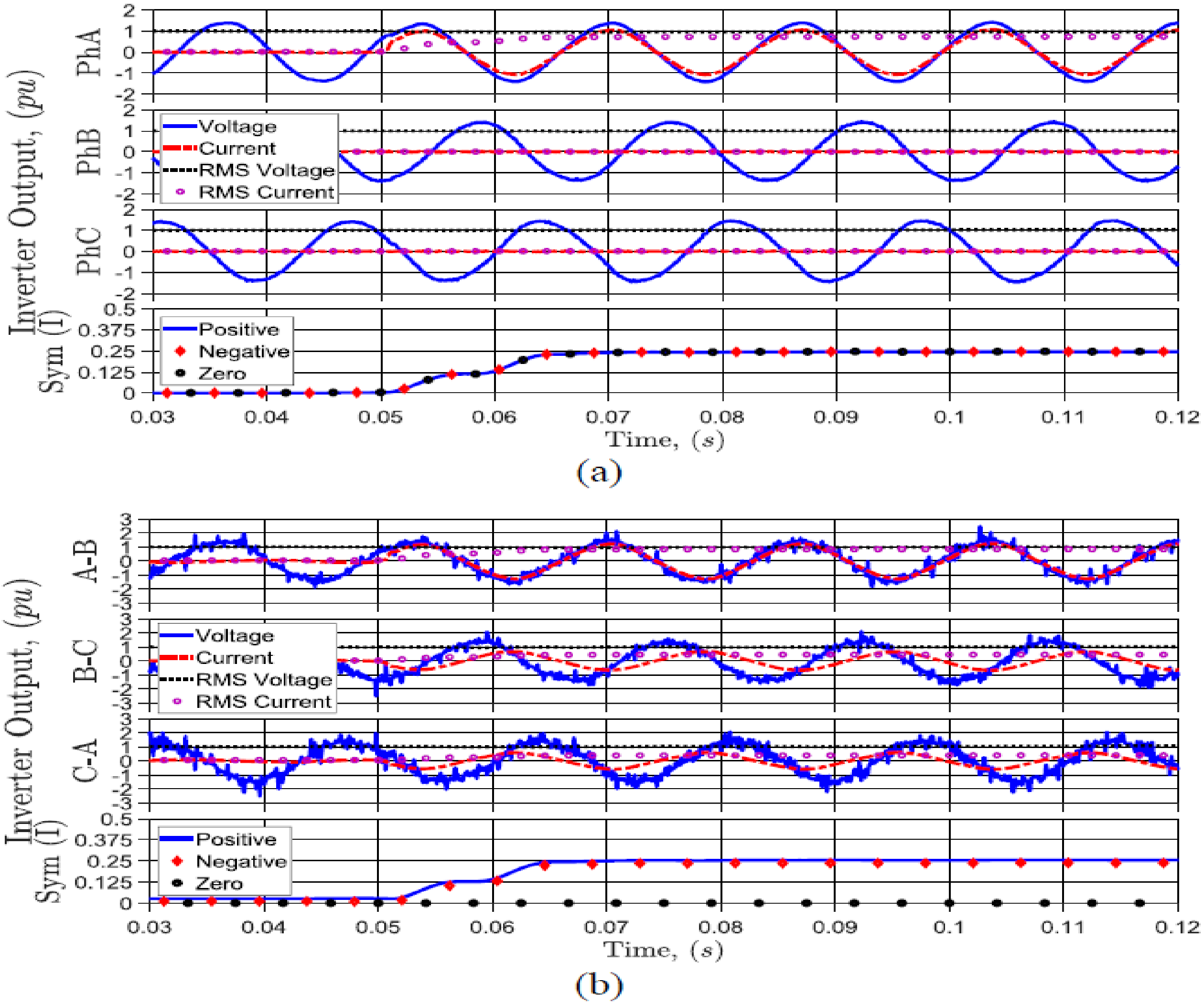

Figure 6. EUT #2 Results During 0.75 p.u. LG Load. (a) Wye Side of Transformer and (b) Delta Side of Transformer

Lastly, a 1 p.u. LLG resistive load was applied to EUT #2, as depicted in Figure 7. On the wye side of the transformer the positive-, negative-, and zero-sequence components of the current are in accordance to that theorized in synchronous machines analyses. Measurements were not taken on the delta side of the transformer as it can be assumed that the inverter will not supply zero-sequence current to the transformer from the results found from the LG load test.

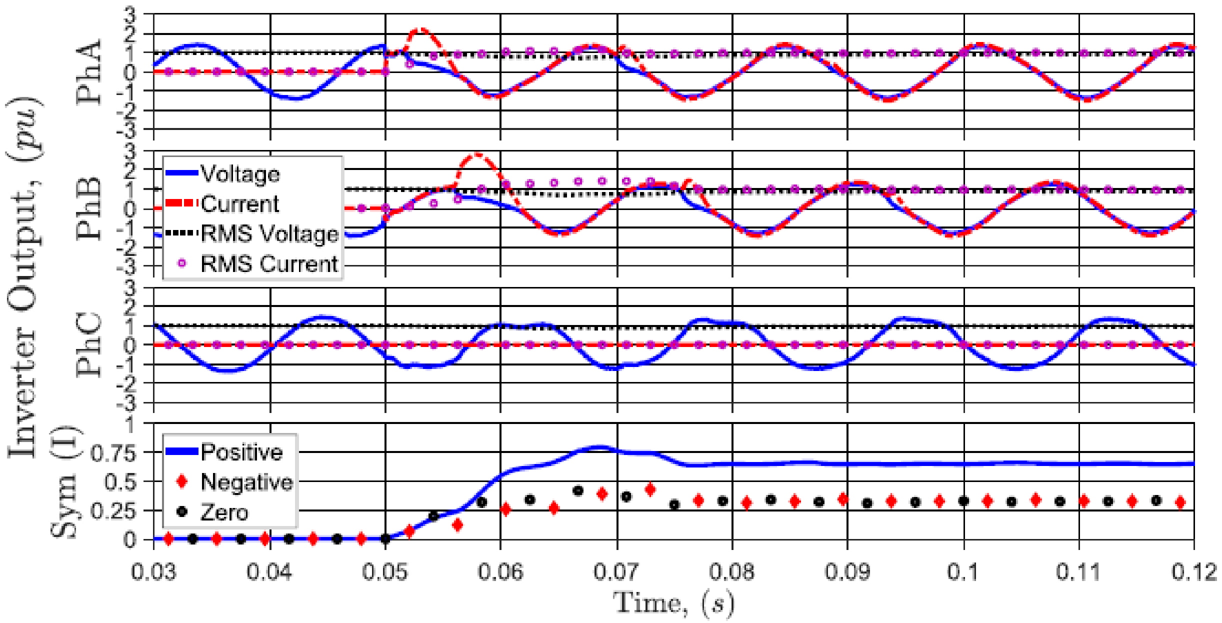

Figure 7: EUT #2 Results During 1 p.u. LLG Load (Wye Side of Transformer)

EUT #3 is a 24 kVA three-phase PV inverter with a nominal voltage rating of 480 V L-L/277 V L-N. For all tests the PV simulator was set to a string condition with Voc of 480 Vdc, Isc of 10Adc, and a fill factor of 0.72. Furthermore, a real-time simulator was used to create a phase shift with an analog signal, which was used to control the grid simulator in amplifier mode to enable emulation of a LL event. Figure 8(a) shows an event such that phase A and B were shifted 40 degrees closer to one another, giving a total of only 40 degrees between them. This phase angle shift was selected as it is the maximum shift allowed without the inverter going into momentary cessation.

From the results shown in Figure 5 through Figure 7, it can be inferred that GFMIs can supply both negative- and zero-sequence current components corresponding to those determined from the conventional symmetrical component analyses performed in systems with rotating machines. This is a crucial function as overcurrent protection may not be a reliable method for fault protection as fault current limited inverter-based generation becomes more prevalent. Moreover, it was confirmed that with the utilization of a delta-wye transformer, a GFMI only needs to provide positive- and negative-sequence components, as the transformer provides the zero-sequence component source, this allows for simpler control schemes than the ones for inverters with zero-sequence controls.

On the other hand, GFLI provides little to no negative- or zero-sequence components during fault events. This is due to the nature of these inverters operating as near ideal current sources, providing a balanced output independent of the voltage reference. The control schemes do not allow them to override their commanded output current, even when the phase power is significantly less than rated or available power. Moreover, when the voltage shifts out of phase, the current is controlled to maintain a 120 degree angle between phases, and thus only allows for the sourcing of positive-sequence current.

To enable a full inverter-based distribution system or microgrid, decisions have to be made of how unbalanced the system can be and what type of fault characteristics are required. This will determine the aggregate makeup for GFLI vs GFMI devices to be implemented on the system. With the lack of unbalanced capabilities from current GFLIs, devices like GFMIs become more crucial to produce this unbalanced power, unless grid following devices are implemented with new control schemes. Furthermore, a higher penetration of GFMIs allow for the system to have a high inertia behavior, and greater stability than systems with higher GFLI penetration.

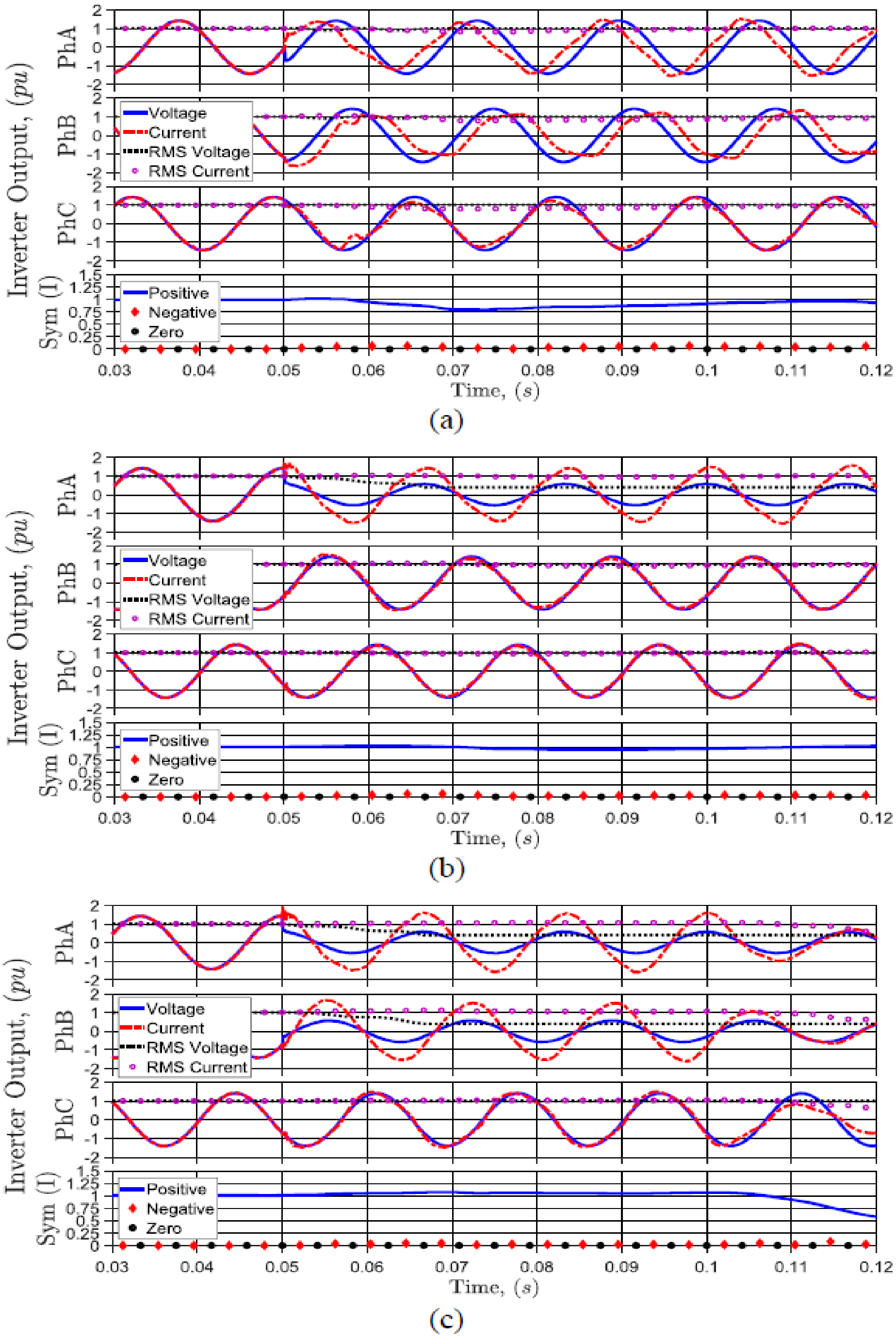

Figure 8. EUT #3 Results During 40 Degree Two Phase Shift (a), 60% Single Phase Sag (b), and 60% Two Phase Sag (c)

3.2. National Grid Resiliency Criteria and a Central Adirondack Resiliency Microgrid Project

In order to improve the resiliency of National Grid's electric grid, National Grid collaborated with Sandia on two aspects of resiliency 1) the creation of a new resiliency distribution system planning criteria and 2) simulations and modeling for a proposed microgrid in the central region of the Adirondacks State Park in Upstate New York, known as the Central Adirondack Resiliency Microgrid Project.

The Resiliency Planning Criteria was developed as part of an overhaul of the National Grid Distribution Planning and Asset Management Criteria document. Whereby this document provides the hard thresholds for planners to conduct system studies and compare results with the Criteria to determine whether system upgrades/solutions are needed. While National Grid has made significant investments in resiliency in recent years, in particular in storm hardening following Irene and Sandy hurricanes, there was a need to bring resiliency into regular planning activities to identify solutions for areas that suffer from major outage events on a frequent basis.

Sandia worked with National Grid to field validate technologies that enable distributed, clean resources to improve reliability (minor events) and resiliency (major events) for the local communities that would be supplied by the Microgrid. The overall objective is to design and demonstrate that a community resilience node can be implemented with a clean inverter-dominated battery forming island protection and control. Inverter-based energy storage can create new problems for the grid, especially around power system protection, so by designing new protection schemes, this effort is overcoming technical challenges and clearing hurdles for clean resilience nodes.

3.2.1. National Grid's Resiliency Planning Criteria

As part of this DRC project, National Grid presented its draft version of the Resiliency Planning Criteria during a working session with the key parties of this Sandia-led DRC project. Subsequent feedback was provided and incorporated into the final version provided below.

Criteria:

Major storm impacts are omitted from reliability metrics in accordance with state-specific requirements. As storms become more frequent and severe considering recent trends and expected climate change impacts, more focus is to be given to the resilience of the grid to withstand and recover from more extreme events.

The following criteria should be considered when the Company is planning feeder or substation upgrades of greater than $1 million in the area of concern.

A resiliency project shall be developed for 15 kV class and above lines and stations that have one or more protection devices with a total ten-year historical customer hours interrupted (CHI) event value greater than the CHI Outage Limits specified in Table 2 below for events lasting greater than 24 hours.

Table 2. CHI Outage Limits for Ten Years per region

MA	NY	RI
156,000	50,100	113,400

A station flood mitigation analysis shall be conducted for stations that are within the 100-year flood zone, whereby the area planner will consult with Civil Engineering to determine the possible flood water levels, assets at risk, and potential mitigation measures. This risk will be compared against the costs of the alternatives to determine if a project is required.

Threats:

- Weather impacts and trending towards longer duration and more frequent events
- Physical attacks
- Cyber security events
- Transmission supply weaknesses

Goals:

- Implement Resiliency projects to bring areas under the CHI threshold and back within criteria. Whereby solutions should consider the time periods specified in the IEEE PES-TR65: Manage disruption, quickly respond, fully recover and adapt
- Improve customer experience and satisfy increasing expectations

Metrics:

- Benefit-Cost Analysis
- Improvements in resiliency over time

3.2.2. Central Adirondack Resiliency Microgrid Project

The Central Adirondack area is shown in Figure 9 below and is an area that suffers from repeated outages due to its location in a rural and heavily treed area that has only one long (~100 miles) radial 46 kV sub-transmission supply. The radial nature of the 46 kV line means that any outages anywhere on the line cause all downstream stations from the fault to lose power. The five distribution feeders fed from this 46 kV sub-transmission line are often listed on National Grid's Worst Performing Feeder list. National Grid has continued to evaluate routes for an alternative secondary source line into this area to improve reliability, but all have been too expensive for customers and/or to difficult to site within a State Park.

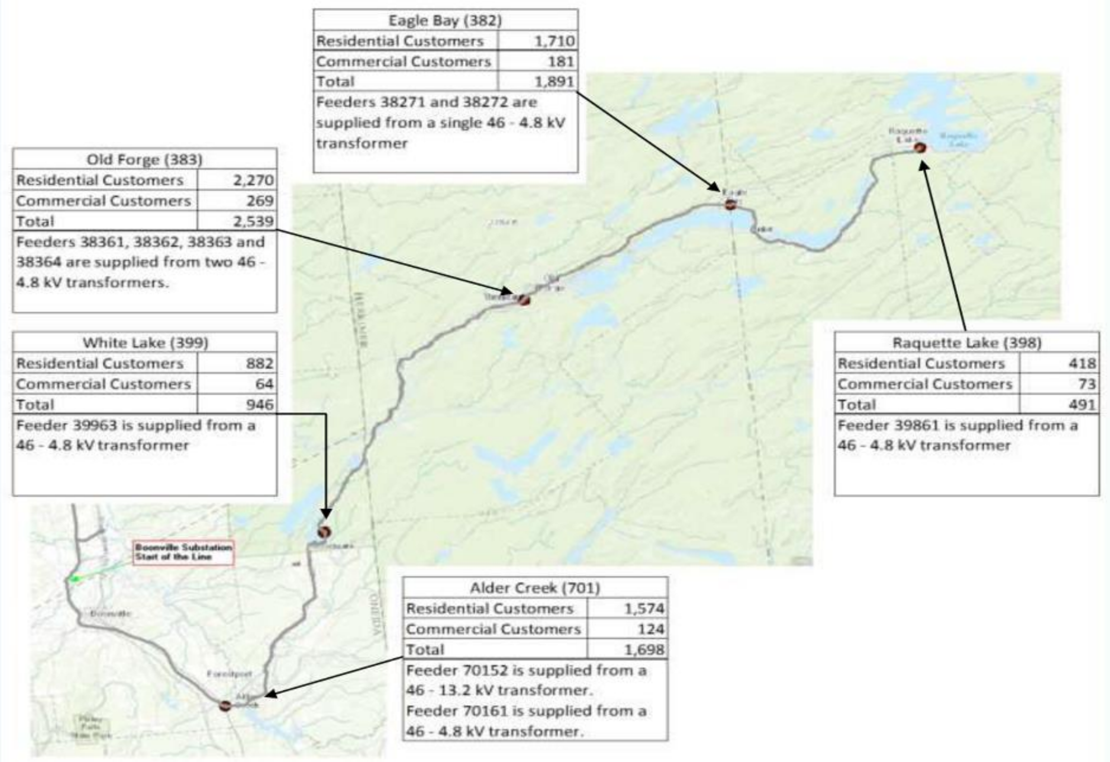

Eagle Bay (382)	
Residential Customers	1,710
Commercial Customers	181
Total	1,891

Feeders 38271 and 38272 are supplied from a single 46 - 4.8 kV transformer

Old Forge (383)	
Residential Customers	2,270
Commercial Customers	269
Total	2,539

Feeders 38361, 38362, 38363 and 38364 are supplied from two 46 - 4.8 kV transformers.

White Lake (399)	
Residential Customers	882
Commercial Customers	64
Total	946

Feeder 39963 is supplied from a 46 - 4.8 kV transformer

Raquette Lake (398)	
Residential Customers	418
Commercial Customers	73
Total	491

Feeder 39861 is supplied from a 46 - 4.8 kV transformer

Alder Creek (701)	
Residential Customers	1,574
Commercial Customers	124
Total	1,698

Feeder 70152 is supplied from a 46 - 13.2 kV transformer.
Feeder 70161 is supplied from a 46 - 4.8 kV transformer.

Figure 9. Old Forge demonstration site

One alternative that would be cost-effective and easy to site compared with bringing an alternate supply line to the area would be to site a battery energy storage system (BESS) that can operate this section of the system as a microgrid. Following an request for proposal (RFP) process, a Li-ION battery solution that can power the whole system downstream of the Alder Creek substation (4 substations, 46 kV sub-transmission line, and 8 feeders) shown in Figure 10, was selected, with the ability to separate from the bulk grid to form an islanded microgrid following an outage anywhere along the 46 kV line.

The battery energy storage system (BESS) will have two major operating modes of grid-parallel mode and microgrid mode. In grid-parallel mode, up to 20 MW/25MVA will be provided into the 46 kV line for the bulk power system support vis ISO power market transactions. In microgrid mode, the BESS will support the surrounding area, including several distribution substations. While the maximum load of the microgrid may be up to 20 MW/25 MVA on peak loading days, most of the time while in microgrid mode it would be far less than this. The load duration curve for the region shows that such loading is needed less than a few percent of the time on certain holiday weekends. The vast majority of the time the microgrid peak load is likely less than 12 MW. Given the fact that the BESS has up to 40 MWh of stored energy, it can offer up to nearly 2 hours of islanded operation at peak load (if fully charged at the time of microgrid creation) and more practically at least 4 hours during or much more during off-peak load conditions.

The microgrid is not designed to have a seamless transition. During an event, there will be several minutes of outage as the system switchgear isolates the microgrid from the bulk system and the system is reconfigured for microgrid mode. The system may be able to seamlessly transition back to grid parallel mode from microgrid following the restoration of bulk power to the region.

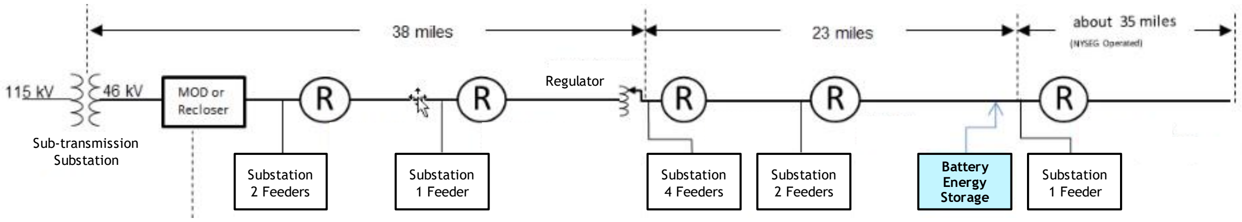

Figure 10. Old Forge area simplified diagram

The sub-transmission 46 kV line running through this area is generally fed from the West from a 115 kV substation, but as seen in Figure 11, in island mode, the system will be fed from the BESS on the East side of the microgrid. This means that during the microgrid mode transition, the current flow direction and the fault current magnitudes will change. An adaptive protection solution is proposed that will change settings depending on if the system is grid-connected or not so that it will remain protected with the lower fault currents provided by the battery on the East side than otherwise seen when connected to the bulk grid. To derive such an adaptive protection solution detailed modeling and simulations of the battery, local electrical grid, and existing protection schemes were required to aid the design and feasibility of this technically complex project.

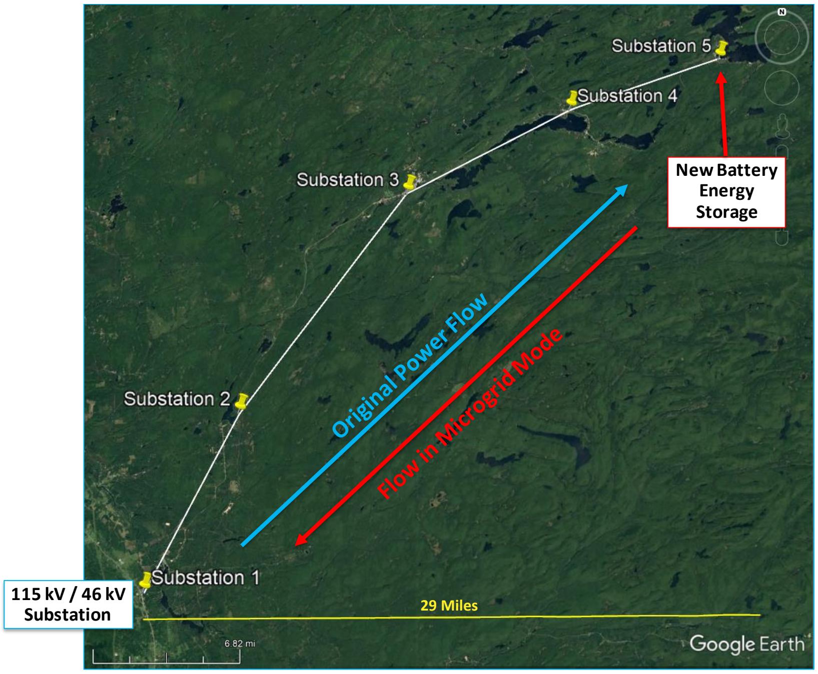

Figure 11. Proposed Old Forge microgrid

3.2.3. *Design Process Overview*

Inverters have a unique dynamic response to faults, as discussed in Section 3.1, with an initial spike from the filter capacitor, transients during control actions, and then steady-state fault current determined by the controls and current limiter. Common utility planning software for protection (such as CAPE or ASPEN software) cannot model those dynamics, especially for islanded systems. This leads to simulation studies being performed in electromagnetic transient (EMT) simulations, as discussed in Section 3.3. Using these EMT simulations, a grounding study is performed in Section 3.4 to determine the effective grounding requirements based on peak voltage during single-line-to-ground faults. The microgrid resilience node is designed to restart and power up the surrounding communities under a loss of power. This black start process is studied in Section 3.5. Next, the results from simulations of different faults around the microgrid in Section 3.7 are used to design the adaptive protection system in Section 3.8. Finally, the system is incorporated in Opal-RT in Section 3.9 for hardware-in-the-loop testing of those relay settings in Section 3.10.

3.3. Building EMT Models of the System

3.3.1. Advantages of EMT Modeling

In order to simulate the impact of fault current from the BESS on the protection system, dynamic simulation of the inverter for both the grid-connected and islanded modes are required. Phasor-based simulation tools are only suitable for system level studies of power systems at fairly large time steps. EMT modeling approaches model most of the relevant dynamics of the power system at small time steps. EMT modeling approaches are especially advantageous in power systems with inverter based resources (IBRs) as it allows for modeling the impact of the switching dynamics and the fast control loops with IBRs that would be neglected with traditional phasor-based modeling approaches. Hence, to accurately study protection systems, stability, and impact of control design of IBRs EMT modeling approaches are essential.

3.3.2. Conversion to PSCAD

The utility model was converted into PSCAD software to enable dynamic simulation in presence of BESS. Model parameters such as line impedances, loads, transformer parameters, etc. were extracted from utility models available in other power system simulators such as PSS/E, ASPEN and CYME. The transformer parameters were supplemented with data from the transformer nameplates as well. The provided PSS/E models did not include the distribution system protective devices. The distribution systems were added into the PSCAD model by extracting information from CYME for the feeder topology, recloser locations, and end of the feeder impedance. The initial PSCAD model includes the highest impedance 3-phase location with the load values from PSS/E evenly split between all buses. This approach does not model voltage drop or the actual location of the loads very well. Moreover, this also does not model the imbalance correctly (specifically the ground currents). All the loads in the model were modeled as constant impedance loads. This assumption should not impact the presented results unless there is a significant amount of imbalance in the loads.

3.3.2.1. Validation of PSCAD Models

The PSCAD model was validated through comparison of the single phase and three-phase line-to-ground fault currents with results from APSEN model. In ASPEN, fault studies were performed with zero fault impedance. Fault studies were also repeated in PSCAD with the following settings for the "Three Phase Fault" component from the PSCAD library:

- Fault ON Resistance = 0.0001 ohm
- Fault OFF Resistance = 1.0e6 ohm

It should be noted that during the fault study of a particular feeder all the loads in the feeder were disconnected. This is important in case of the 1LG fault current analysis. In PSCAD, when loads remain connected during the 1LG fault, the zero-sequence circuit is completed by the YG-connected load impedances leading to some zero-sequence currents during 1LG fault. Table 3 and Table 4 shows a comparison of fault currents for the 1LG and 3LG faults in ASPEN and PSCAD.

In general, there was a good agreement in fault currents at all the buses for both 1LG and 3LG cases. For 1 LG case, significant error was observed on the Alder Creek 13.2 kV feeder. The reason for this is not clear at this time. Also, PSCAD shows a nonzero 1LG fault current on the Eagle Bay 4.8 kV bus, where ASPEN shows zero fault current. Theoretically zero fault current would be the expectation here because this is a three-wire system, but the PSCAD model includes phase-ground impedance-load models that provide a zero sequence path, and this is likely the reason for the difference there.

Table 3. Single-Phase LG Fault Current Comparisons (ASPEN vs PSCAD)

Bus Name	Nominal Bus Voltage [kV]	Phase Current [A] (ASPEN)	Phase Current [A] (PSCAD)	% difference
Alder Creek	4.8	0	0	0%
Alder Creek	13.2	2126.8	1473.44	30.7%
Alder Creek	46	966.2	944.75	2.2%
Boonville	46	2831.6	2886.77	-1.9%
Eagle Bay	4.8	0	42.21	
Eagle Bay	46	266.1	263.4	1.0%
Eagle Bay T	46	266.3	263.21	1.2%
East Rock	46	1619	1689.54	-4.4%
Kayuta Lake	46	976.7	894.05	8.5%
Old Forge	46	335.9	333.38	0.0%
Alder Creek	4.8	0	0	0.0%
Alder Creek	4.8	0	0	0.0%
Alder Creek	46	211.4	205.1	3.0%
Boonville	4.8	0	0	0.0%
Eagle Bay	46	545.1	541.11	0.7%
Eagle Bay	4.8	0	0	0.0%

Table 4. Three-Phase LG Fault Current Comparisons (ASPEN vs PSCAD)

Bus Name	Nominal Bus Voltage [kV]	Phase Current [A] (ASPEN)	Phase Current [A] (PSCAD)	% difference
Alder Creek	4.8	2469.5	2370.33	4.0%
Alder Creek	13.2	1787.5	1744.77	2.4%
Alder Creek	46	1586.2	1505.29	5.1%
Boonville	46	2801.9	2895.22	-3.3%
Eagle Bay	4.8	2926.5	2769.88	5.4%
Eagle Bay	46	517.7	496.94	4.0%
Eagle Bay T	46	518	497.29	4.0%
East Rock	46	2217.6	2222.07	-0.2%
Kayuta Lake	46	2237.4	1779.71	20.5%
Old Forge	46	1454.7	1448.71	0.4%
Alder Creek	46	643.9	619.71	3.8%
Alder Creek	4.8	3430.3	3102.1	9.6%

Alder Creek	4.8	3364.7	3197.05	5.0%
Boonville	46	404.9	382.3	5.6%
Eagle Bay	4.8	1714	1641.9	4.2%
Eagle Bay	46	998.6	961.8	3.7%
Eagle Bay T	4.8	2198.1	2049.58	6.8%

Model Conversion to MATLAB\Simulink

The utility model was also converted into MATLAB\Simulink for hardware-in-the-loop (HIL) studies. The HIL studies were performed using the real-time digital simulator from OPAL-RT. The RT-LAB software used by the RTDS is only compatible with MATLAB\Simulink. In this section, a brief discussion on the procedure used to translate the PSCAD model into MATLAB\Simulink is described. There are some differences in how the models are represented in MATLAB\Simulink compared to PSCAD and how the parameters are interpreted.

Source Representation:

The bulk power system (BPS) in MATLAB\Simulink is represented by a "Three-Phase Source" block. The positive sequence impedance of the BPS source specified in PSCAD is used to set the "Internal Impedance" parameter of the "Three-Phase Source" block. Next, to model the zero sequence impedance of the BPS from PSCAD, the ground connection of the "Three-Phase Source" block is exposed and an impedance element is connected. This grounding impedance is computed according to the following equation:

$$Z_g = \frac{Z_0 - Z_1}{3}$$

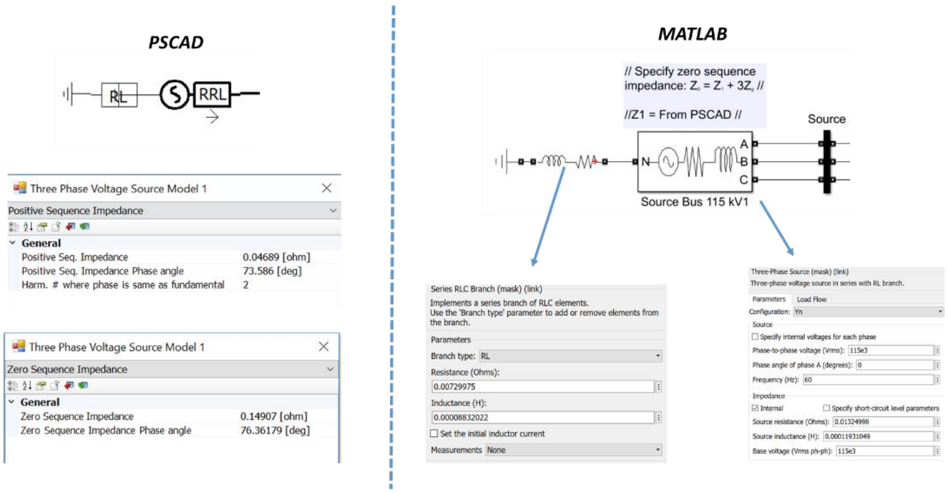

Three Phase Voltage Source Model 1

Positive Sequence Impedance

General

Positive Seq. Impedance	0.04689 [ohm]
Positive Seq. Impedance Phase angle	73.586 [deg]
Harm. # where phase is same as fundamental	2

Three Phase Voltage Source Model 1

Zero Sequence Impedance

General

Zero Sequence Impedance	0.14907 [ohm]
Zero Sequence Impedance Phase angle	76.36179 [deg]

Series RLC Branch (mask) (link)

Implements a series branch of RLC elements.
Use the 'Branch type' parameter to add or remove elements from the branch.

Parameters

Branch type: RL

Resistance (Ohms): 0.00729975

Inductance (H): 0.00008832022

☐ Set the initial inductor current

Measurements None

Three-Phase Source (mask) (link)

Three-phase voltage source in series with RL branch.

Parameters | Load Flow

Configuration: Yn

Source

☐ Specify internal voltages for each phase

Phase-to-phase voltage (Vrms): 115e3

Phase angle of phase A (degrees): 0

Frequency (Hz): 60

Impedance

☑ Internal ☐ Specify short-circuit level parameters

Source resistance (Ohms): 0.01324998

Source inductance (H): 0.00011931049

Base voltage (Vrms ph-ph): 115e3

Line Representation:

The feeder lines are represented using the "Three-Phase Mutual Inductance" block by specifying the positive and zero sequence parameters obtained from PSCAD.

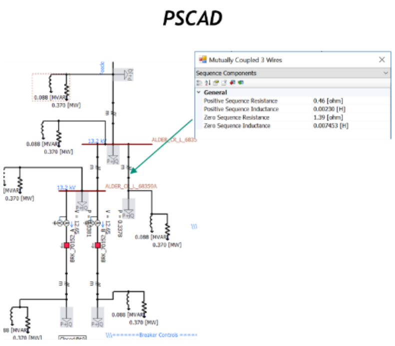

Mutually Coupled 3 Wires

Sequence Components

General

Positive Sequence Resistance	0.46 [ohm]
Positive Sequence Inductance	0.00230 [H]
Zero Sequence Resistance	1.39 [ohm]
Zero Sequence Inductance	0.007453 [H]

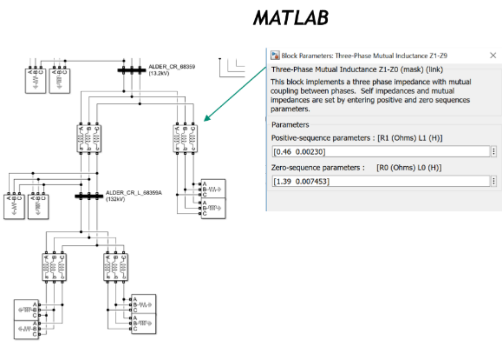

Block Parameters: Three-Phase Mutual Inductance Z1-Z9

Three-Phase Mutual Inductance Z1-Z0 (mask) (link)

This block implements a three phase impedance with mutual coupling between phases. Self impedances and mutual impedances are set by entering positive and zero sequences parameters.

Parameters

Positive-sequence parameters : [R1 (Ohms) L1 (H)]: [0.46 0.00230]

Zero-sequence parameters : [R0 (Ohms) L0 (H)]: [1.39 0.007453]

Load Representation:

The loads are represented using the "Three-Phase Parallel RLC" block. The loads are modeled as constant impedance loads similar to PSCAD. By default, the "Three-Phase Parallel RLC" block exhibits a constant impedance at the specified frequency.

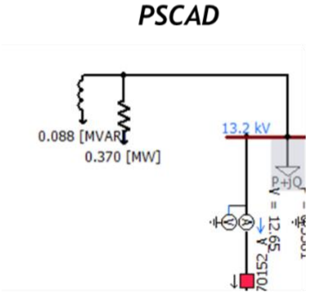

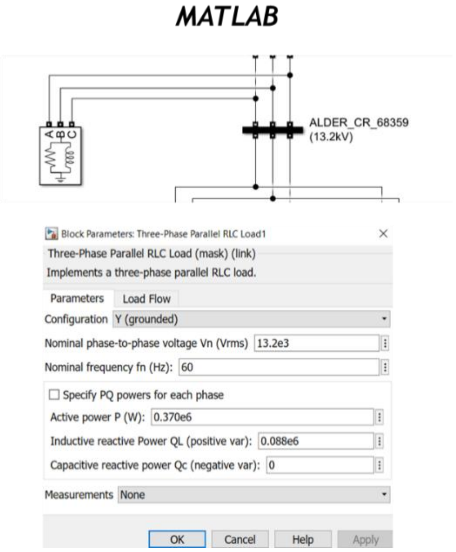

Block Parameters: Three-Phase Parallel RLC Load1

Three-Phase Parallel RLC Load (mask) (link)

Implements a three-phase parallel RLC load.

Configuration: Y (grounded)

Nominal phase-to-phase voltage Vn (Vrms): 13.2e3

Nominal frequency fn (Hz): 60

☐ Specify PQ powers for each phase

Active power P (W): 0.370e6

Inductive reactive Power QL (positive var): 0.088e6

Capacitive reactive power Qc (negative var): 0

Measurements: None

Transformer Representation:

The transformers (including the substation transformer, the regulators on 46 kV line, and the distribution feeder transformers) are represented using the "Three Phase Transformer (Two Winding)" block except for the transformer at the Alder Creek 13.2 kV feeder. This transformer has an additional tertiary winding and is thus represented using the "Three Phase Transformer (Three Winding)" block. The PSCAD parameters "Positive Sequence Leakage Reactance" and "Copper Losses" are used to represent the parameters of the transformer model in MATLAB\Simulink. The "Copper Losses" parameter correspond to the parameters R1 and R2 (resistance of the primary and secondary winding) while the "Positive Sequence Leakage Reactance" parameter correspond to the parameters L1 and L2 (inductance of the primary and secondary winding). The impedances are divided between the primary and the secondary winding based on the turns-ratio of the transformers. For the regulators on the 46 kV line, the impedance are divided equally between the primary and the secondary winding. For all transformers, the magnetizing resistance Rm and inductance Lm are set to high values of 500 p.u. as the "Eddy Current Losses" are set to 0 in PSCAD.

Model Validation:

The MATLAB model was validated through comparison of the single phase and three-phase line-to-ground fault currents with results from PSCAD model. In both PSCAD and MATLAB, fault studies were performed with the following settings for the "Three Phase Fault" component:

- Fault ON Resistance = 0.0001 ohm
- Fault OFF Resistance = 1.0e6 ohm

Table 5 and Table 6 show comparisons of fault currents for the 1LG and 3LG faults in MATLAB and PSCAD. In general, there was a good agreement in fault currents at all the buses for both 1LG and 3LG cases.

Table 5. Single-Phase LG Fault Current Comparisons (MATLAB vs PSCAD)

Bus Name	Nominal Bus Voltage [kV]	Phase Current [A] (PSCAD)	Phase Current [A] (MATLAB)	% difference
Alder Creek	4.8	0	0	0.0%
Alder Creek	13.2	1473.44	1658.71	-12.6%
Alder Creek	46	944.74	930.67	1.5%
Boonville	46	2886.77	3094.15	-7.2%
Eagle Bay	4.8	42.21	0	100.0%
Eagle Bay	46	263.4	260.01	1.3%
Eagle Bay T	46	263.21	260.23	1.1%
East Rock	46	1689.54	1737.84	-2.9%
Kayuta Lake	46	894.05	881.63	1.4%
Old Forge	46	333.38	341.88	-2.5%
Alder Creek	4.8	0	0	0.0%
Alder Creek	4.8	0	0	0.0%
Alder Creek	46	205.1	202.81	1.1%
Boonville	4.8	0	0	0.0%
Eagle Bay	46	541.11	534.31	1.3%
Eagle Bay	4.8	0	0	0.0%

Table 6. Three-Phase LG Fault Current Comparisons (MATLAB vs PSCAD)

Bus Name	Nominal Bus Voltage [kV]	Phase Current [A] (PSCAD)	Phase Current [A] (MATLAB)	% difference
Alder Creek	4.8	2370.33	2343.14	1.1%
Alder Creek	13.2	1744.77	1301.21	25.4%
Alder Creek	46	1505.29	1506.76	-0.1%
Boonville	46	2895.22	2896.91	-0.1%
Eagle Bay	4.8	2769.88	2649.12	4.4%
Eagle Bay	46	496.94	509.25	-2.5%
Eagle Bay T	46	497.29	508.92	-2.3%

East Rock	46	2222.07	2224.14	-0.1%
Kayuta Lake	46	1779.71	1777.56	0.1%
Old Forge	46	1448.71	1451	-0.2%
Alder Creek	46	619.71	646.72	-4.4%
Alder Creek	4.8	3102.1	3189.52	-2.8%
Alder Creek	4.8	3197.05	3042.32	4.8%
Boonville	46	382.3	389.01	-1.8%
Eagle Bay	4.8	1641.9	1131.62	31.1%
Eagle Bay	46	961.8	970.04	-0.9%
Alder Creek	4.8	2049.58	2019.26	1.5%

BESS representation:

The BESS was represented using a manufacturer-specific, code-based, switch-averaged, black-box model of the inverter and a Norton representation of the battery source. A site controller model was also provided. The manufacturer configured the inverter model to give a total AC capacity of 76.3 MVA at 480 V_{rmsLL}. Three versions of the inverter model were provided, corresponding to three different inverter control modes: a standard grid-following model using a phase-locked loop (PLL) for line synchronization and controlling the inverter P and Q injection into the grid; a grid-forming mode that regulates V and f using droop controls; and a synthetic inertia mode (for on-grid use) in which the inverter's behaviors are governed by a set of equations set up to cause the inverter to emulate a synchronous machine, but still with current limits.

Similarly, the parameters of the 0.48:46 kV, Generator step-up transformer (GSU) transformer are shown in the figure below:

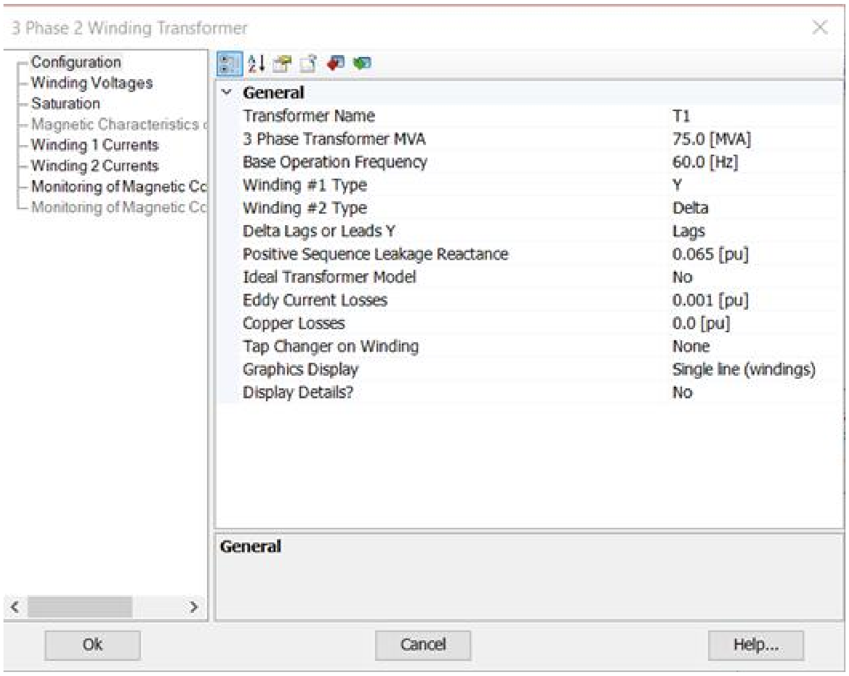

General

Transformer Name	T1
3 Phase Transformer MVA	75.0 [MVA]
Base Operation Frequency	60.0 [Hz]
Winding #1 Type	Y
Winding #2 Type	Delta
Delta Lags or Leads Y	Lags
Positive Sequence Leakage Reactance	0.065 [pu]
Ideal Transformer Model	No
Eddy Current Losses	0.001 [pu]
Copper Losses	0.0 [pu]
Tap Changer on Winding	None
Graphics Display	Single line (windings)
Display Details?	No

Figure 12. GSU transformer parameters

The GSU transformer was modeled without any saturation enabled in the PSCAD model. According to the manufacturer, the inverters for use in this BESS have an enhanced fault current capability and are able to produce up to 1.5 p.u. fault current on the inverter's rated current basis. This additional fault current capability is higher than most PV inverters and offers additional output that is useful to provide black start inrush capacity of the BESS as well as sufficient fault current for certain overcurrent protection requirements needed on the 46 kV system in microgrid mode.

3.4. Grounding Study

The grounding of power systems is important for maintenance of proper voltages. For example, ground fault overvoltage (GFOV) can occur when a single phase to ground fault occurs on an ungrounded power system, and can cause the line-ground voltage on the unfaulted phases to rise to as high as 173% of the rated value. Grounding of the system can prevent GFOV. Grounding is also important for maintenance of proper voltages when the loads are unbalanced phase-to-phase, which is typical in distribution.

On the Old Forge 46 kV circuit, the 115:46 kV transformer at Boonville is configured to provide grounding to the 46 kV circuit. However, when this circuit goes into off-grid mode, that 115:46 kV transformer is outside of the boundary of the intentional island system. Thus, another means of grounding the 46 kV circuit must be provided. This will be done by including a grounding transformer on the 46 kV bus of the BESS plant, which will be switched out when the microgrid is grid-connected so as to avoid impacts on the on-grid protection coordination. There are two options for doing this:

1. A separate grounding transformer can be provided. This grounding transformer could be a YG:d, with the YG on the 46 kV side, or a zigzag. This grounding transformer would be switched out of the circuit when the Old Forge system is on-grid.
2. The BESS step-up transformer could be configured as a three-winding transformer with a buried delta tertiary winding. This buried delta along with a YG connection on the 46 kV side would provide the needed grounding to the 46 kV circuit. A switch would be included on the grounding lead of the 46 kV YG winding so that, when in on-grid mode, the ground connection could be open-circuited.

The impedances of the grounding transformer and the transformer's grounding impedance (the impedance between the transformer and "remote earth" or "true ground") impact the ability of the grounding transformer to help maintain proper voltages. If these impedances are too high, overvoltages will not be prevented. Reducing this impedance requires increasing the apparent power (MVA) rating of the grounding transformer, which increases costs. Thus, it is desirable to determine the minimum size of grounding transformer that maintains overvoltages below some selected level while providing sufficient asymmetrical fault current to make relaying possible.

When the power source for an intentional island system is a synchronous generator, there is a relatively straightforward procedure for determining the needed grounding transformer impedance. However, for inverter-based sources, this procedure does not work, and EMT simulation is used to identify the appropriate grounding transformer impedance and size.

To that end, the PSCAD model was used to provide insights into the sizing of a grounding transformer that would cause the Old Forge system to remain effectively grounded while operating in the off-grid (microgrid) mode. The grounding transformer was assumed to be a YG:d three-phase transformer as shown in Figure 13. The grounding transformer is connected to the 46 kV bus next to the BESS plant's 46 kV step-up transformer, as shown in the figure. A small load of 10 kW (<<

1% of the BESS nameplate rating) was connected to the grounding transformer secondary side to maintain numerical stability. The impedance to remote earth as seen from the grounding lead of the transformer is represented by the 1 ohm resistor shown. The parameters used in the grounding transformer model are shown in Figure 14. The grounding transformer secondary (delta) winding voltage was selected to be 13.8 kV. The transformer model is linear; saturation is not modeled. In these grounding transformer sizing simulations, the 3 MVAR capacitor at Alder Creek is offline.

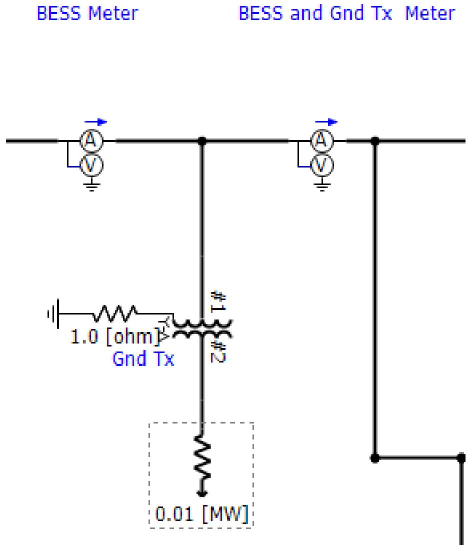

Figure 13. Grounding transformer model.

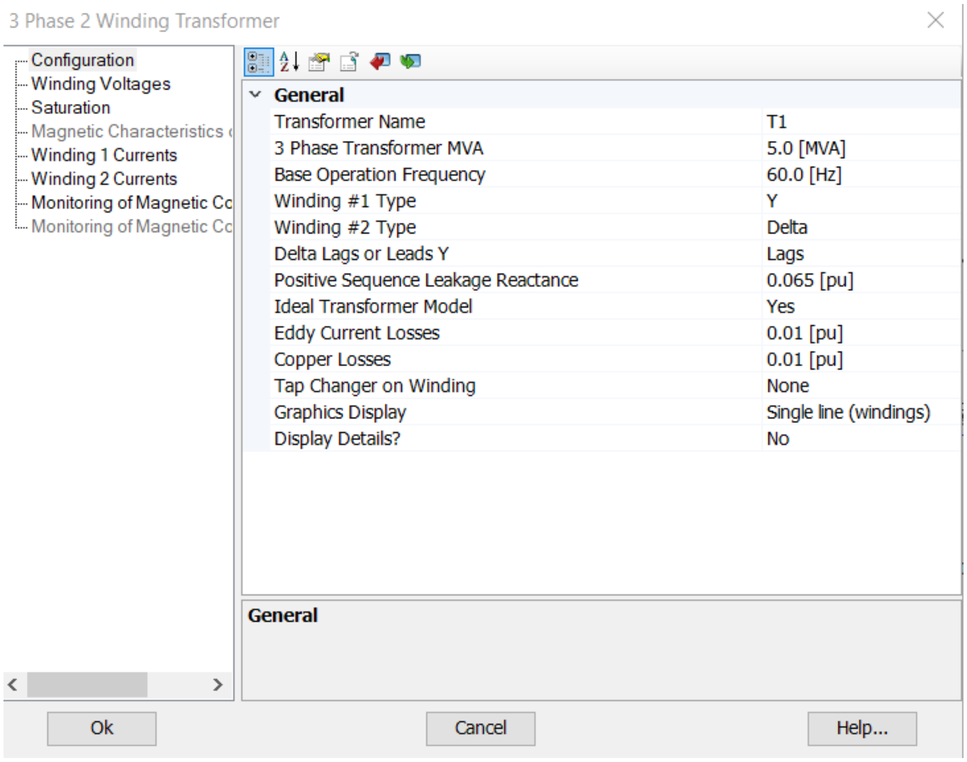

General

Transformer Name	T1
3 Phase Transformer MVA	5.0 [MVA]
Base Operation Frequency	60.0 [Hz]
Winding #1 Type	Y
Winding #2 Type	Delta
Delta Lags or Leads Y	Lags
Positive Sequence Leakage Reactance	0.065 [pu]
Ideal Transformer Model	Yes
Eddy Current Losses	0.01 [pu]
Copper Losses	0.01 [pu]
Tap Changer on Winding	None
Graphics Display	Single line (windings)
Display Details?	No

Figure 14. Parameters used in the grounding transformer model.

In this portion of the report, reference will be made to a number of meters and other locations on the 46 kV system. Figure 15 shows the locations of these numbered meters (the red circled numbers in the figure), as well as the BESS point of interconnection (POI) (shown in green text toward the right end of the figure) and the three line regulators (noted via purple text).

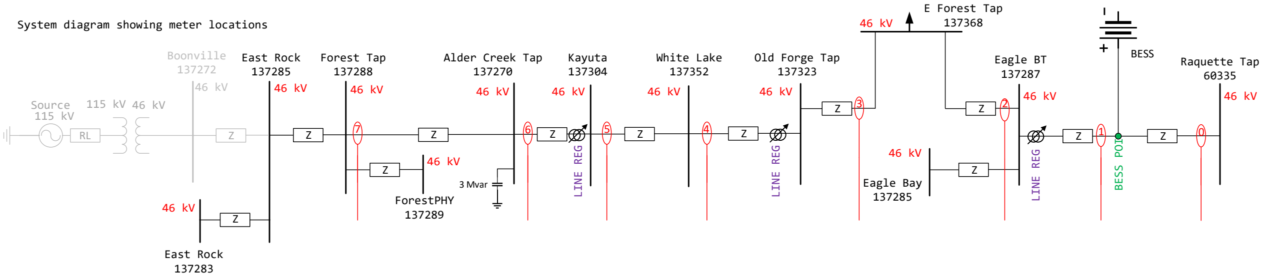

Figure 15. One-line diagram of the Old Forge 46 kV system, showing the locations of numbered meters, line regulators, and the BESS POI.

The GFOV occurs for a fault at the BESS POI, and the largest GFOV occurs at that same point, the BESS POI. Thus, results are reported here for this worst-case condition. Figure 16 shows the peak ungrounded phase voltage at Meter 1 (shown in Figure 15) as a function of grounding transformer apparent power (MVA) rating, with all other transformer parameters remaining as shown in Figure 14. In particular, the transformer per-unit impedance was held to 6.5% with an X/R of 10. The absolute impedance then varies according to the transformer MVA rating. These results indicate that a grounding transformer of 5 MVA rating is the smallest grounding transformer for which the unfaulted phase voltage remains below 1.39 p.u.[1, 2] for all 1LG faults on the system. Figure 17 shows the phase-ground voltage waveforms during a 1LG fault starting at t = 12 s with a 5 MVA grounding transformer. The waveforms remain sinusoidal, and the peak magnitude is limited to 1.37 p.u. of the nominal peak value. For comparison, Figure 18 shows the same voltages for the same 1LG fault, but with a 3 MVA grounding transformer. The waveforms are still sinusoidal but the peak voltages on the unfaulted phases reach 1.46 p.u.

---

[1] The 1.39 pu value comes from IEEE Std C62.92.1-2016, clause 7.1. However, *if* the Old Forge 46 kV system has no phase-ground load connected to it and its arresters have a sufficiently high MCOV, then it might be permissible for the unfaulted-phase voltages to exceed the 1.39 pu value, allowing the use of a smaller grounding transformer.

[2] The 1.39 pu value given in IEEE C62.92.1 refers to an RMS value. The values given in Figure 16 are *peak* voltage values. As shown in subsequent figures, the simulations suggest that the voltage waveforms can become significantly distorted during a 1LG fault on this system, so the 1.39 pu value might not apply to the *peak* in this case. It would be best to allow some margin in this case.

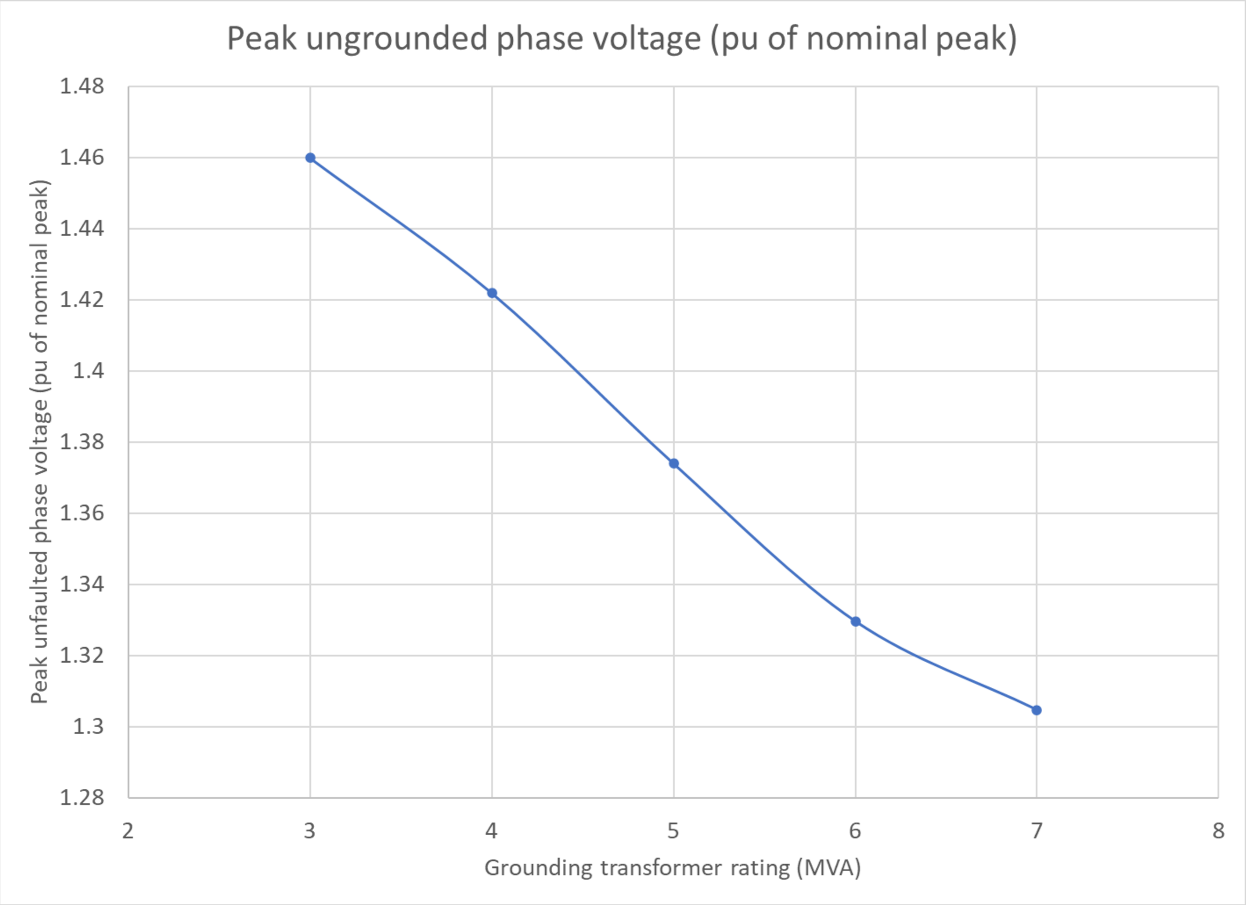

Figure 16. Peak unfaulted phase voltage at the POI versus grounding transformer size (MVA) for a 1LG fault at the POI, assuming the impedance parameters in Figure 14.

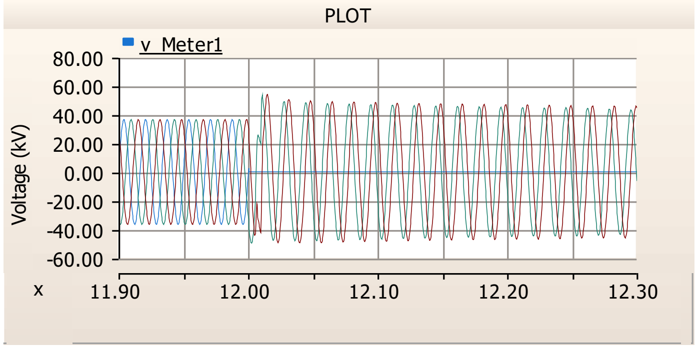

Figure 17. Line-ground voltage waveforms at Meter 1 during a 1LG fault at the BESS POI, with a 5 MVA 6.5% Z grounding transformer. The fault occurs at t = 12 s.

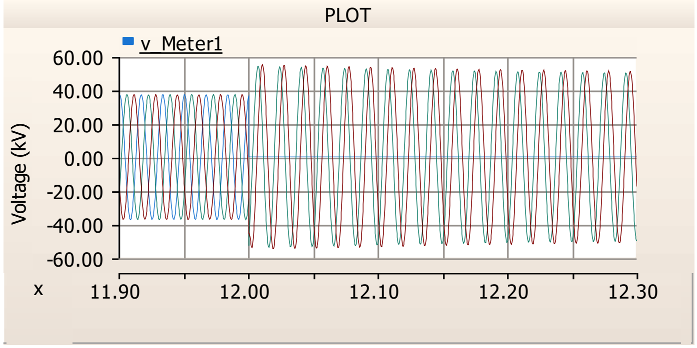

Figure 18. Line-ground voltage waveforms at meter 1 during a 1LG fault at the BESS POI, with a 3 MVA 6.5% Z grounding transformer. The fault occurs at t = 12 s.

Note in Figure 16 that the reduction in unfaulted-phase peak voltage appears to incrementally decrease as the grounding transformer gets larger. This occurs because once the grounding transformer exceeds 7 MVA, an oscillation begins to appear in the inverter output resulting in a distorted waveform, and the unfaulted-phase voltage peaks are set by the peaks of those harmonic voltages. For example, Figure 19 shows the phase-ground voltage waveforms at meter 1 for a 1LG fault on the BESS POI with an 8 MVA grounding transformer. A sizeable harmonic content begins to appear in the unfaulted phase voltages, and the peaks of those harmonics dominate the overall peak voltage, masking any benefit from further increasing the grounding transformer size. This oscillation may be due to a mismatch between the negative-sequence current demand of the circuit and the inverters' negative-sequence current capabilities or controls.

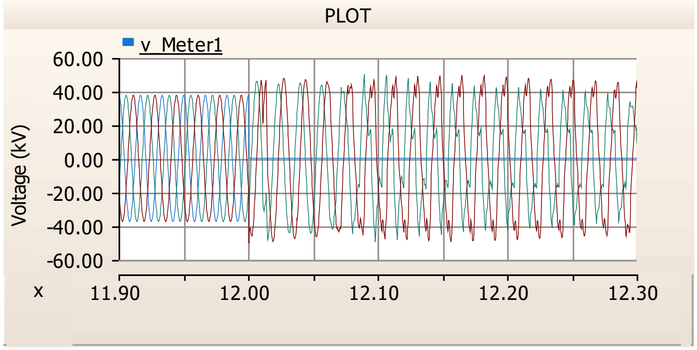

Figure 19. Line-ground voltage waveforms at Meter 1 during a 1LG fault at the BESS POI, with an 8 MVA grounding transformer. The fault occurs at t = 12 s.

Simulations were also run to test the impact of the grounding resistance (impedance to remote earth) and suggest what range is acceptable for this parameter. The simulation results suggest that the grounding transformer impedance to remote earth must be 1 + j0 Ω or less. If the impedance to remote earth is higher than this, during the post-fault recovery after a 1LG fault applies and is cleared the simulations suggest that the inverter can in some cases enter an unstable state in which its output is highly distorted. An example is shown in Figure 20 through Figure 26. These figures show phase-ground voltages at Meter 1 (see Figure 15 for the location of Meter 1) and BESS 480-V output currents before, during and after a 1LG fault at the BESS POI. Figure 20 shows a broader view of the Meter 1 phase-ground voltages during the whole event. The ground fault overvoltages at the beginning of the fault event (t = 12 s) are evident, but the peak voltages quickly fall to an acceptable level. The fault clears at t = 13 s, and the voltage appears to recover. Figure 21 shows a zoomed-in view of the Meter 1 line-ground voltages centered around the moment the fault strikes (t = 12 s), and Figure 22 shows the BESS phase currents on the 480 V bus during the same time period. At this zoom level, the distortion in the voltage and current waveforms is apparent.

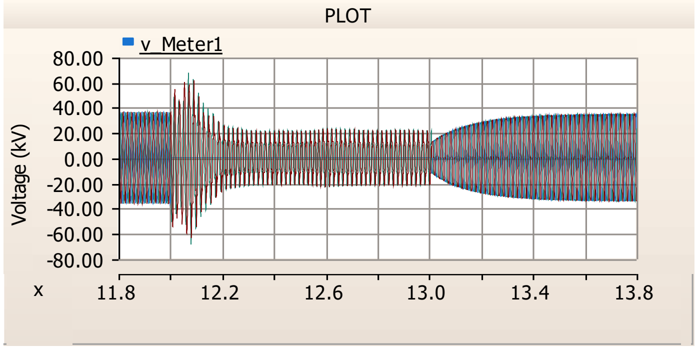

Figure 20. Line-ground voltage waveforms at Meter 1 during a 1LG fault at the BESS POI, with a 5 MVA grounding transformer and a 5 + j0 Ω impedance to remote earth. The fault occurs at t = 12 s and clears at t = 13 s, so this view shows pre- and post-fault data.

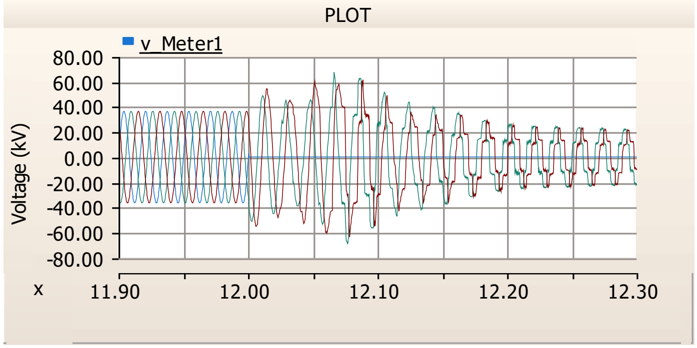

Figure 21. Line-ground voltage waveforms at Meter 1 during a 1LG fault at the BESS POI, with a 5 MVA grounding transformer and a 5 + j0 Ω impedance to remote earth, showing the period right before and after the fault occurs at t = 12 s.

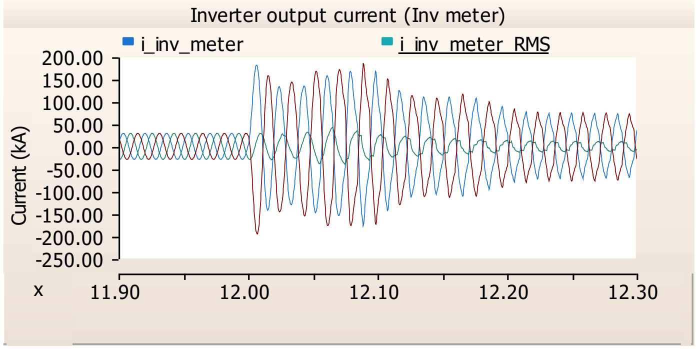

Figure 22. BESS output phase currents at the 480 V BESS meter corresponding to the voltages shown in Figure 21.

Figure 23 and Figure 24 show the Meter 1 voltages and BESS phase currents respectively centered on the moment when the 1LG fault clears, at t = 13 s. Prior to the fault clearing, the output current is nearly triangular, possibly indicating controller saturation, and the voltage shows a high level of harmonic distortion.

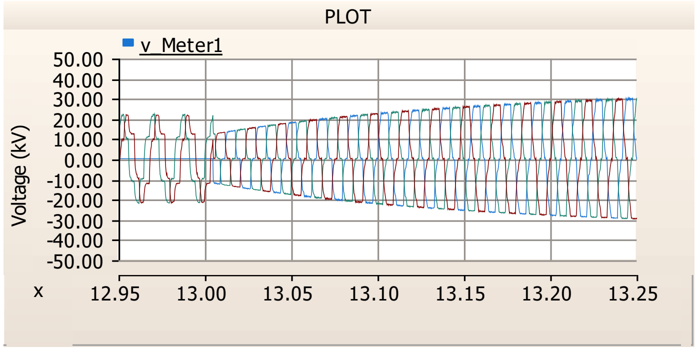

Figure 23. Line-ground voltage waveforms at Meter 1 during a 1LG fault at the BESS POI, with a 5 MVA grounding transformer and a 5 + j0 Ω impedance to remote earth. This view is zoomed in on the period right before and after the fault is cleared at t = 13 s. Note the highly distorted voltage waveforms both before and after the fault clears.

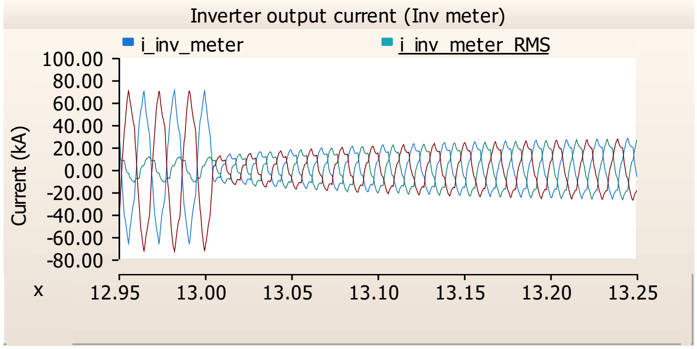

Figure 24. BESS phase currents at the 480 V BESS meter during a 1LG fault at the BESS POI, with a 5 MVA grounding transformer and a 5 + j0 Ω impedance to remote earth. This view is zoomed in on the same time period as Figure 23. Note the near-triangular inverter current prior to the fault clearing at t = 13 s, and the residual distortion after the fault clears.

Finally, Figure 25 and Figure 26 show the Meter 1 phase voltages and BESS 480-V output phase currents respectively several seconds after the fault clears, again for a 5 MVA grounding transformer with a 5 + j0 Ω grounding impedance. The inverter current remains highly distorted, and the voltage waveforms are nearly square. The square voltage waveform causes the RMS measurements in the simulation to be inaccurate, and as a result all of the transformer tap changers start trying to correct for the nonsinusoidal voltage (Figure 27). In most of these cases, the inverter eventually trips either on overvoltage or underfrequency. The take-away point here is that the simulations suggest that the grounding impedance must be kept low.

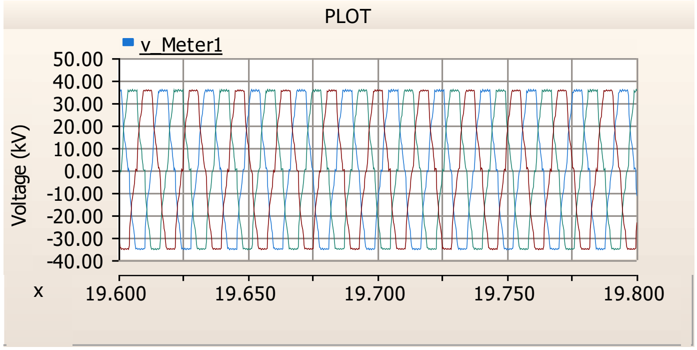

Figure 25. Line-ground voltage waveforms at meter 1 well into the post-fault period (the fault cleared at t = 13 s), with the 5 MVA grounding transformer and 5 + j0 Ω impedance to remote earth.

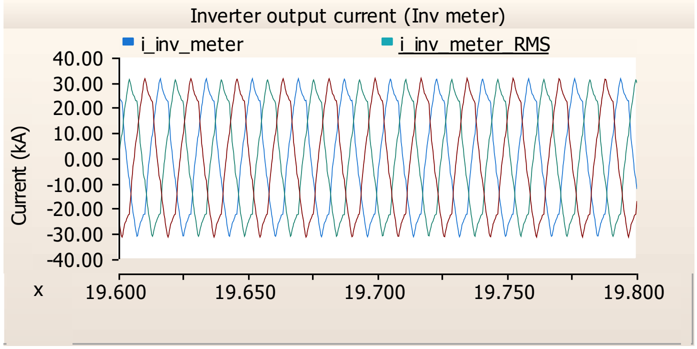

Figure 26. BESS output phase currents at the 480 V BESS meter corresponding to the voltages shown in Figure 25.

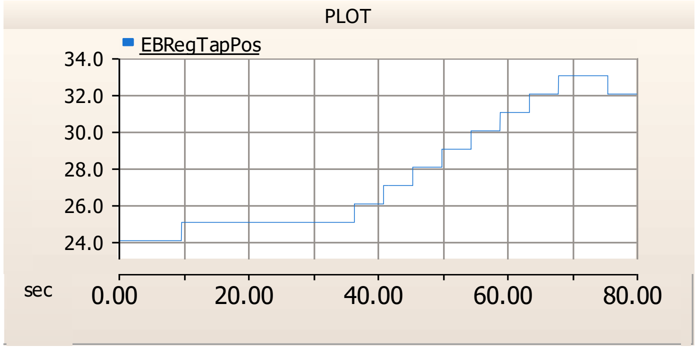

Figure 27. Eagle Bay regulator tap position during a 1LG fault event at the BESS POI. The fault in this case occurs at t = 20 s. The grounding transformer size is 5 MVA and the grounding impedance is 5 + j0 Ω.

3.5. Black-Start Study

Simulations were run to test the ability of the 76.3 MVA BESS to perform a cold-load start of the microgrid in the off-grid mode. It is always important to conduct a black-start test of any islanded power system, but in this case it is especially important because it is expected that the transition from on-grid to off-grid operation will be an "open transition" in which the microgrid is de-energized during the transmission, then restarted.

For these simulations, saturation was turned "on" in the transformer models so that they would draw inrush current. The magnetizing current was set to 0.01 pu, and the air-core inductance to 0.2 pu. The remanent flux in all legs of all transformers was set to zero. The secondary side breaker of each distribution transformer is initially open, so that the transformer inrush current is isolated from the load inrush current. The secondary-side breakers close at t = 10 s, so in this case there is no segmentation or "staggering" of the secondary breakers on the distribution transformers; they are all closed at the same time.

In addition, for the black-start simulations, two induction machines were modeled at Old Forge, to represent the Old Forge ski area load. These are squirrel-cage motors sized at 230 kVA (308 hp) each. The purpose of including these motors is to subject the BESS inverters to the challenge of a large-motor start while simultaneously executing a cold-load pickup. The mechanical torque on the machine is modeled as being 0.95 times the square of the motor per-unit speed, as shown in Figure 28. One motor is connected to each of the two Old Forge 4.8 kV buses, as shown in Figure 29. The parameter values used in the motor models are shown in Table 7. Both motors are started simultaneously at t = 20 s (10 s after the rest of the load is picked up by closing the distribution transformer secondary breakers). The motors are started directly across the line; no soft-starting means is employed. This is done to make the motor-start test as stringent a test as possible for the BESS inverters.

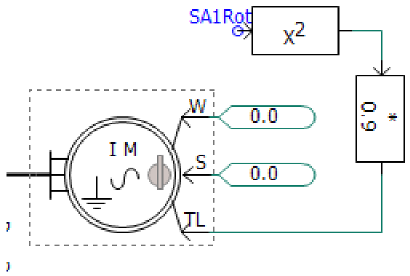

Figure 28. Schematic of motor model for Ski Area Motor #1.

Table 7. Motor model parameter values

Parameter	Value
Rated MVA	0.23 MVA (308 hp)
Rated voltage	4.8 kV_{LL}
Stator/Rotor turns ratio	2.637687
Inertial time constant (J)	0.7267 s
Mechanical damping	0.01 pu
Motor type	Squirrel-cage
Stator resistance	0.0054 pu
Wound rotor resistance	0.00607 pu
First squirrel-cage resistance	0.298 pu
Magnetizing inductance	4.362 pu
Stator leakage inductance	0.102 pu
Wound rotor leakage inductance	0.11 pu
First cage leakage inductance	0.05 pu
Mutual inductance—wound rotor—1st cage	0.02 pu

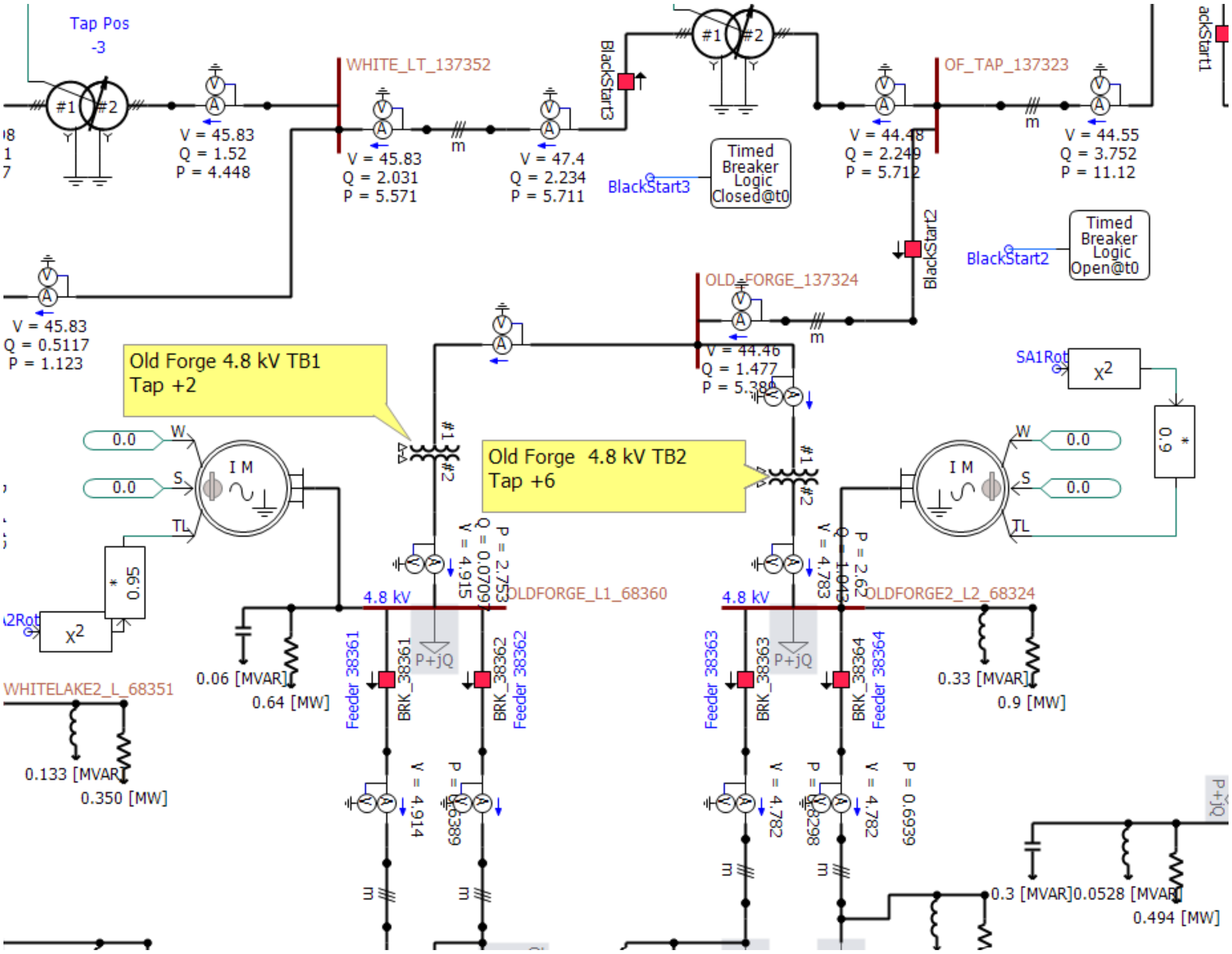

Figure 29. Screen shot of the PSCAD model centered on the Old Forge bus, showing the connection locations of the two induction machines.

Figure 30 shows the active and reactive power output from the BESS (measured on the 46 kV bus of the BESS plant 480 V:46 kV step-up transformer) as a function of time during the black-start sequence. The constant-impedance load is picked up at t = 10 s by simultaneously closing all of the distribution transformer secondary breakers, and the motor load starts at t = 20 s. Figure 31 shows the RMS voltage on the 46 kV bus on the controlled side (the side *away* from the BESS) during the black start sequence. It is important to note that the BESS ramps the voltage when it first starts, reaching rated voltage after about 4 s, effectively implementing a soft-start of the islanded system. Because the distribution transformers' primary sides are all connected to the 46 kV bus during the initial voltage ramp, this ramp-up of the voltage upon black start virtually eliminates the transformer inrush. The voltage dips at 10 and 20 s as expected because of the starting of the constant-Z and motor loads respectively, reaching a minimum of 0.96 pu after the motors start. At that point the regulators begin adjusting their tap settings to bring the voltage closer to nominal—for example, see Figure 32 which shows the tap position of the Eagle Bay regulator during the black start event. (In this case, because the regulator's tap changer is on the side facing the BESS but the controlled side is the other side of the regulator, *lowering* the tap position *raises* the voltage on the controlled side of the regulator.) Figure 33 shows the mechanical rotational speeds of the two induction machines on the Old Forge, and indicates that both come up to speed without difficulty (albeit somewhat slowly; note that it takes 7 s for the motors to reach their final steady-state speed). The ultimate result is that the BESS black-starts the entire microgrid without difficulty, which is not surprising given that the BESS' apparent power rating is just over three times the peak load in the microgrid.

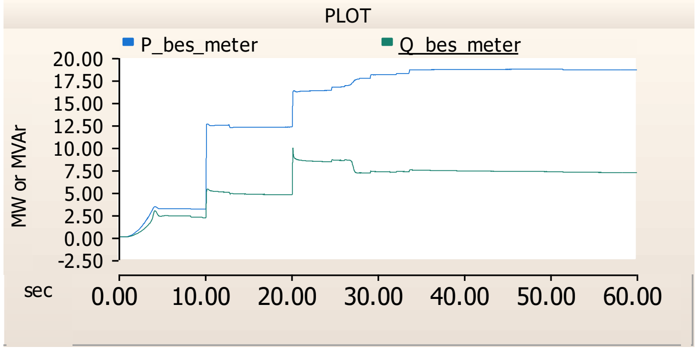

Figure 30. Active and reactive power output from the BESS during the black-start sequence with constant-impedance loads starting at t = 10 s and motor load at t = 20 s (off-grid mode).

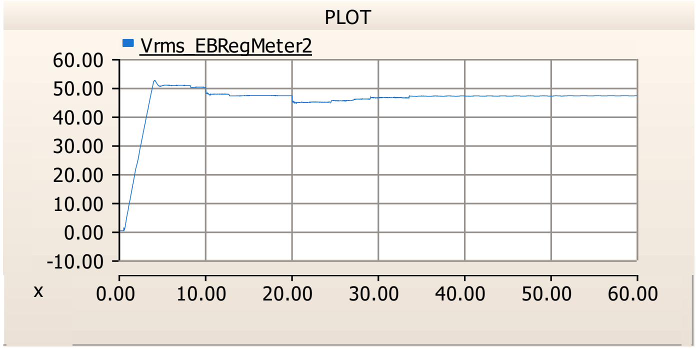

Figure 31. RMS voltage measured at the controlled side of the Eagle Bay voltage regulator during the black-start sequence with constant-impedance loads starting at t = 10 s and motor load at t = 20 s (off-grid mode).

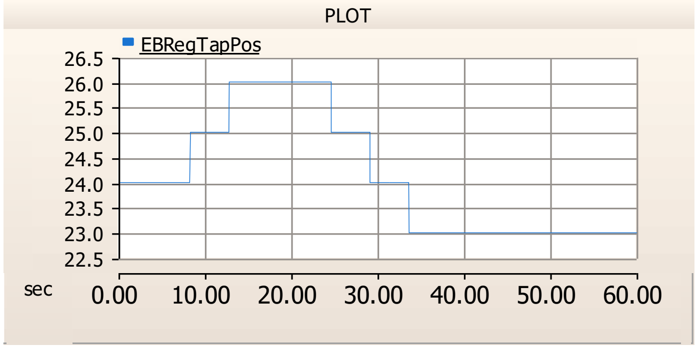

Figure 32. Tap position of the Eagle Bay voltage regulator during the black-start sequence with constant-impedance loads starting at t = 10 s and motor load at t = 20 s (off-grid mode). (Recall that *lowering* the tap position *raises* the voltage in this case.)

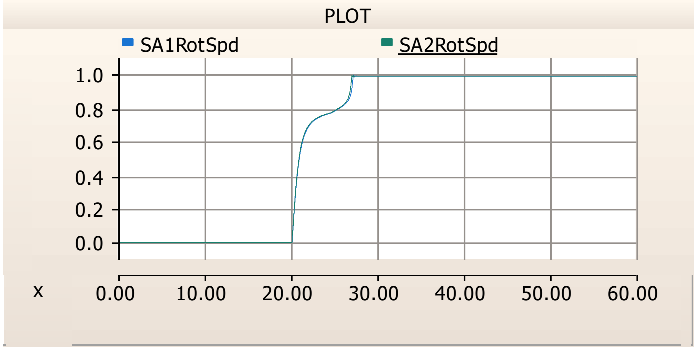

Figure 33. Mechanical (rotational) speed of the two Old Forge induction motors during the black-start sequence with constant-impedance loads starting at t = 10 s and motor load at t = 20 s (off-grid mode).

A simulation was also run in which the entire load (constant-Z load plus the motor load) was all picked up at t = 10 s. Figure 34 shows the active and reactive power output from the BESS, Figure 35 shows the RMS voltage on the controlled side of the Eagle Bay regulator, and Figure 36 shows the rotational speed of the induction machines, during this black-start event with all of the load started simultaneously at t = 10 s. As before, the BESS applies a voltage ramp to the islanded system and reaches rated voltage in 4 s. In this case also, the BESS is able to black-start the load without a trip or unacceptable voltage excursion.

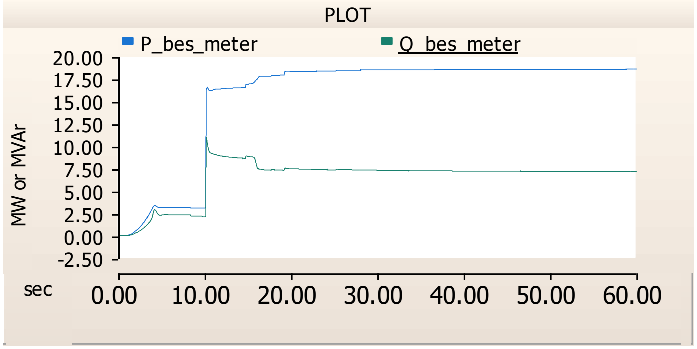

Figure 34. Active and reactive power output from the BESS during the black-start sequence with all loads starting at t = 10 s (off-grid mode).

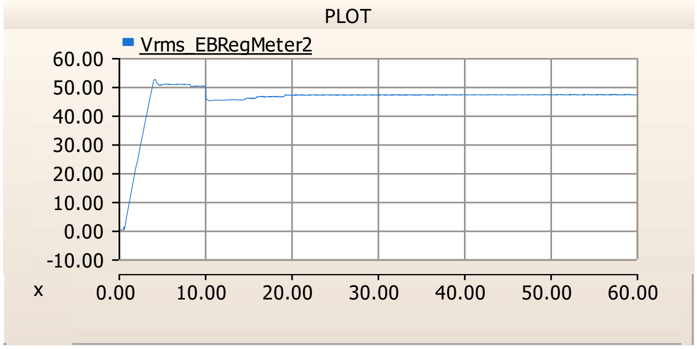

Figure 35. RMS voltage measured at the controlled side of the Eagle Bay voltage regulator during the black-start sequence with all loads starting at t = 10 s (off-grid mode).

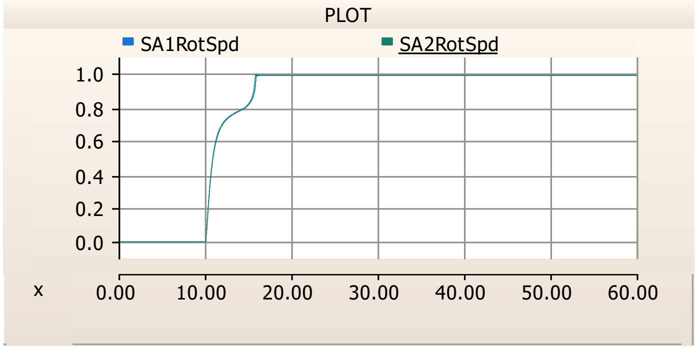

Figure 36. Mechanical (rotational) speed of the two Old Forge induction motors during the black-start sequence with all loads starting at t = 10 s (off-grid mode).

Finally, a simulation was run in which all of the distribution secondary breakers and the motor breakers were closed throughout the simulation, so the loads are connected to the BESS during the BESS' initial 4-second ramp-up of the islanded system voltage. The results of these simulations are shown in Figure 37 through Figure 39, and indicate that in this case as well the BESS is able to black-start the entire load. In fact, the voltage deviation is smaller in this case than it is in the cases in which the load is energized later, so in a sense the system's performance is better in this case. However, in a sense this case is not practical because it is expected that the secondary-side breakers of each of the distribution transformers will be open when the microgrid is de-energized during the transition from on-grid to off-grid operation. Thus, it is not expected that there ever would be a case in which all of the loads are online during the 4-s initial ramp.

From these simulations we conclude that the BESS should be able to black-start the microgrid load without any regulation problems, and that it is not necessary to bring the microgrid load online in "blocks" during black start. This is likely because of the fact that the BESS is so large relative to the peak load.

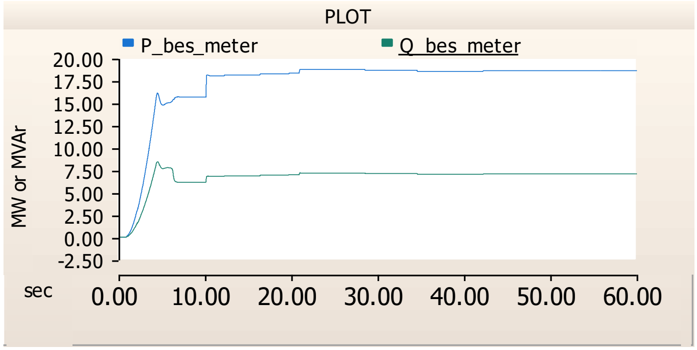

Figure 37. Active and reactive power output from the BESS during the black-start sequence with all loads starting at t = 0 s (off-grid mode).

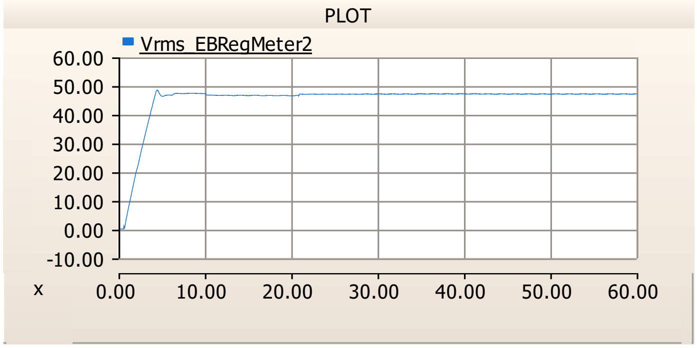

Figure 38. RMS voltage measured at the controlled side of the Eagle Bay voltage regulator during the black-start sequence with all loads starting at t = 0 s (off-grid mode).

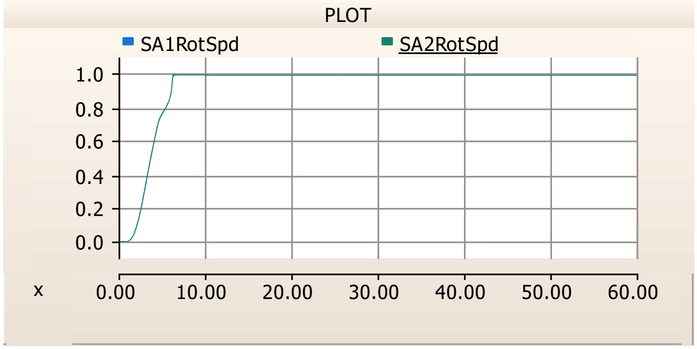

Figure 39. Mechanical (rotational) speed of the two Old Forge induction motors during the black-start sequence with all loads starting at t = 0 s (off-grid mode).

In all of these black-start simulations, the BESS ramped the voltage when first starting, reaching rated voltage in 4 s. It would be prudent to consider whether that 4-s ramp is optimal. This ramp rate effectively eliminates transformer inrush and soft-starts motor loads, but some loads, especially single-phase induction machine loads like those found on refrigerators and air conditioners, might fail to start properly if the ramp rate is too slow. A 4-s ramp is common with soft-starters on larger motors, but it would be a good idea to verify that single-phase motors, especially capacictor-start motors like those in the applications mentioned above, start and run correctly with this ramped voltage.

3.6. Inverter Sizing Study

One of the tasks originally intended as part of this study was a set of simulations in which the minimum inverter size that still produces sufficient fault current for protection operation would be determined by sweeping the BESS apparent power (MVA) rating in simulation. Unfortunately, this is not possible at this time because the supplied PSCAD black-box inverter model appears to be internally tuned for the 75 MVA BESS size and would not simulate properly if that size was reduced by more than a few percent.

3.7. Fault Simulations

3.7.1. System behavior during momentary 46 kV bus faults: OFF-GRID MODE

Dozens of fault scenarios were run using the PSCAD model, and during these simulations it was noticed that the output current of the BESS inverters can become highly distorted both during a fault and after self-clearing of a momentary fault. This is important because the impact of such distorted currents on the ability of protective relays to accurately measure voltages and currents must be carefully evaluated. This section provides some examples to illustrate this behavior.

3.7.1.1. Momentary (self-clearing) 3LG fault on the Old Forge 46 kV bus: OFF-GRID MODE

This section presents results measured during a momentary or self-clearing bolted 3LG fault on the Old Forge 46 kV bus. The fault strikes at t = 25 s and self-clears at t = 25.5 s. If distance relaying were used at Meter 1, then this fault location would *not* be within Zone 1 of the distance relay at Meter 1; this fault should be picked up by a distance relay at Meter 3.

Figure 40 shows the pre-fault phase currents. These waveforms are highly sinusoidal, as expected. Figure 41 shows the phase current waveforms at the same location during the fault. The current waveforms are now significantly distorted and appear almost triangular. This distorted current results in distorted phase-ground voltage waveforms, as shown in Figure 42. After the fault self-clears, the phase current amplitudes return to roughly their pre-fault levels, but the waveforms remain significantly distorted as shown in Figure 43. This distortion persists for long periods of time (at least tens of seconds) after the momentary fault self-clears. The voltage waveforms corresponding to these post-fault distorted currents are shown in Figure 44.

To help in understanding how distance relaying might be impacted by this waveform distortion, Figure 45 through Figure 48 show two sets of impedances vs time calculated by a PSCAD distance relay at two locations: Meter 1, and Meter 3 (see Figure 15 for the locations of these meters). The fault is in the primary zone of Meter 3, so the desired result for this fault is that the relay associated with Meter 3 should trip and that associated with Meter 1 should not. Figure 45 shows the impedances calculated using the current and voltage measurements from Meter 1. The top plot in Figure 45 shows the real and imaginary parts of the calculated Phase A-to-B impedance, and the bottom plot shows the real and imaginary parts of the calculated Phase A-to-ground impedance. Pre-fault, the impedances are relatively constant, with some expected ripple appearing in the calculated values which is caused by the fact that the PSCAD distance relay block utilizes some fixed-frequency 60-Hz measurements but the actual frequency in the islanded power system at this point is 59.8 Hz (which is due to inverter frequency droop, noting that there is no tertiary controller represented in this model so the steady-state frequency is never adjusted back to 60 Hz). During the 3LG fault, the ground impedance drops dramatically, as expected. The phase-to-phase impedance also drops but becomes highly noisy, with some of the noise peaks having amplitudes comparable to the pre-fault calculated impedance.

Figure 47 shows the impedances calculated using the current and voltage measurements from Meter 3, and Figure 48 shows a view of Figure 47 zoomed in on the period of the fault. Comparing Figure 48 against Figure 46, it is clear that the impedances measured at Meter 3 are much lower than those measured at Meter 1, and thus differentiation of the zones is possible. However, due to the waveform distortion and "jitter" in the inverters' phase angle controls during the fault, the impedance measurements are extremely noisy and it is not clear how reliable zone differentiation can be in this situation. Furthermore, after the fault self-clears, all of the impedance measurements are extremely noisy and it is not clear how any of the relays will behave at this point.

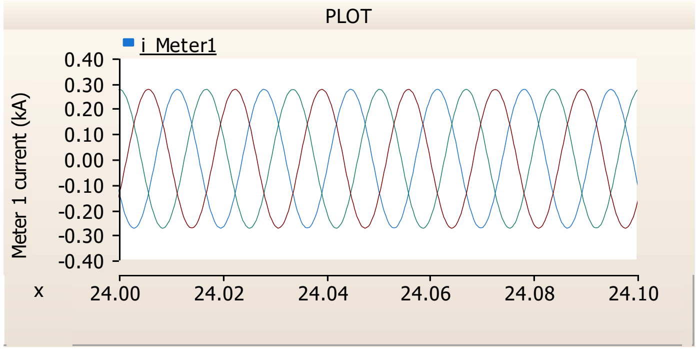

Figure 40. Pre-fault phase current waveforms measured at Meter 1 (off-grid mode).

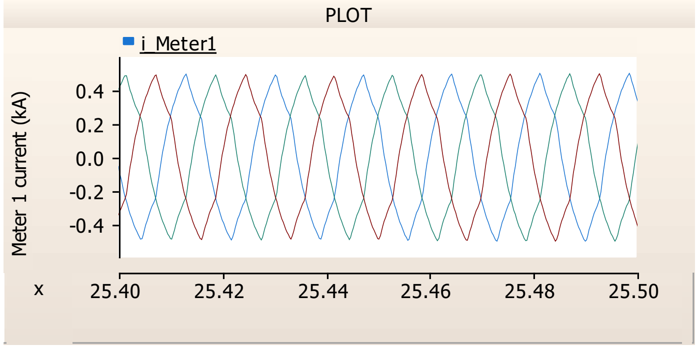

Figure 41. Phase current waveforms measured at Meter 1 during a 3LG fault on the Old Forge 46 kV bus (off-grid mode).

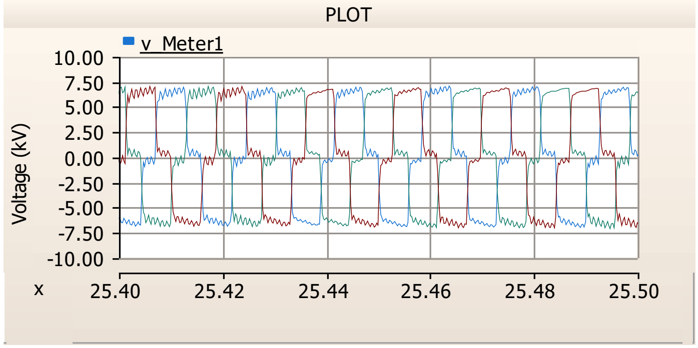

Figure 42. Phase voltages at Meter 1 corresponding to the currents shown in Figure 41 (off-grid mode).

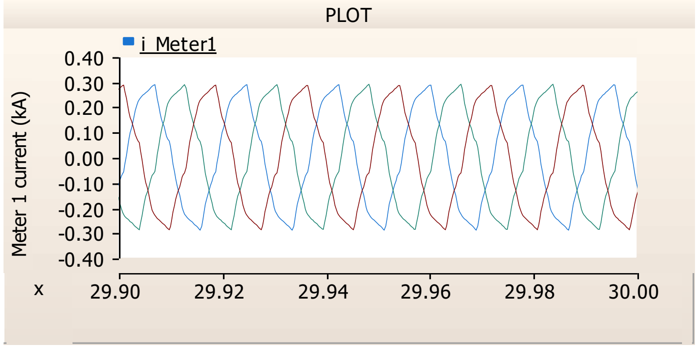

Figure 43. Post-fault (after self-clearing) phase current waveforms measured at Meter 1 (off-grid mode).

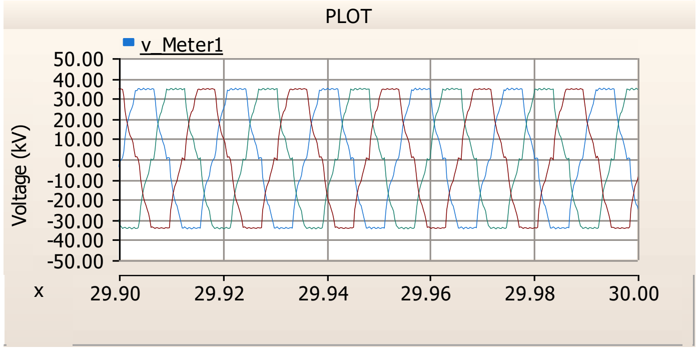

Figure 44. Phase-ground voltage waveforms at Meter 1 corresponding to the currents shown in Figure 43 (off-grid mode).

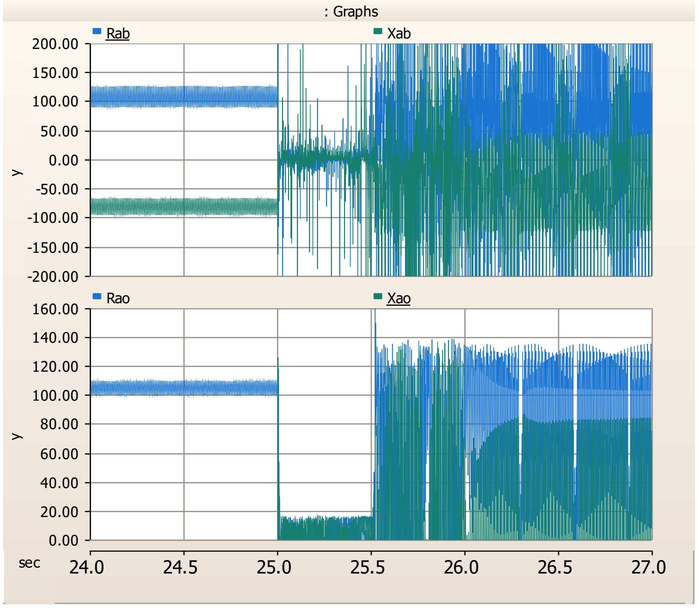

Figure 45. Phase A-to-B impedance (top) and phase A-to-ground impedance (bottom) measured at Meter 1 before, during and after a 3LG fault on the Old Forge 46 kV bus (fault starts at t = 25 s and self-clears at t = 25.5 s) (off-grid mode).

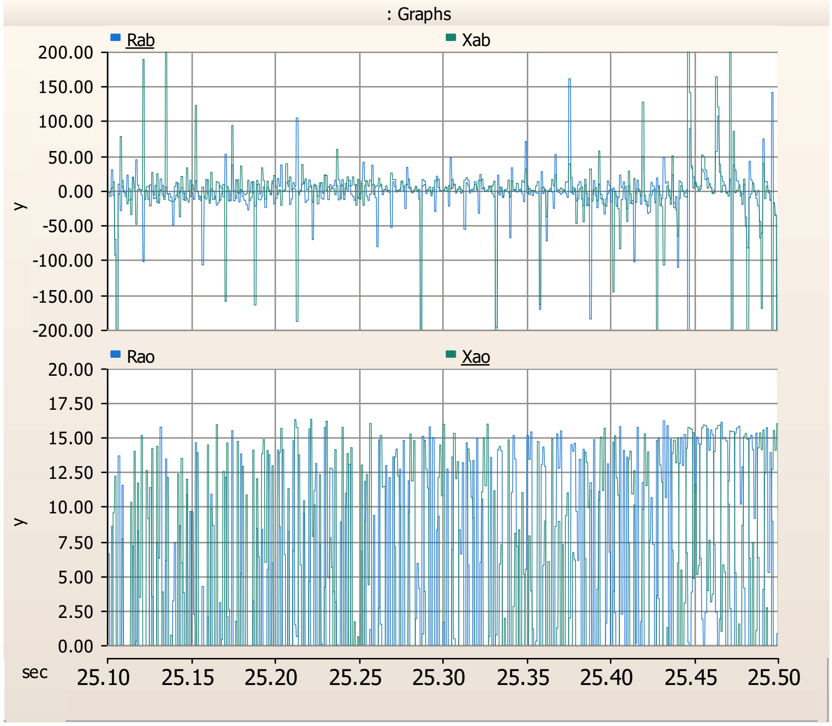

Figure 46. A zoomed-in view of Figure 45 that more clearly shows the time period of the 3LG fault (off-grid mode).

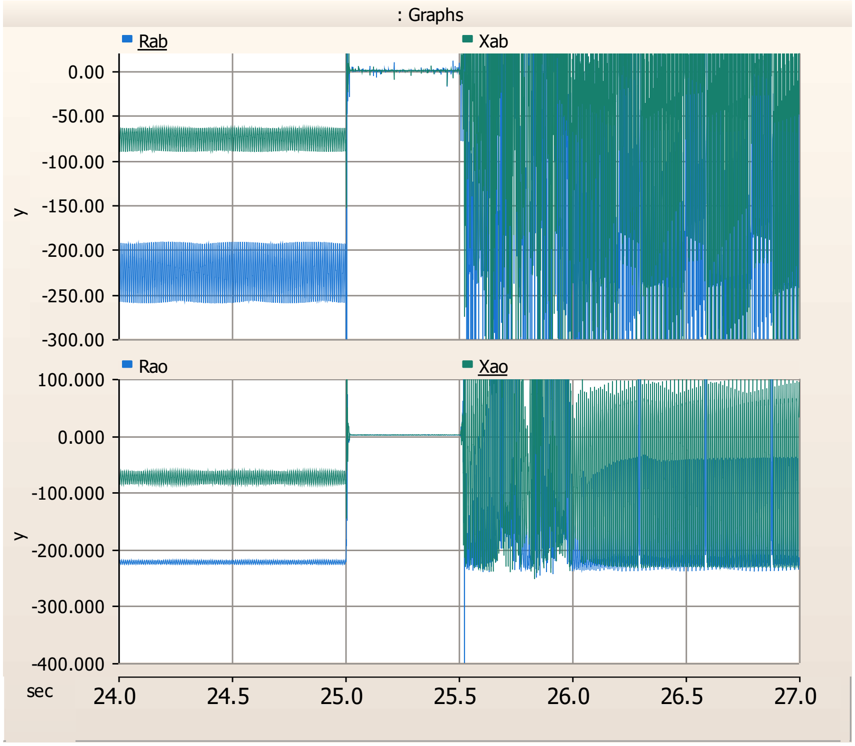

Figure 47. Phase A-to-B impedance (top) and phase A-to-ground impedance (bottom) measured at Meter 3 before, during and after a 3LG fault on the Old Forge 46 kV bus (fault starts at t = 25 s and self-clears at t = 25.5 s) (off-grid mode).

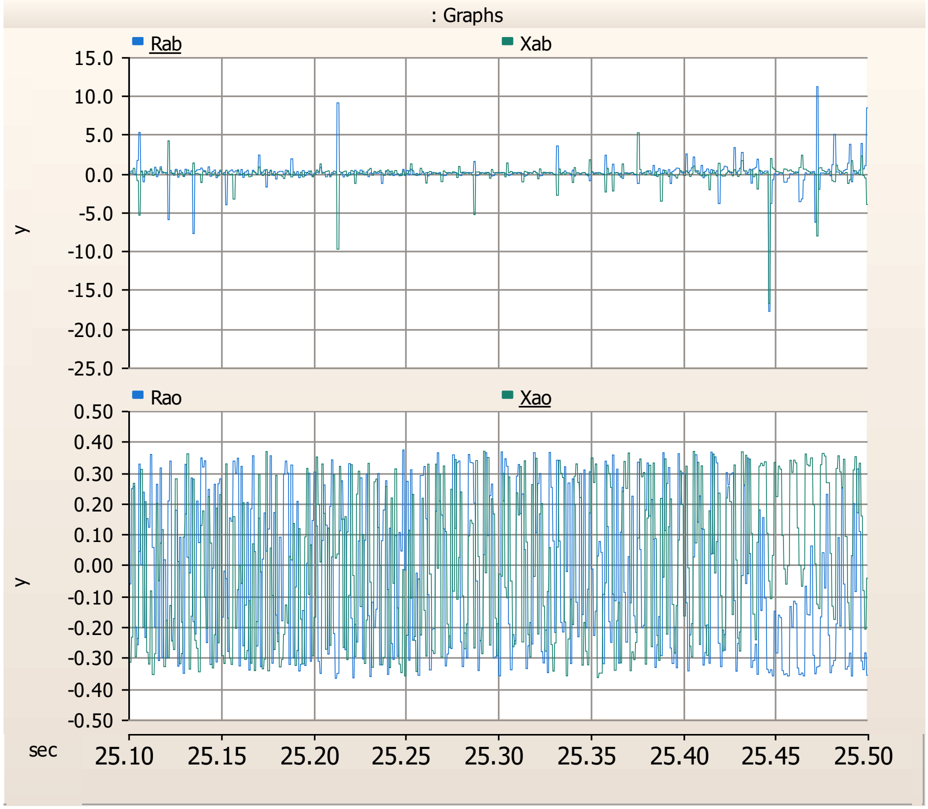

Figure 48. A zoomed-in view of Figure 47 that more clearly shows the time period of the fault (off-grid mode).

3.7.1.2. Momentary (self-clearing) 2L fault on the Old Forge 46kV bus: OFF-GRID MODE

This section presents results from simulation of a momentary or self-clearing bolted 2L fault (phase A to phase B) on the Old Forge 46 kV bus. The fault strikes at t = 25 s and self-clears at t = 25.5 s. If distance relaying were used at Meter 1, then this 2L fault would *not* be within Zone 1 of the distance relay at Meter 1; this fault should be picked up by a distance relay at Meter 3.

Figure 49 and Figure 50 show the phase current waveforms and the phase-ground voltage waveforms respectively during the 2L fault. Figure 51 and Figure 52 show the same waveforms post-fault. As was the case with the 3LG fault, the inverter output current remains distorted after the 2L fault self-clears.

Figure 53 shows impedances calculated using voltages and currents from Meter 1, and Figure 54 shows the impedances calculated using voltages and currents from Meter 3. The y-axis scaling is the same in these two figures. As was the case for the 3LG fault, during the 2L fault the impedances measured at Meter 3 are *generally* lower than those measured at Meter 1, and thus zone differentiation should be possible, but the calculated values are so noisy that it is not clear how reliable zone identification would be. The post-fault period is not shown here but it is similar to that following the 3LG fault: after the 2L fault clears all of the impedance measurements at all relays become extremely noisy, probably due to the distorted waveforms, and it is not clear how the relays will behave post-fault.

Figure 49. Phase current waveforms measured at Meter 1 during a 2L fault on the Old Forge 46 kV bus (off-grid mode).

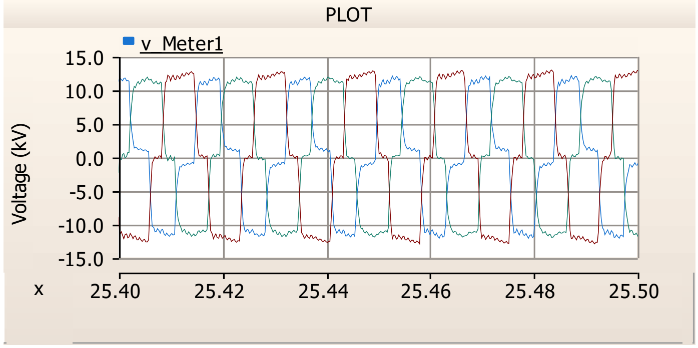

Figure 50. Phase-ground voltage waveforms measured at Meter 1 during a 2L fault on the Old Forge 46 kV bus (off-grid mode).

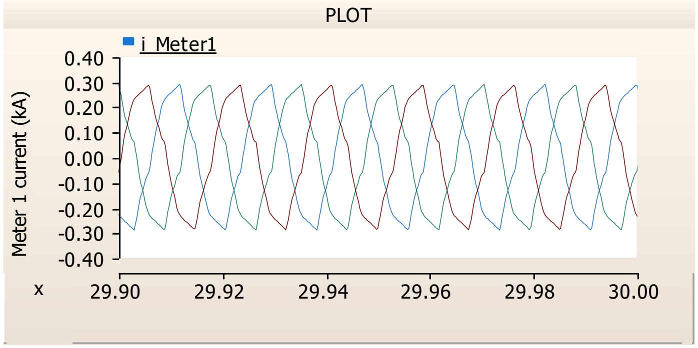

Figure 51. Post-fault current waveforms measured at Meter 1 (off-grid mode).

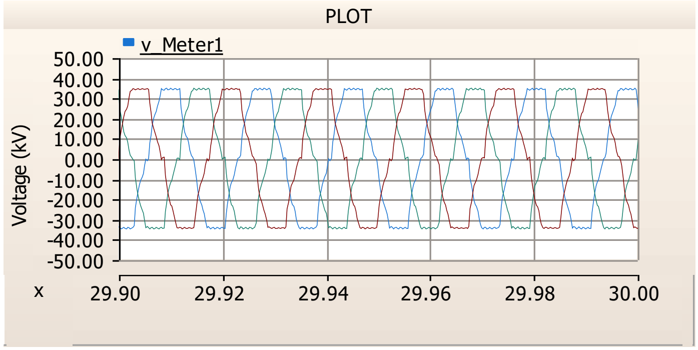

Figure 52. Post-fault voltage waveforms measured at Meter 1 (off-grid mode).

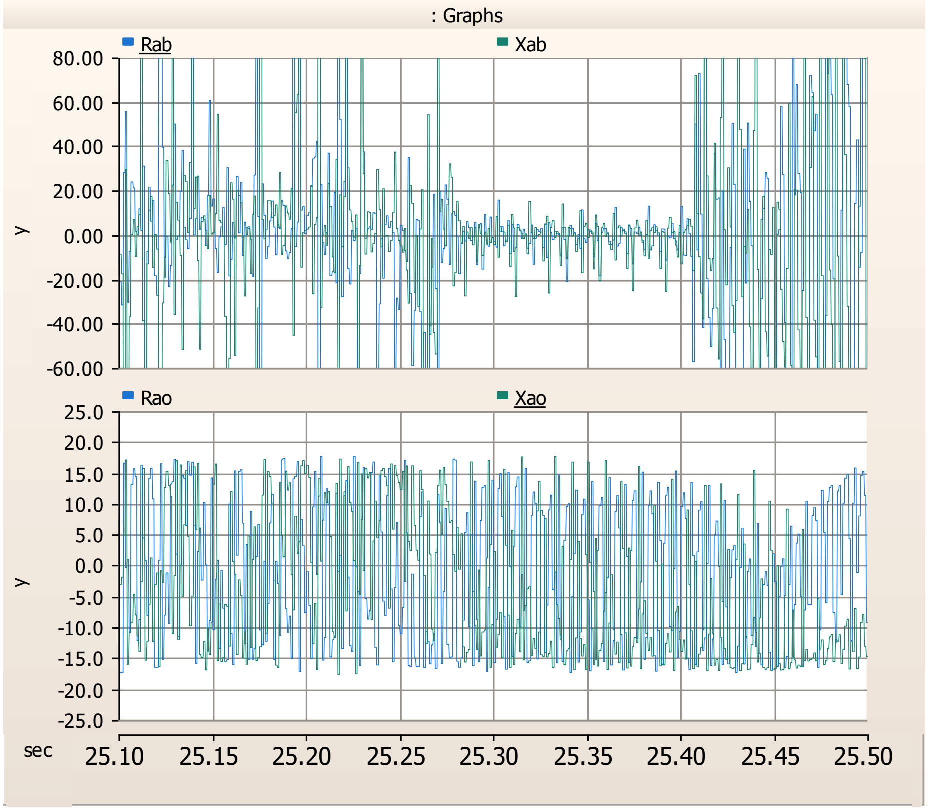

Figure 53. Impedances during the 2L fault calculated using voltages and currents from Meter 1 (off-grid mode).

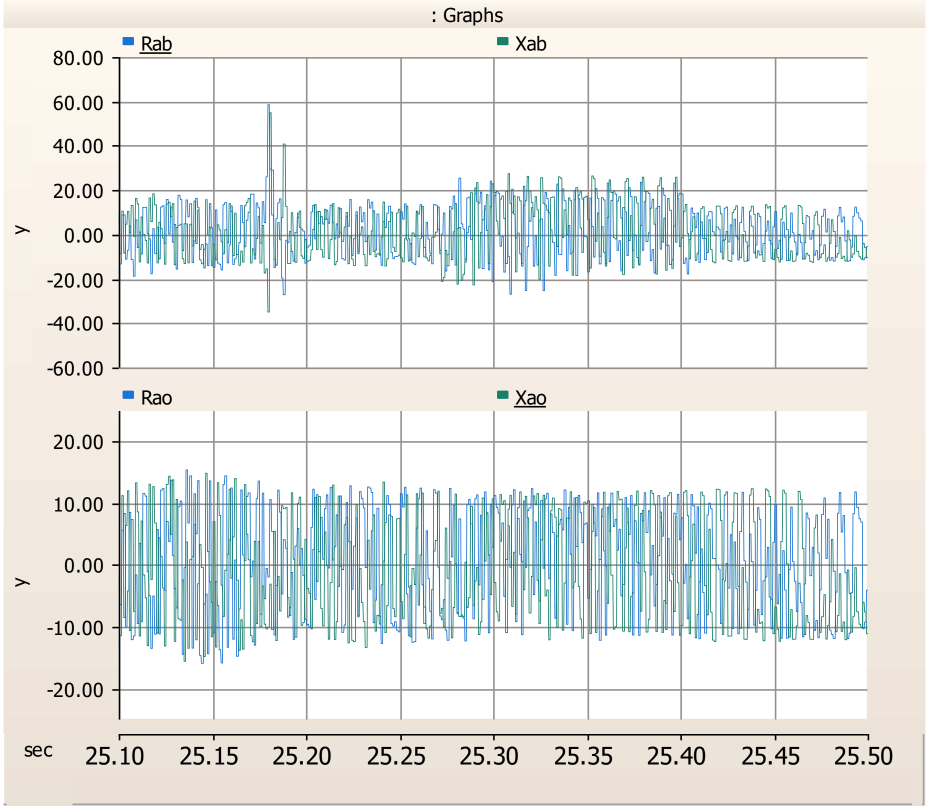

Figure 54. Impedances during the 2L fault calculated using voltages and currents from Meter 3 (off-grid mode).

3.7.1.3. 3LG fault at Old Forge cleared by breaker: OFF-GRID MODE

Simulations were run to investigate the behavior of the system if the 3LG fault described in Section 3.7.1.1 were cleared by operation of a breaker instead of self-clearing. To achieve this, an extra breaker was added to the system as shown in Figure 55 (the breaker labeled “DR_TEST_BK”). The 3LG fault on the Old Forge 46 kV bus occurs at t = 25 s, and the breaker DR_TEST_BK was manually tripped at t = 25.4 s to isolate the fault from the rest of the system. DR_TEST_BK also disconnects over half of the load from the BESS, so there is a significant load rejection event associated with opening this breaker.

Figure 56 shows the phase-ground voltages at Meter 1 during this event, and Figure 57 shows the phase currents measured at Meter 1. When the breaker opens at 25.4 s, the inverter immediately reduces its output current, but the voltage rises quickly and the BESS trips at t = 26.2 s on overvoltage.

This behavior should be discussed with the manufacturer as it is a serious concern if the inverter cannot ride through the load rejection caused by operation of protection—in that case protection is almost moot because the entire system will be blacked out anyway. It is not fully clear how realistic the inverter PSCAD model behavior is in this specific circumstance, and that should be investigated further.

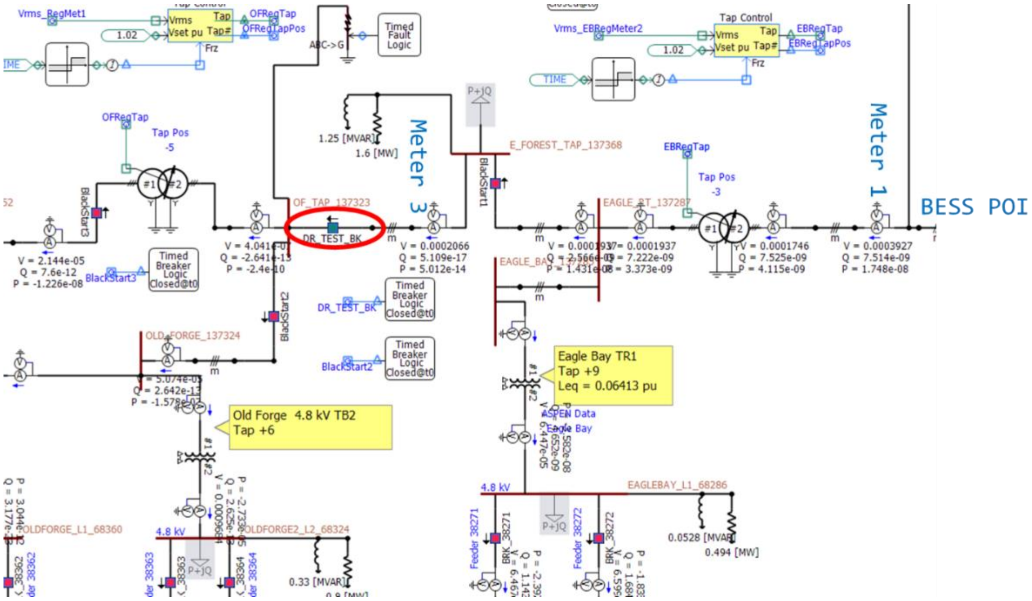

Figure 55. Portion of the one-line diagram of the Old Forge system showing the locations of Meter 1, Meter 3, and the circuit breaker DR_TEST_BK added to clear the fault on the Old Forge 46 kV bus.

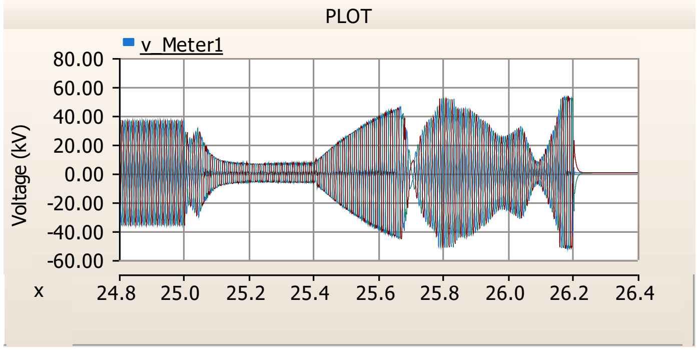

Figure 56. Phase-ground voltages at Meter 1 before, during and after a 3LG fault on the Old Forge 46 kV bus that is cleared by the breaker shown in Figure 55 (off-grid mode).

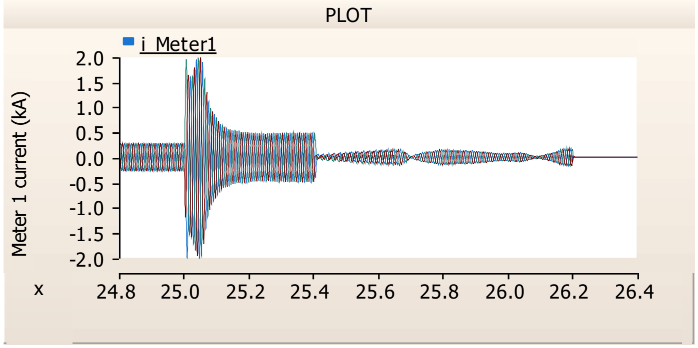

Figure 57. Phase currents at Meter 1 before, during and after a 3LG fault on the Old Forge 46 kV bus that is cleared by the breaker shown in Figure 55 (off-grid mode).

3.7.2. Distribution-level fault currents: OFF-GRID MODE

The PSCAD model was used to determine the 1LG and 3LG fault currents for faults on the low-voltage side of each distribution transformer connected to the 46 kV Old Forge circuit. The point of these simulations is to facilitate comparisons between the on-grid and off-grid fault currents for faults on the distribution secondaries, to determine whether conventional coordinated overcurrent protection will still work on the distribution circuits. Figure 58 shows these results. The six sub-plots in Figure 58 correspond to six fault locations, on the secondary sides of the Eagle Bay, Old Forge #2, Old Forge #1, White Lake, Alder Creek #2, and Alder Creek #1 distribution transformers, respectively. The location of the fault is shown by a yellow lightning bolt in each subplot. For each fault type (1LG and 3LG) and location, values are shown for the sequence components of the pre-fault current (the darker red numbers) and of the fault current (bright red numbers). Fault currents are all given in amperes.

Fault at Eagle Bay distribution transformer 4.16 kV bus
All currents are in A

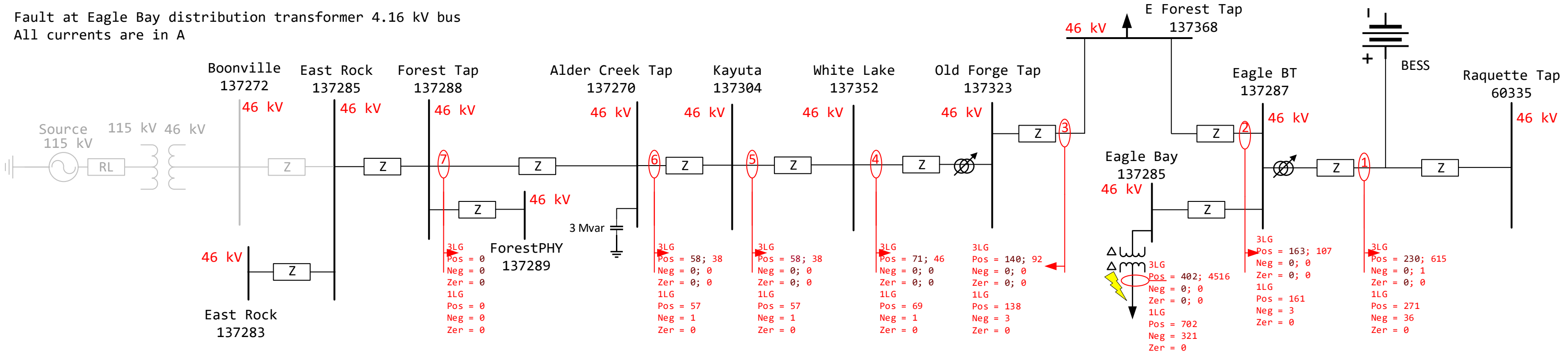

Fault at Old Forge distribution transformer #2 (5 MVA) 4.16 kV bus
All currents are in A

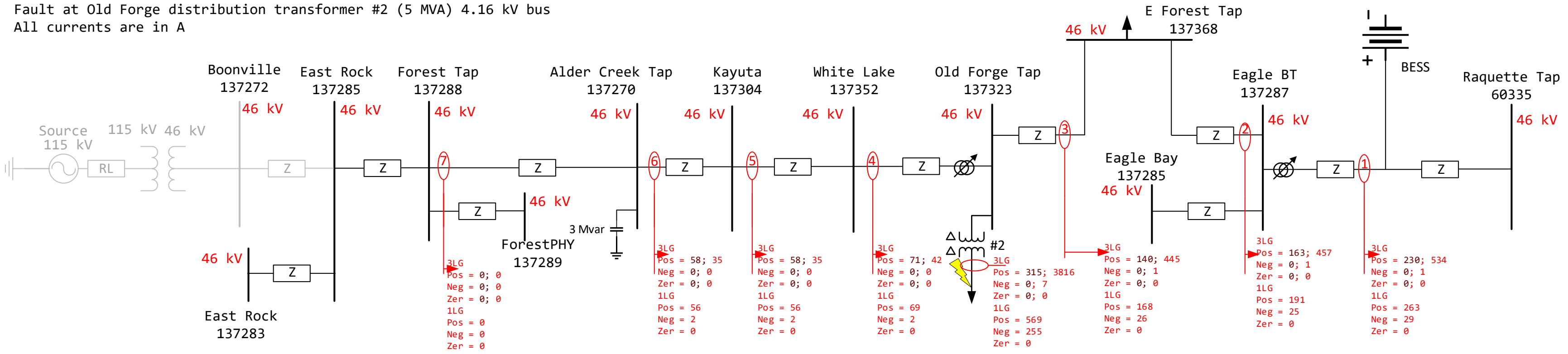

Fault at Old Forge distribution transformer #1 (3.75 MVA), 4.16 kV bus
All currents are in A

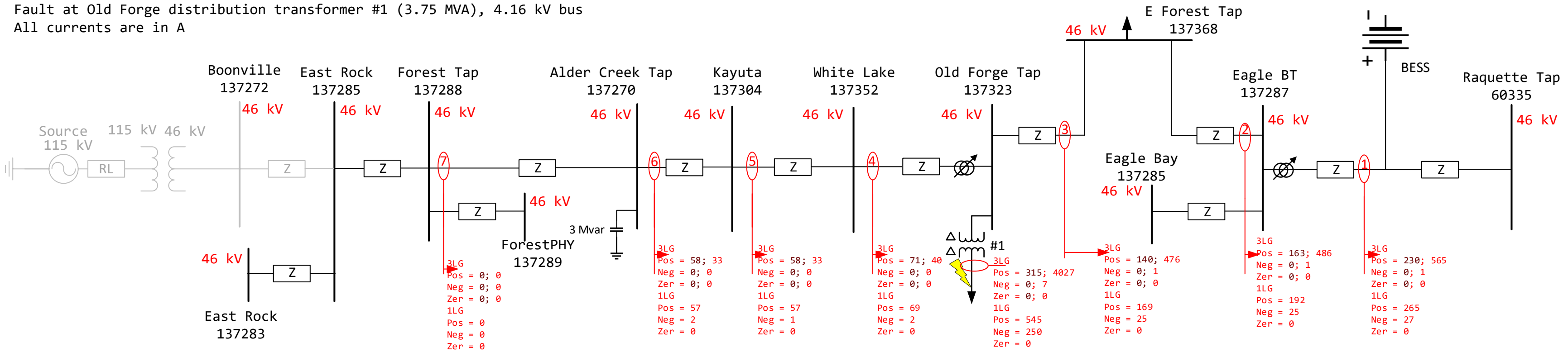

Fault at White Lake distribution transformer 4.16 kV bus
All currents are in A

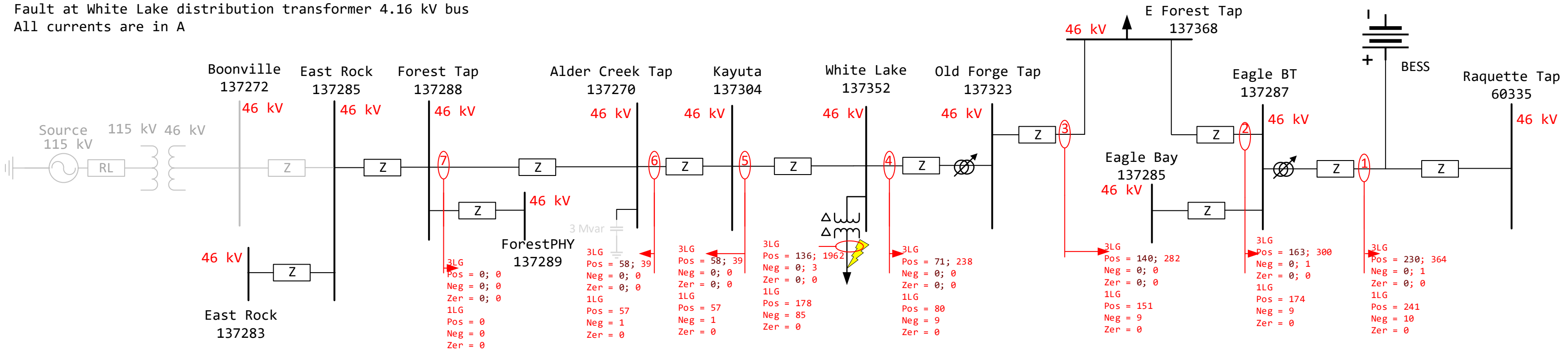

Fault at Alder Creek #1 distribution transformer 4.16 kV bus
All currents are in A

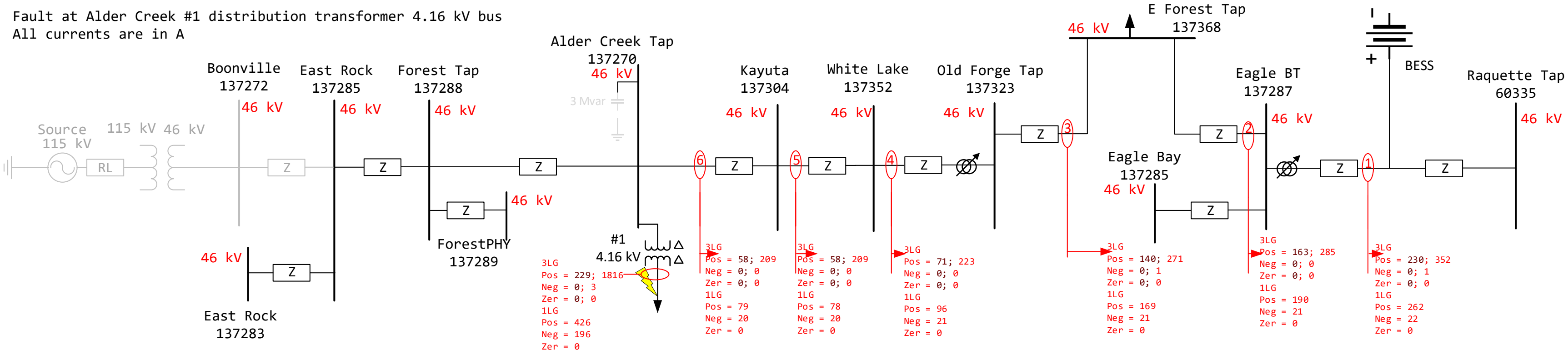

Fault at Alder Creek #2 distribution transformer 13.8 kV bus
All currents are in A

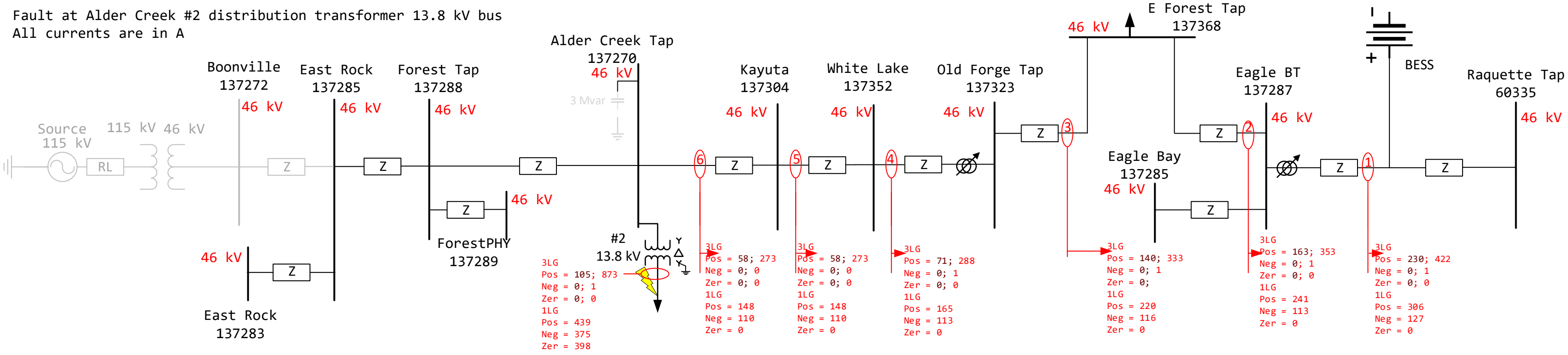

Figure 58. Plots showing the sequence components of the currents measured at various locations on the Old Forge system in the off-grid mode during faults on the secondary sides of each distribution transformer.

3.7.3. *Comparison of 46 kV bus on- and off-grid 3LG fault currents*

The PSCAD model was used to determine the fault currents seen by the protective relays during both on-grid and off-grid operation, to facilitate development of protection settings in both modes. The results are given in Table 8 and Figure 59. The "Meter #" gives the number of the meter at which the fault current is being measured (see Figure 15). The locations across the top of the table show the bus fault locations, and the "ON" and "OFF" columns give the fault currents for the on- and off-grid modes respectively. Because the BESS inverters are significantly oversized, the 3LG fault currents in the off-grid mode exceed their on-grid counterparts in every case.

Table 8. Comparison of 3LG fault currents for on- and off-grid modes of operation. The meter numbers correspond to the meters shown in Figure 15. The names across the top are bus names (also shown in Figure 15).

	Alder Creek		**Kayuta**		**White Lake**		**Old Forge**		**E Forest**		**Eagle Bay**	
Meter #	ON	OFF	ON	OFF	ON	OFF	ON	OFF	ON	OFF	ON	OFF
6	434	563										
5	434	563	442	571								
4	406	565	413	574	477	716						
3	364	609	403	637	457	758	515	1162				
2	408	622	414	632	459	768	516	1163	518	1164		
1	424	687	430	696	475	838	523	1243	524	1241	514	1254

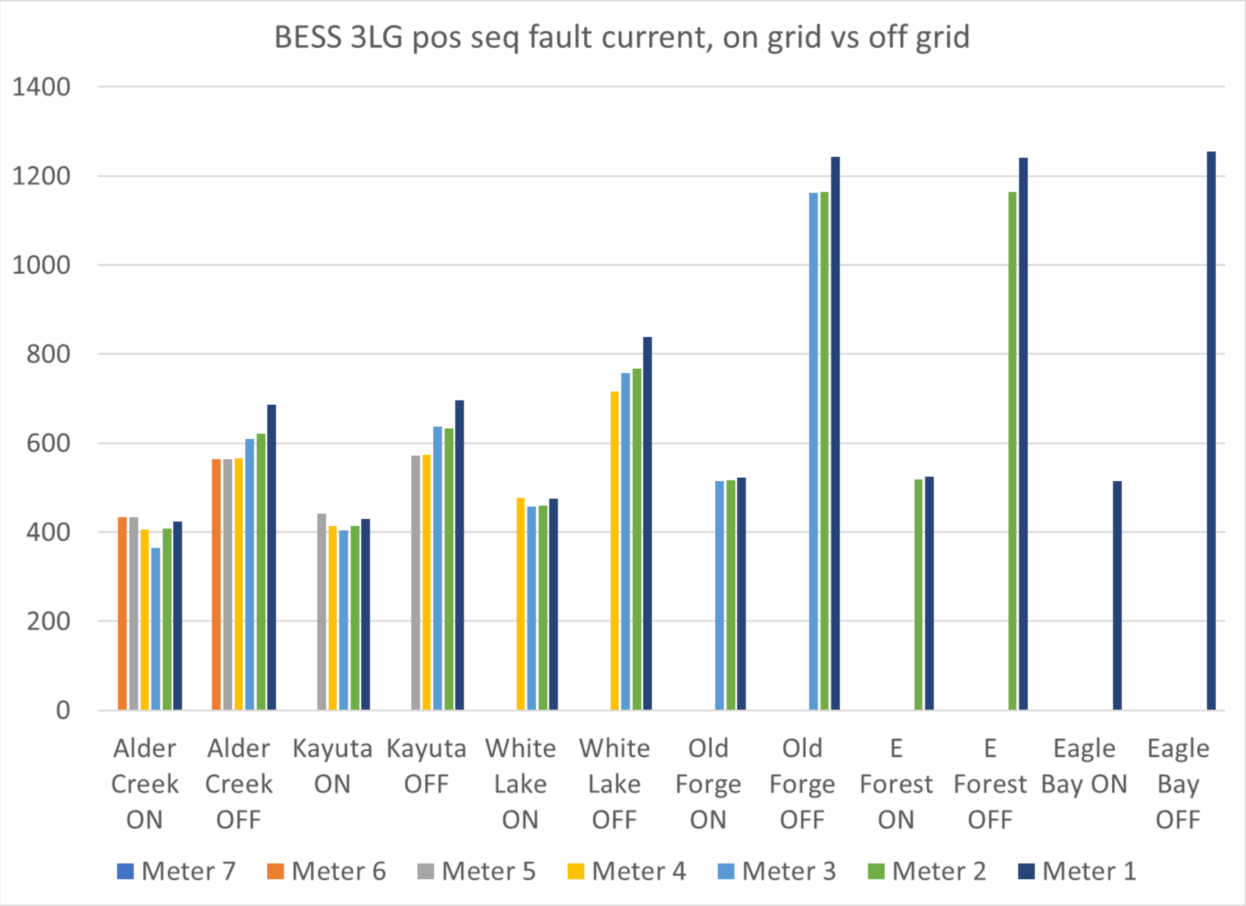

Figure 59. Plot of the data in Table 8.

3.8. Old Forge Protection Design

A preliminary protection scheme was designed for the 46 kV sub-transmission system to accommodate the BESS. Since, the BESS can operate in either the off-grid or the on-grid mode, directional overcurrent protection relays were utilized in the design as this facilitates the detection of the direction of the fault current. Two sets of settings were computed based on whether the BESS is in the off-grid or on-grid mode. Then the relay settings can be switched based on the operating mode of the BESS. Directional overcurrent relays use the phase relationship of voltage and current to determine the direction of the fault current and is ideal for a system where there are two or more generating sources. Directional algorithms are used to detect the direction of the current in such protection relays. For instance, the directional overcurrent element model in PSCAD provides two directional algorithms by default:

1. Algorithm 1 is based on ERL phase relays. This algorithm uses either of the negative-sequence, zero-sequence, or positive-sequence quantities (voltages and currents), depending on relay settings and system conditions at the time of the fault to determine the direction of fault current.
2. Algorithm 2 is based on the SEL relays. This algorithm also utilizes either the negative-sequence, zero-sequence, or positive-sequence quantities. Users can specify a priority order that include one or more of the elements for ground overcurrent supervision, but in the case of phase overcurrent supervision, negative sequence voltage polarized elements have the priority.

It should be noted that this section just provides a preliminary design of the possible protection scheme using directional overcurrent protection elements. The applicability of the proposed design has to be further validated considering factors such as whether the algorithms in directional overcurrent relays can properly detect directionality or not and does the loading conditions in the feeder allow for the use of overcurrent protection or whether distance protection is more suitable.

3.8.1. *Directional Protection Design for 46 kV System (Off Grid mode)*

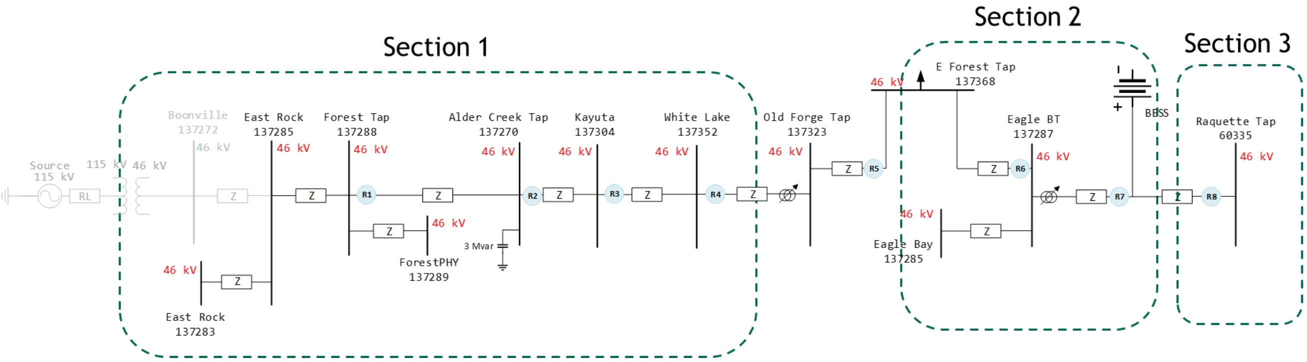

Figure 60. 46 kV distribution system in off grid mode with BESS and relay locations.

When the BESS is in the off-grid mode a fault analysis was carried out in PSCAD with faults applied to every 46 kV bus in the network. For both 3LG and 1LG case, the faults were computed with fault impedances of 0.0001Ω. The results of the faults analysis are summarized in the following figures:

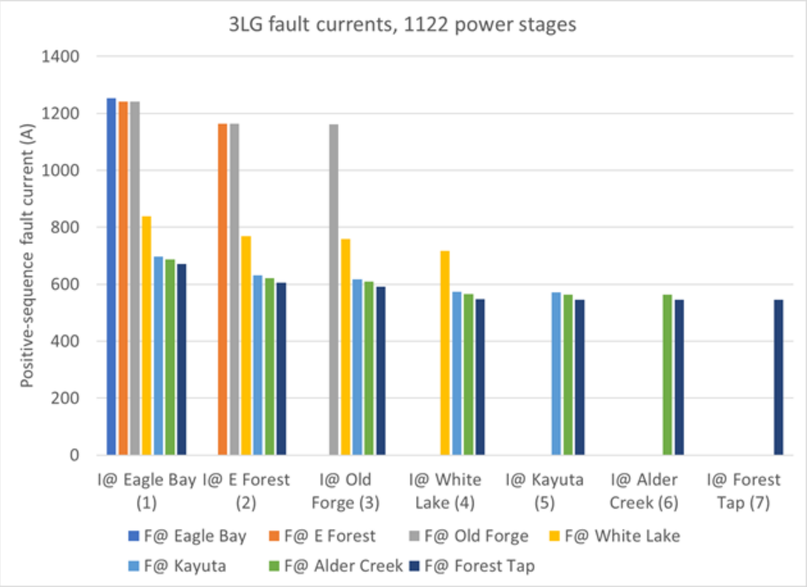

Figure 61. Positive-sequence fault current for 3LG faults at different locations in the network (Off-Grid Case).

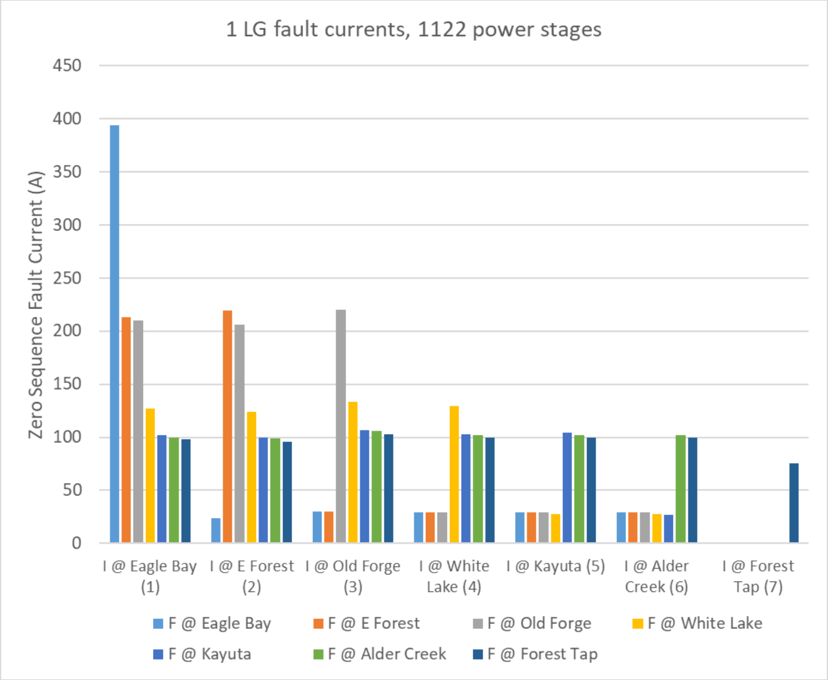

Figure 62. Zero-sequence fault current for 1LG faults at different locations in the network (Off-Grid Case).

Based on Figure 60, three sections for the protection system design were identified:

- Faults at Eagle Bay, E Forest Tap, and Old Forge all produced fault currents between 1100 A and 1300 A.
- Faults at all other 46 kV locations to the left of the BESS point of interconnection all produced fault currents between 500 and 700 A.
- Raquette Lake is a section by itself because it is on the right side of the BESS point of interconnection.

For Raquette Lake, directional elements are not required for protection design as the power flow will always be unidirectional. For proper operation, only the current pickup settings needs to be switched between the on and off-grid cases. For the remaining sections, directional overcurrent can distinguish between faults by setting different current pickup for the two sections. Further coordination can be achieved through the time delay elements as well. For the design of the protection scheme, a coordination time interval of 0.15 s is assumed between the relays. It is assumed that the current transformers (CTs) associated each of the relays has a CT ratio of 200:5. Furthermore, the relays are assumed to be programmed with SEL U1 moderately inverse time characteristic curve which is given by the following equation:

$$t = TDS\left(\frac{k}{M^{\alpha} - P} + c\right) + B$$

where *t* is the operating time, *TDS* is the time dial settings, *M* is the multiples of the pickup current, and *k*, *a*, *c*, and *B* are parameters specific to the type of the relay curve. For the SEL U1 curve, these parameters are set to 0.014, 0.02, 0.0226, and 0 respectively. The computed settings of the relays are shown in Table 9. Similarly, Figure 63(a) and Figure 63(b) and show the time coordination aspects of the protection design.

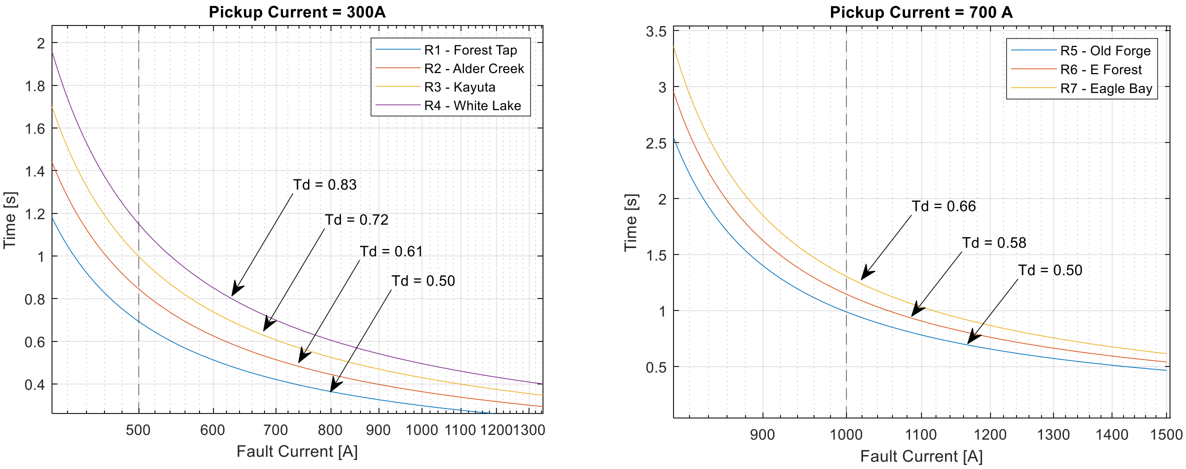

(a) **(b)**

Figure 63. Time dial settings for relays (Off grid mode, 3LG faults)

Table 9. Relay settings (Off grid mode, 3LG faults).

Relay Name	Pickup Current	TDS
R1 @ Forest Tap	300 A	0.50
R2 @ Alder Creek	300 A	0.61
R3 @ Kayuta	300 A	0.72
R4 @ White Lake	300 A	0.83
R5 @ Old Forge	700 A	0.50
R6 @ E Forest	700 A	0.58
R7 @ Eagle Bay	700 A	0.66
R8 @ Raquette Lake	700 A	0.50

Similar observations regarding the sections can be made for the 1LG faults based on Figure 62. For the measurement of zero-sequence currents, the CTs typically outputs $3I_0$ value for the zero-sequence current. This factor has to be considered in the design of the protection scheme. The settings of the relays for the 1LG fault case are shown in Table 10. Similarly, Figure 64(a) and Figure 64(b) show the time coordination aspects of the design.

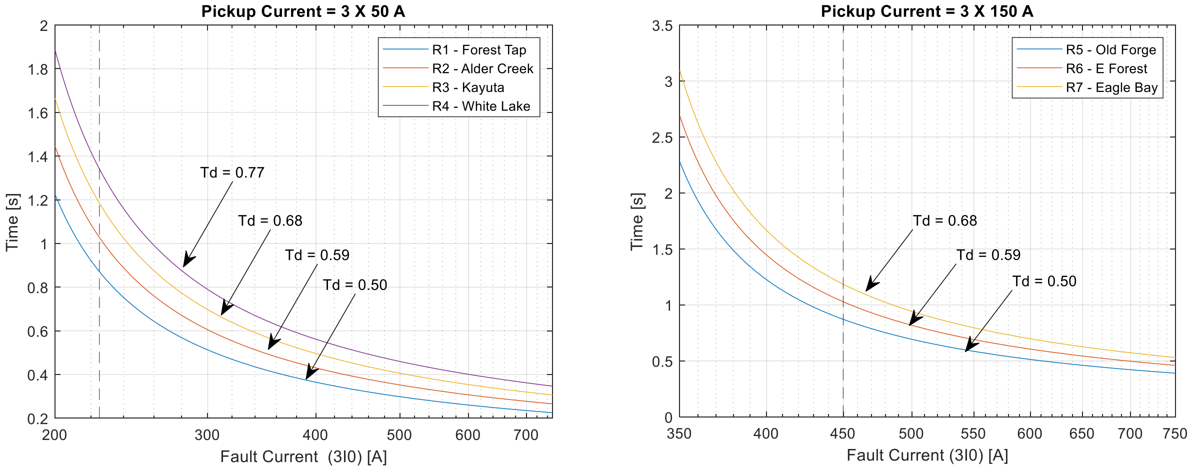

(a) **(b)**

Figure 64. Time dial settings for relays (Off grid mode, 1LG faults).

Table 10. Relay settings (Off grid mode, 1LG faults).

Relay Name	Pickup Current	TDS
R1 @ Forest Tap	3 x 50 A	0.05
R2 @ Alder Creek	3 x 50 A	0.14
R3 @ Kayuta	3 x 50 A	0.23
R4 @ White Lake	3 x 50 A	0.32
R5 @ Old Forge	3 x 100 A	0.14
R6 @ E Forest	3 x 100 A	0.23
R7 @ Eagle Bay	3 x 100 A	0.32
R8 @ Raquette Lake	3 x 100 A	0.05

3.8.2. Directional Protection Design for 46 kV System (On Grid mode)

Similarly, fault analysis is also performed for the on-grid mode when the BESS is operating in the synthetic-inertia mode. To check the desensitization of the protection scheme with the BESS, Figure 65 compares the 3LG positive sequence fault current sourced by the grid with and without the BESS. The figures suggest that desensitization of the grid-side protection by the BESS is not an issue for this system as the fault currents are essentially same regardless of whether or not the BESS in connected. This means the protection system can be designed based on the fault current sourced from the grid regardless of the BESS. The fault current for the 1LG faults are plotted in Figure 66.

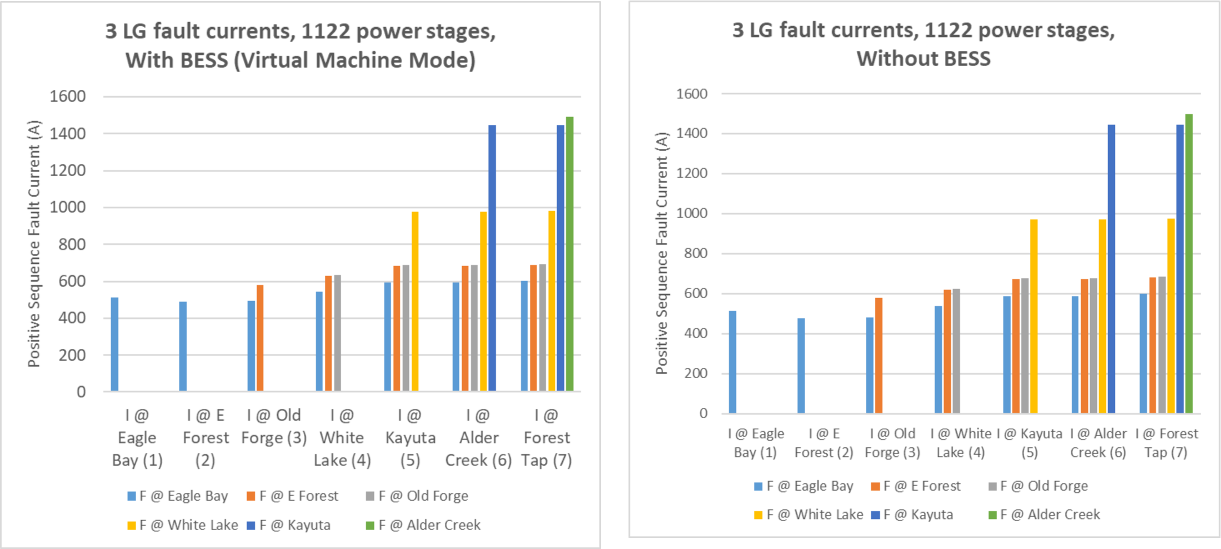

(a) (b)

Figure 65. Comparison of on-grid fault current sourced from the grid with and without the BESS for 3LG faults.

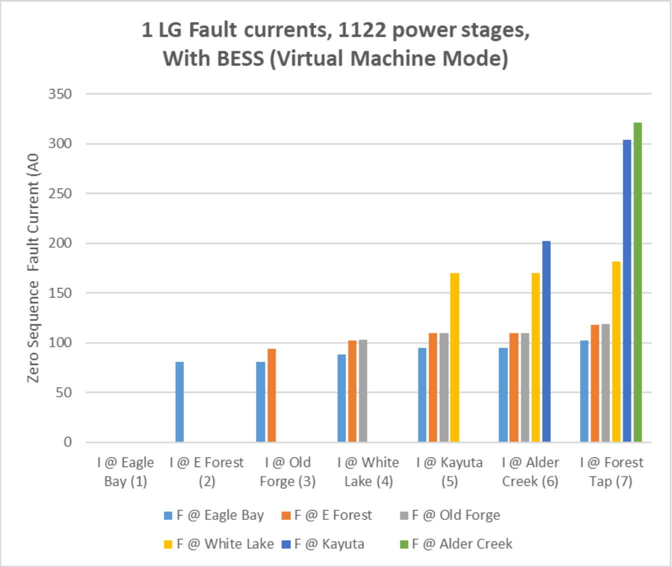

Figure 66. Fault current sourced from the grid + BESS for 1LG faults, on-grid mode.

Table 11 compares fault currents sourced by the BESS for the on-grid and the off-grid cases. Compared to the off-grid cases, the fault currents in the on-grid case are much lower. Also, it can be observed that the faults currents are nearly independent of the fault location. If a protection scheme with fault currents being sensed from the BESS side is desired for the on-grid case, different settings and possibly different protection types will be required for the on-grid and off-grid modes for the directional protection elements and to ensure the relays do not trip on load. However, the plan of the system operator is to the direct transfer trip(DTT) the upstream breakers so a protection system was not designed for this case. In general for the grid-parallel mode, the 46 kV recloser scheme is only being used for fault current flowing from the transmission system, which can be accomplished by means of directional blocking on all 46 kV reclosers. The BESS and the protection between the BESS and fault is designed to ride through the fault until disconnected by the DTT.

Table 11. Fault Current Sourced by the BESS for On-Grid and Off-Grid Mode for 3LG Faults.

	F @ Alder Creek ON GRID	F @ Alder Creek OFF GRID	F @ Kayuta ON Grid	F @ Kayuta OFF Grid	F @ White Lake ON Grid	F @ White Lake OFF Grid	F @ Old Forge ON Grid	F @ Old Forge OFF Grid	F @ E Forest ON Grid	F @ E Forest OFF Grid	F @ Eagle Bay ON Grid	F @ Eagle Bay OFF Grid
I @ Alder Creek (6)	434	563										
I @ Kayuta (5)	434	563	442	571								
I @ White Lake (4)	406	565	413	574	477	716						
I @ Old Forge (3)	364	609	403	637	457	758	515	1162				
I @ E Forest (2)	408	622	414	632	459	768	516	1163	518	1164		
I @ Eagle Bay (1)	424	687	430	696	475	838	523	1243	524	1241	514	1254

Based on Figure 65 (a), two sections for the protection system design were identified as illustrated in Figure 67:

- Faults on Raquette, Eagle Bay, E Forest, and Old Forge all produced fault currents in range of 400 A to 700A.
- Faults on White Lake, Kayuta, and Alder Creek produced fault currents in the range of 900 to 1400 A.

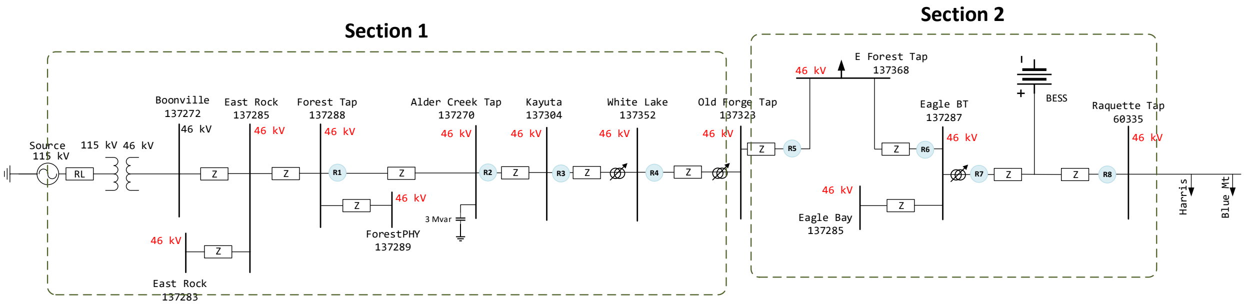

Figure 67. 46 kV distribution system in on grid mode with BESS and relay locations.

For the protection design of on-grid case, a SEL U1 curve is used for the relay with parameters set to 0.014, 0.02, 0.0226, and 0 respectively. The simulation results from PSCAD showed that the fault at Raquette Lake resulted in large oscillations sourced from the BESS causing the BESS to trip under 1s post-fault as shown in Figure 68 (such oscillations were not observed for faults at other locations). After the BESS trips, the fault current is supplied by the grid. The peaks were measured at more than twice the steady-state fault level from the grid. Hence, for the Relay R8 an instantaneous overcurrent protection setting combined with a time-overcurrent protection coordinated with rest of the relays in the system is recommended. The aim of the instantaneous overcurrent protection is to operate the relay quickly if such large oscillations are in fact observed in the real system. The computed settings of the relays are shown in Table 12. Similarly, Figure 69(a) and Figure 69(b) and show the time coordination aspects of the protection design.

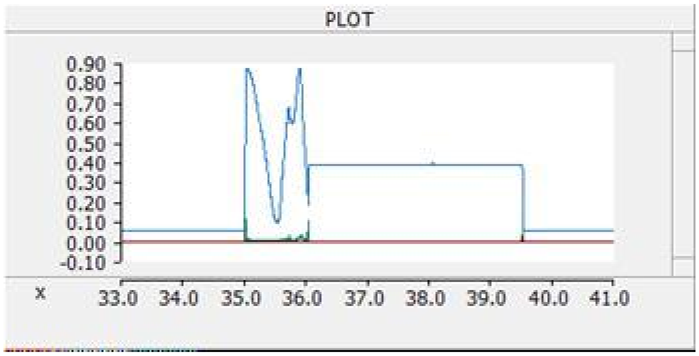

Figure 68. Sequence currents measured at Meter 0 during a 3LG fault at Raquette Lake.

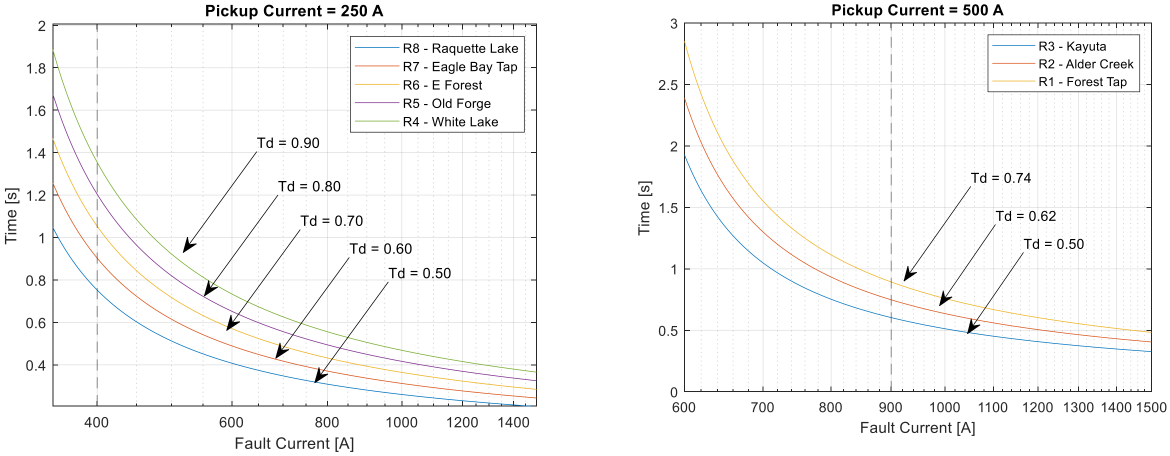

(a) **(b)**

Figure 69. Time dial settings for relays (On grid mode, 3LG faults).

Table 12. Relay settings (On grid mode, 3LG faults).

Relay Name	Pickup Current	TDS
R1 @ Forest Tap	500 A	0.74
R2 @ Alder Creek	500 A	0.62
R3 @ Kayuta	500 A	0.50
R4 @ White Lake	250 A	0.90
R5 @ Old Forge	250 A	0.80
R6 @ E Forest	250 A	0.70
R7 @ Eagle Bay	250 A	0.60
R8 @ Raquette Lake	250 A	0.50

Similarly, computed settings of the relays for 1LG case are shown in Table 13 and the coordination aspects of the protection design are illustrated in Figure 70(a) and Figure 70(b).

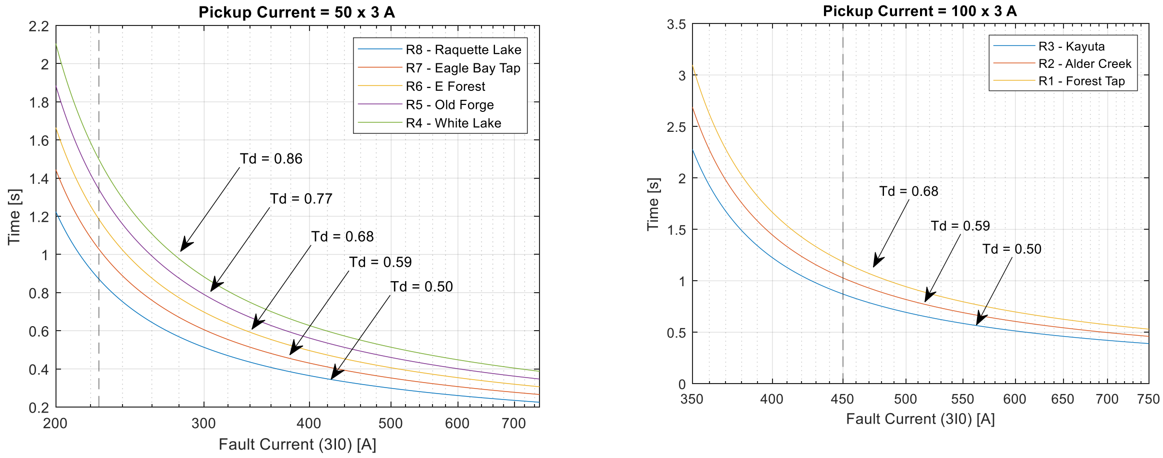
Pickup Current = 50 x 3 A

Pickup Current = 100 x 3 A

(a) **(b)**

Figure 70. Time dial settings for relays (On grid mode, 1LG faults).

Table 13. Relay settings (Off grid mode, 1LG faults).

Relay Name	Pickup Current	TDS
R1 @ Forest Tap	500 A	0.74
R2 @ Alder Creek	500 A	0.62
R3 @ Kayuta	500 A	0.50
R4 @ White Lake	250 A	0.90
R5 @ Old Forge	250 A	0.80
R6 @ E Forest	250 A	0.70
R7 @ Eagle Bay	250 A	0.60
R8 @ Raquette Lake	250 A	0.50

3.8.3. Critical Clearing Time for the BESS in on-grid Synthetic Inertia Mode operation

Another important observation from the fault studies with BESS in the Synthetic Inertia Mode was the presence of a critical clearing time (CCT) as shown in Figure 71. The reader is reminded that the key reason for using the Synthetic Inertia Mode while on-grid was that this mode improved the ride-through capability of the BESS during remote transmission faults, relative to standard grid-following controls. However, while the Synthetic Inertia Mode improved ride-through for remote faults, simulations suggested that in some cases there were very short critical clearing times for the inverter in this mode during close-in 3LG faults. Referring to Figure 71, for the 3LG case, if the fault does not clear prior to CCT the BESS becomes unstable and trips. For the 1LG case, if the fault does not clear by the CCT then the BESS trips only after the fault clears. This shows that overcurrent coordination may not work in some cases and some form of communication-based protection scheme may be more suitable. However, it is possible that this CCT issue may not be a problem in this application because it only occurs in situations in which the BESS must trip anyway (i.e., a fault between the BESS and the Boonville bus).

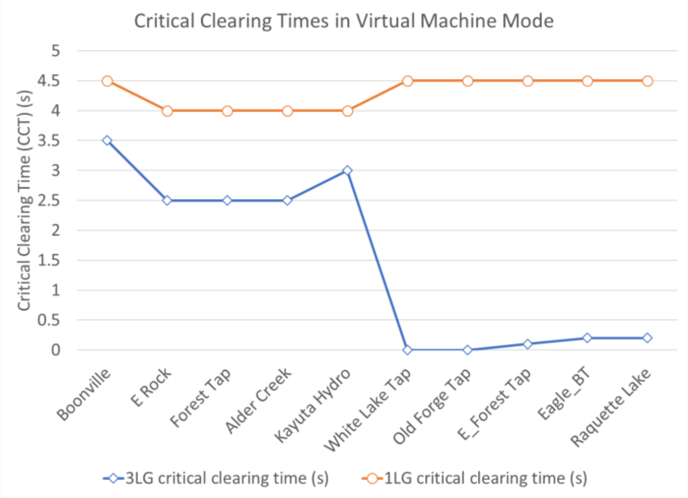

Figure 71. Presence of Fault Clearing Times with BESS in Synthetic Inertia Mode.

3.9. Dynamic simulations using a generic inverter model

To further improve fundamental understanding of the dynamics of this system, and also as a precursor to the hardware-in-the-loop work described below, additional simulations were run using the Simulink power system model described in Section 0, and a generic inverter model.

The generic GFMI used in this work includes the Center for Electric Reliability Technology Solutions (CERTS) droop control scheme. Figure 72 illustrates the block diagram for the CERTS GFMI model. This CERTS-based GFMI control utilizes frequency-droop and voltage-droop characteristics to regulate active and reactive power, respectively. Before implementing the droop control scheme, the output variables i_0 and v_0 are mapped into the *αβ-frame*. The transformed values of voltage and current are used to calculate active and reactive power, as shown in equations (7) and equation (8), respectively.

$$P = \frac{3}{2} \cdot \left(v_{0\alpha} \cdot i_{0\alpha} + v_{0\beta} \cdot i_{0\beta} \right) \tag{7}$$

$$Q = \frac{3}{2} \cdot \left(-v_{0\alpha} \cdot i_{0\beta} + v_{0\beta} \cdot i_{0\alpha}\right) \tag{8}$$

In these equations, the variable $v_{0\alpha}$ and $i_{0\alpha}$ represent the alpha voltage and current values, while the variable $v_{0\beta}$ and $i_{0\beta}$ represent the beta voltage and current values of the *αβ*-frame. A proportional-integral (PI) controller is implemented to regulate the voltage reference provided by the voltage droop stage. The use of a PI controller helps improve the voltage regulation by minimizing any circulating currents that might be present throughout the system. The output peak voltage provided to this control stage is also calculated in the *αβ-frame* as shown in equation (9).

$$V_{0\,peak} = \sqrt{v_{0\alpha}^2 + v_{0\beta}^2} \tag{9}$$

A more advanced feature of the CERTS- based GFMI control scheme includes the use of an overload mitigation regulator, which helps to prevent the GFMI from DC bus voltage collapse by introducing a second control loop that reduces the inverter’s frequency in cases where it may become overloaded. For simplicity, this control loop scheme was omitted since proper precautions were taken during simulations to avoid overloading the inverter under steady state conditions. The parameters of the GFMI simulation model are shown in Table 14.

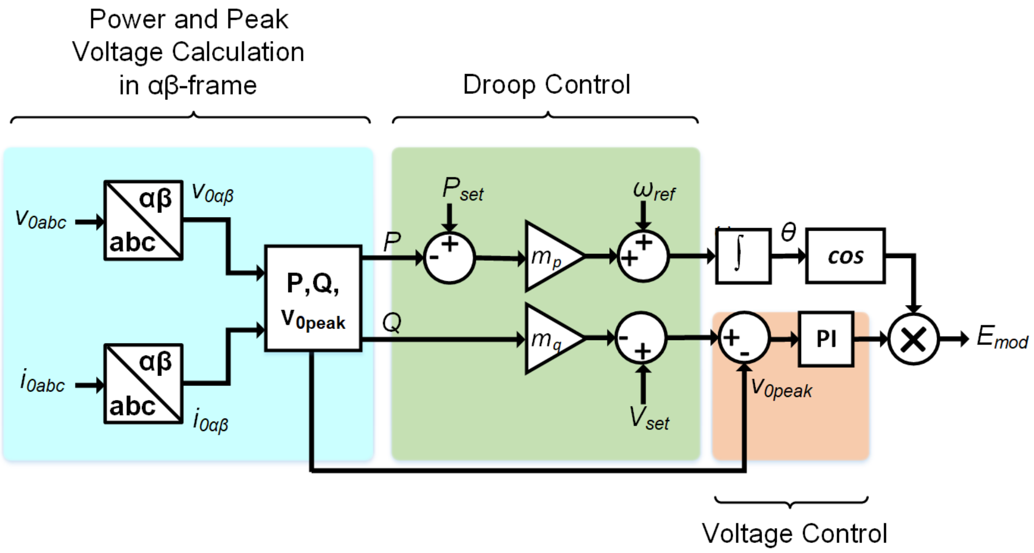

Figure 72. Block Diagram Describing the CERTS Grid Forming Inverter Control Scheme.

Table 14. Grid Forming Inverter Simulation Model Parameters

Parameter	Value	Unit
Rated Power	20	MVA
Voltage	480	V
Switching Frequency	19800	Hz
DC Voltage	1500	V
DC Capacitance	0.01	F
Proportional Gain	0.1	-
Integral Gain	5.84	-

3.9.1. Modeling GFMIs current limiting capabilities

When a fault occurs, it is expected that inverters will enter a current-limiting mode. One type of current-limiting mode keeps the current below the inverter's output current limit by clipping the peaks of the inverter output current. If an inverter that employs this clipping-based current limiting were deployed, the clipping of fault current waveforms contributed by the BESS may cause some issues in the design of the protection scheme and interactions with utility system reclosers and other devices. This would be due to the harmonic distortion of the waves and certain chaotic waveform conditions at times. To better understand this effect, the fault limiting nature of the inverter controller was examined in this section..

The CERTS control scheme was modified to implement the aforementioned clipping-based current protection scheme as shown in Figure 73. The αβ components of the current and voltage are the inputs to the constant-current curtailment protection block, which in return provides the control (triggering) signal and the saturation voltage limits to the dynamic-saturation block that follows the modulated signals from the voltage and frequency-droop control blocks. The impedance Z_{crit} is defined by the point at which the inverter is operating at its maximum output voltage and current, as shown in Figure 74.

In order to compare the dynamics under fault scenarios of the model depicted in Figure 73, experimental tests were performed on a commercially available single-phase inverter, hereinafter referred to as the device under test 1 (DUT 1). DUT 1 is a 5 kW rated GFMI operating at a voltage level of 240 V. Its voltage and current traces under a ground fault with an impedance of $Z_f = 2.4\ \Omega$, is compared in Figure 75 against the traces generated with the modified CERTS model. The traces labeled as Model 1 represent the phase delay implementation using a derivative block, whereas the traces labeled as Model 2 represent the phase delay implementation using a transport delay.

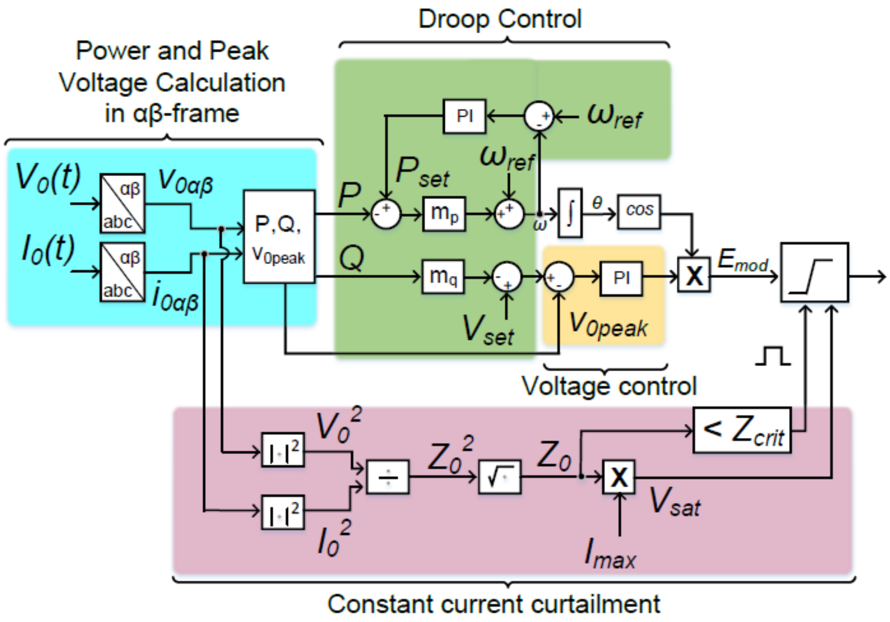

Figure 73. Modified Single-Phase CERTS Control Scheme with Constant-Current Curtailment Protection.

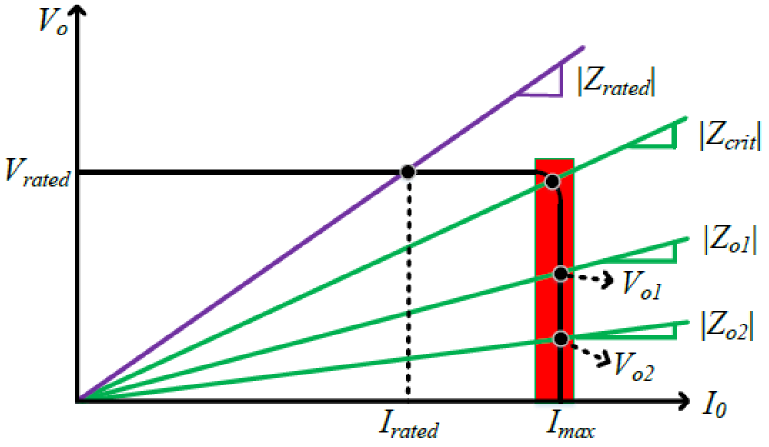

Figure 74. Voltage-Current Characteristics of Constant Current Protection Mode for DC/DC Converters.

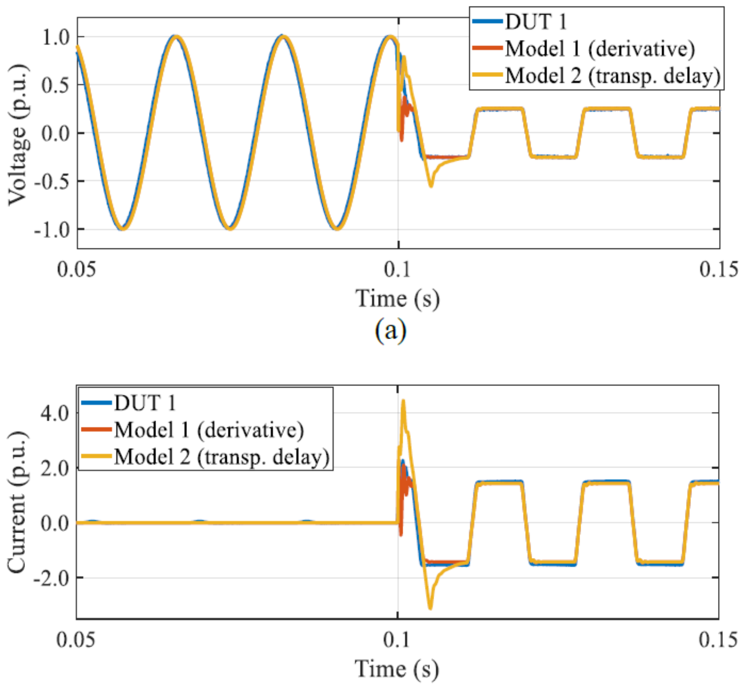

(a)

(b)

Figure 75. Modified Single-Phase CERTS Control Scheme with peak-clipping Current Curtailment Protection: (a) inverter terminal voltage; (b) inverter output current.

3.9.2. Inverter modules stacking

In order to increase the power, and thus the current rating capabilities of GFMIs, inverter manufacturers stack or connect in parallel several H-bridge modules as depicted in Figure 76. Notice that all the stacked H-Bridges (from Bridge 1 to Bridge n) share the same DC link, which is usually the case in large mega-watt scale energy-storage plants. Furthermore, each H-bridge is followed by an inductive-capacitive-inductive (LCL)filter, which smooths out the corresponding voltages and currents. Notice also that the main output of the GFMI is the electrical connection of all of the outputs of each LCL filter.

Including this stacking technique in a simulation model of a large scale energy-storage plant is a good way to emulate a realistic transient or steady state scenario. However, for a large number of stacked modules (n>10), a simulation implemented in a real-time simulator could be easily saturated by overruns and therefore losing the real-time simulation feature. One way to overcome the overruns problem is to increase the simulation time at the expense of losing detailed transient dynamics. A better way to avoid simulation overruns is to simplify the stacked H-Bridges by an equivalent single circuit. From the circuit analysis perspective, the equivalent circuit viewed from the output of the stacked H-Bridges is the Thevenin equivalent impedance of the parallel connection of a total of *n* LCL filters with the source behind the H-Bridges (DC LINK) grounded, as depicted in Figure 77. After the corresponding network analysis, the impedance of the stacked LCL filters can be reduced to a single LCL circuit, with the equivalent values of the components being a function of the number of stacked modules (*n*):

$$R_{1eq} = \frac{R_1}{n} \tag{10}$$

$$L_{1eq} = \frac{L_1}{n} \tag{11}$$

$$R_{2eq} = \frac{R_2}{n} \tag{12}$$

$$C_{2eq} = nC_2 \tag{13}$$

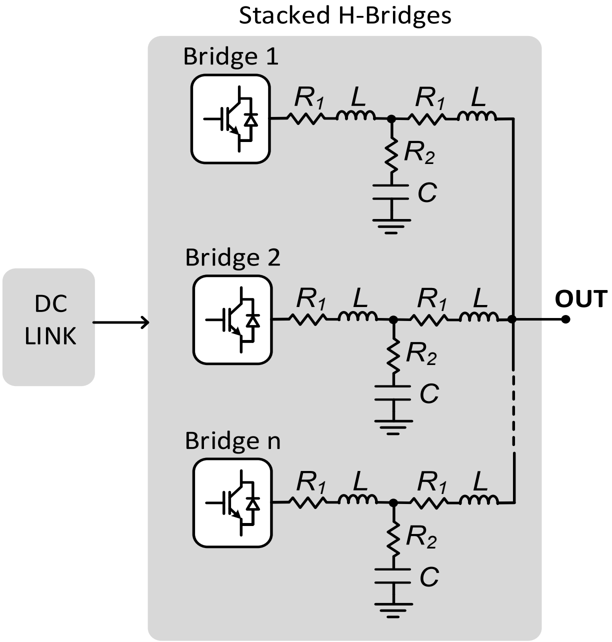

Figure 76. GFMIs stacking

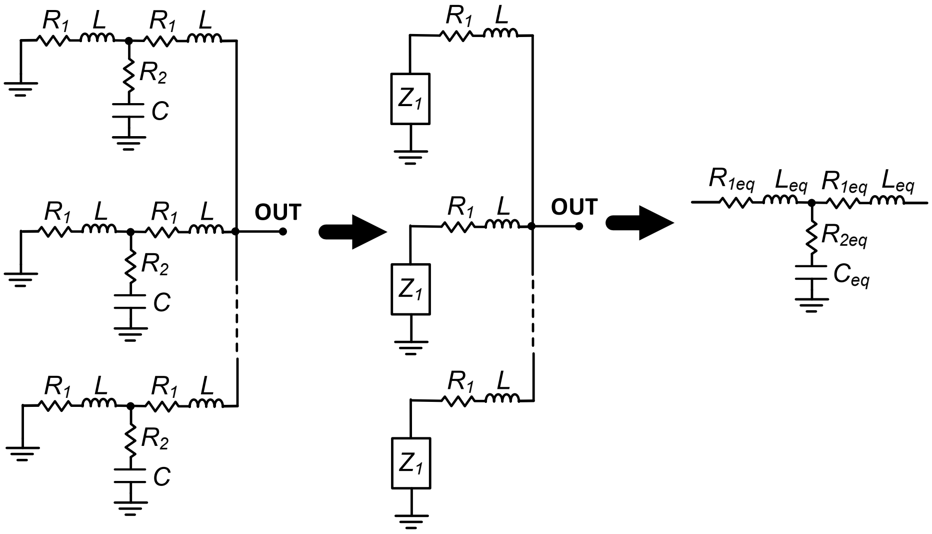

Figure 77. Equivalent LCL circuit derivation.

In order to validate the equivalent circuit equations, a 20 MW GFMI simulation CERTS model was simulated using 40 stacked H-bridges rated 500 kW each. Then the model was simulated using only the equivalent model derived from Eqs (10)-(13). Table 15 shows the values of the LCL filter values for each H-Bridge and the corresponding equivalent LCL circuit.

Table 15. LCL filter values

H-Bridge LCL filter values		Equivalent filter values	
R_1	0.1 Ω	R_{1eq}	0.0025 Ω
L_1	800 μH	L_{1eq}	20 μH
R_2	0.1 Ω	R_{2eq}	0.0025 Ω
C_2	150 μF	C_{2eq}	6000 μF

Simulations' comparisons are depicted in Figure 78. Notice that the equivalent circuit dynamics in frequency, current, and voltage follow the exact dynamics as the simulation with stacked H-bridge modules.

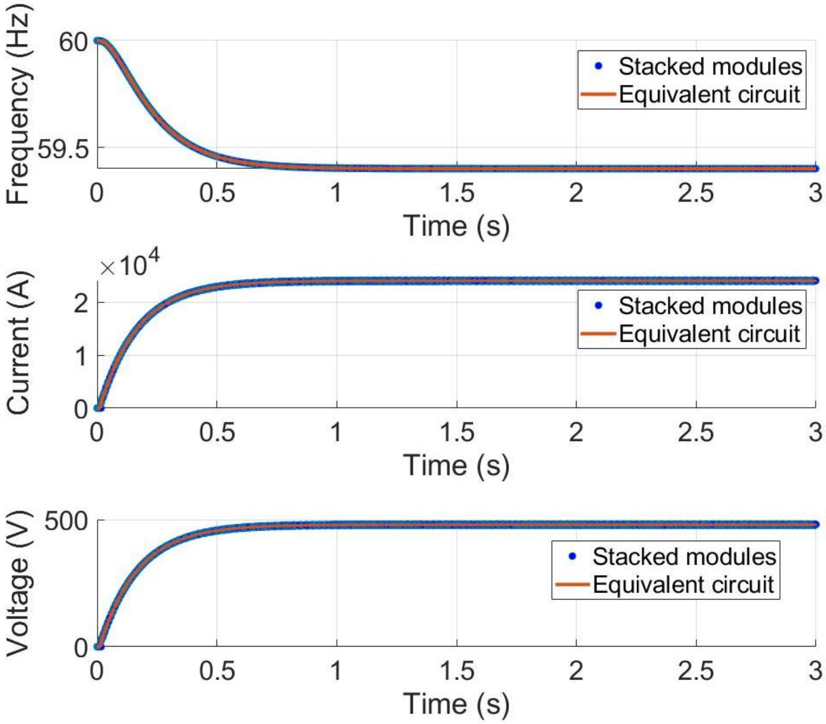

Figure 78. Simulation comparisons that validate the equivalent circuit.

3.9.3. *Seamless on- to off-grid transition*

It is not expected that the Old Forge system will undergo a seamless on- to off-grid transition. However, the generic CERTS-based GFMI described above is capable of such seamless transitions. To demonstrate this, simulations for the National Grid Old Forge system when subjected to a power outage at 5 seconds were obtained. Figure 79 illustrates the GFMIs response when subjecting the Old Forge system to a power outage. The NG system source is supplying the entire load initially and then at 5 seconds the NG source is turned off (bulk source disconnected without a fault condition present) and the BESS suddenly picks up all load. This type of operation would not be the usual transition for the microgrid, which normally occurs as a result of a fault and then the microgrid starts after a period of outage. But this type of transition would be useful for testing of the microgrid or pre-emptive microgrid mode where it is deliberately seamlessly transitioned to that mode.

Notice that initially, due to its location at the end of the 46 kV line, the GFMI provides reactive power to increase the voltage at its PCC. Active power is not provided initially since it is provided primarily from the bulk transmission system. Once the transmission system is disconnected and the Old Forge microgrid is isolated, there is an increase in active power from the BESS in order to supply the system loads. Reactive power is reduced since active power is already increasing the systems voltage. Figure 80 illustrates how there is a slight reduction in voltage at the PCC of the GFMI, when the system is isolated, but quickly increases until reaching nominal voltage. Figure 81 illustrates that although there is a reduction in system frequency once the microgrid is islanded, the frequency response is within the droop settings of 5%.

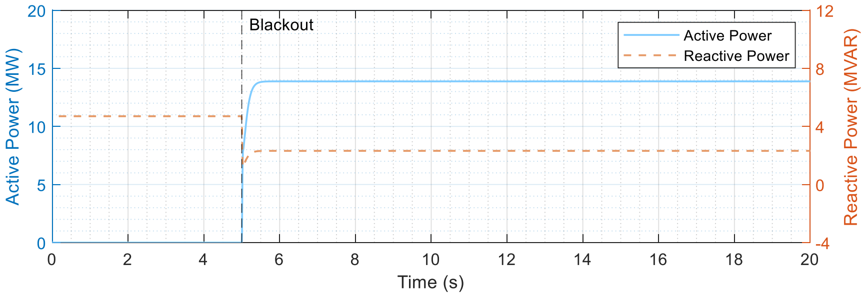

Figure 79. Simulation Results for the Grid Forming Inverter Active and Reactive power obtained when subjecting the Old Forge Distribution System to a Power Outage.

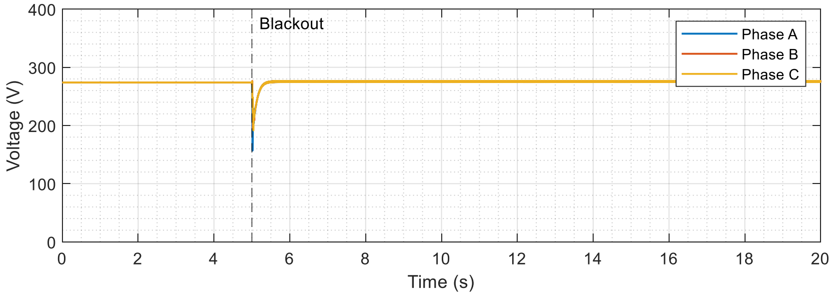

Figure 80. Simulation Results for the Grid Forming Inverter Voltage obtained when subjecting the Old Forge Distribution System to a Power Outage.

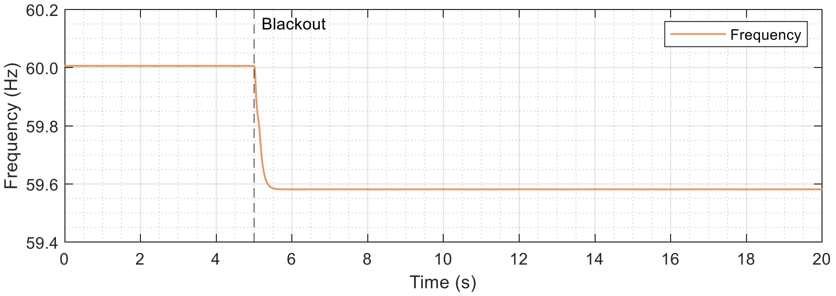

Figure 81. Simulation Results for the Grid Forming Inverter Frequency obtained when subjecting the Old Forge Distribution System to a Power Outage.

These results demonstrate that the simulation model of the GFMI is able to maintain the microgrid operating under blackout conditions. When a blackout condition is introduced, the GFMI provides active and reactive power to regulate the system voltage and frequency.

3.9.4. *Black-Start with the generic GFMI model*

Simulations were also conducted to demonstrate black start of the Old Forge system using the generic CERTS GFMI. In this simulation the National Grid Old Forge system is disconnected from the transmission system and there is no source supplying power to the system loads. The Old Forge system is at zero volts throughout, and then a breaker is closed and the GFMIs frequency and voltage are commanded to provide 60 Hz and 480 V. This scenario represents the normal start-up for the microgrid using the BESS after the outage, similar to the discussion in Section 3.5. Figure 82 illustrates how initially there is no active or reactive power provided by the GFMI. Once the GFMI is connected, it is able to black-start the Old Forge microgrid, supplying its load. Figure 83 illustrates how the voltage increases to its nominal value as soon as the GFMI is connected to the Old Forge microgrid. Figure 84 illustrates that the GFMI frequency is at 60 Hz and as soon as it is connected to the Old Forge microgrid, the frequency droops according to the inverters' frequency droop settings.

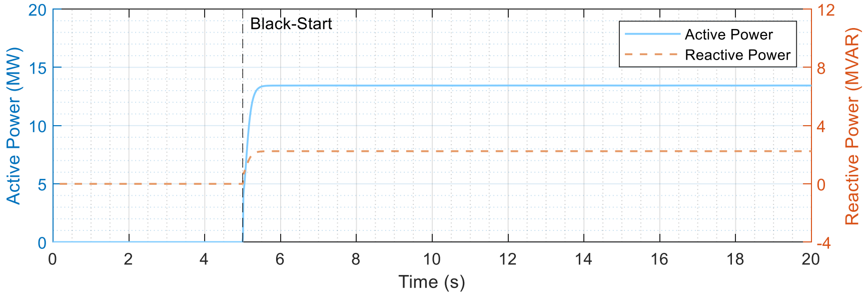

Figure 82. Active and reactive power from the generic CERTS GFMI model during a black start of the Old Forge microgrid.

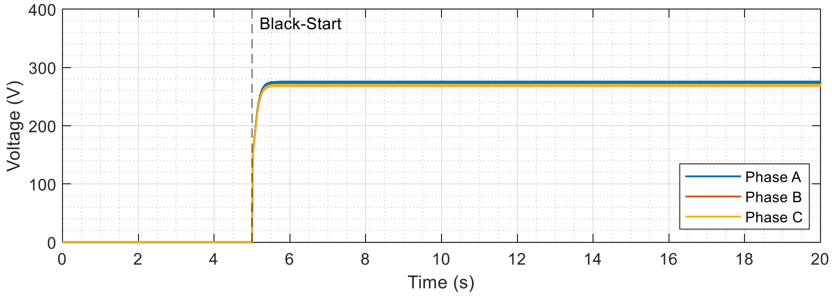

Figure 83. Voltage at the POI of the generic CERTS GFMI during a black-start of the Old Forge microgrid.

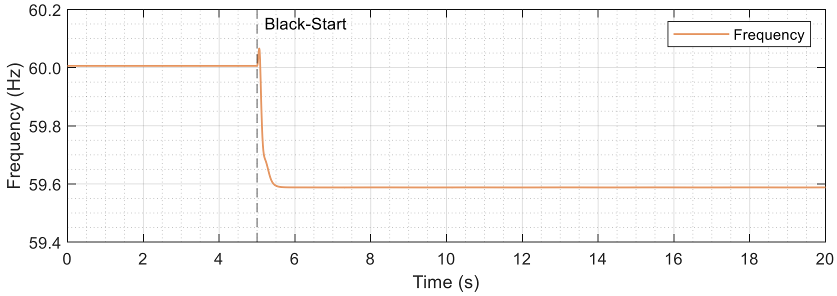

Figure 84. Frequency of the voltage at the generic CERTS GFMI POI during a black-start of the Old Forge microgrid.

One key difference between these black-start results and those shown in section is that in Figure 83 there is no ramp-up of the voltage during the black start; the inverter produces a near step-change in the output voltage. It is also important to note that the system model used in this case did not represent transformer or motor-start inrush currents. Future steps would include adding those inrush currents to the model, and testing a commercial GFMI (ABB PCS100) in the power hardware in the loop platform under blackout and blackstart conditions in order to compare both simulation and experimental Power HIL results. Moreover, Power HIL experimental tests would include testing the commercial GFMI under different control schemes to help support the microgrid. This work can be expanded further in order to consider the commercial GFMI operating simultaneously with protection relays. When implemented, this would provide a glimpse into dynamics interactions between both protections and GFMI generation devices under a variety of fault conditions.

3.10. Hardware in the Loop Testing with Relays

Implementing protection systems, protection engineers aim to provide validated systems that operate with reliability, security, speed and selectivity. Testing is necessary to ensure that systems meet performance criteria, but the increasing complexity of interconnected equipment makes comprehensive testing more challenging. The need for increased power grid resilience requires systems capable of delivering realistic and high-fidelity test conditions for a broad range of system configurations.

A feeder fault was tested with HIL relays time overcurrent (TOC) protection that are connect to the OPAL-RT with the NG model in DETL, as show in Figure 85. The simulation is initially started in a grid connected mode, and after the user determines that the simulation is stable, the simulation is switched to an island mode, where the only source in the system is the grid forming inverter. Three SEL 751 relays were connected by analog out connections from the OPAL-RT to the low-level test interface of each relay as show in Figure 85. For the connection in Figure 86, the low-level test interface received voltage and current point on wave data from the OPAL-RT simulation. Only the current measurements are used to determine if a fault is in a relays zone of protection. As shown in Figure 87, a phase ABC to ground (ABCG) fault was placed to the left of R2 to test the relay setting. Table 10 in Section 3.8.1 displays the relay settings that were calculated and then deployed to the relays (R1, R2, and R3). For this test we want R2 to try and clear the fault and R1 and R3 not operate unless R2 fails to clear the fault.

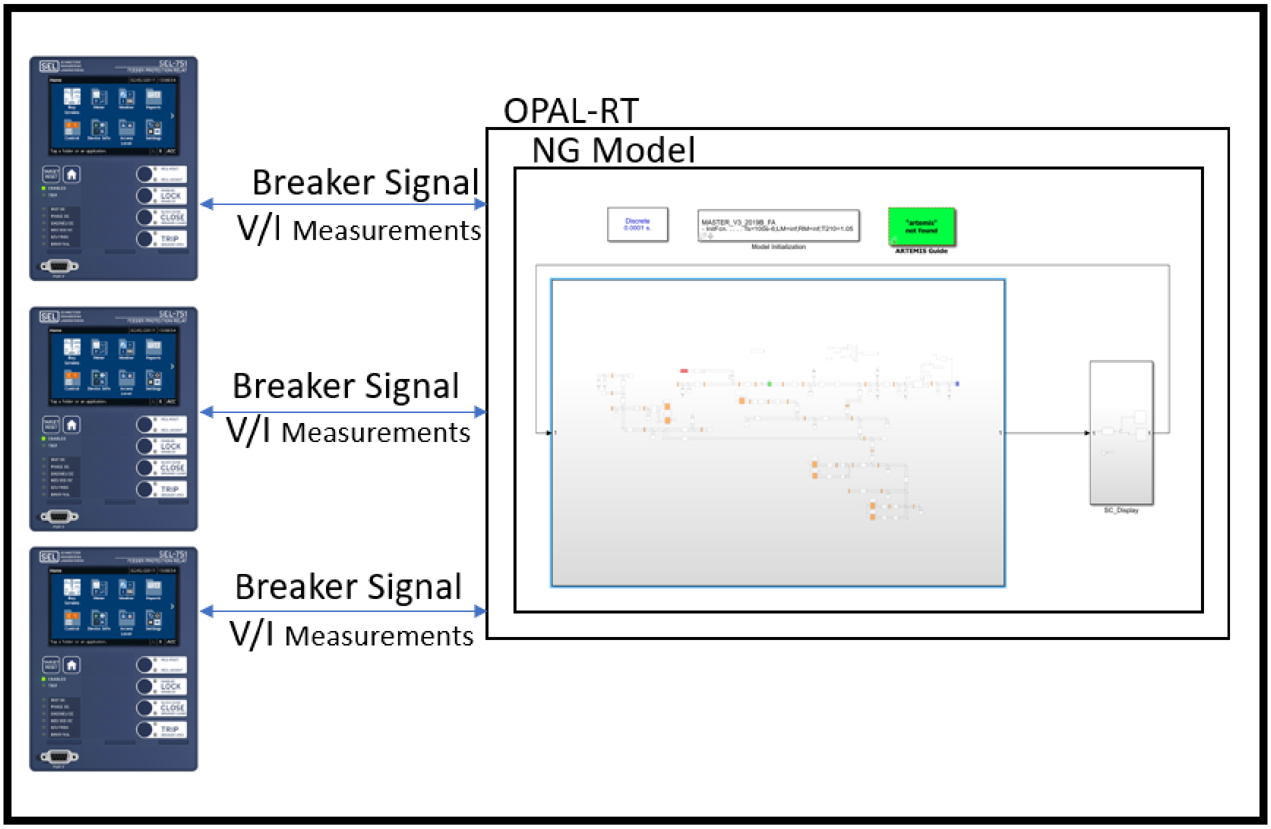

Figure 85. NG HIL Configuration

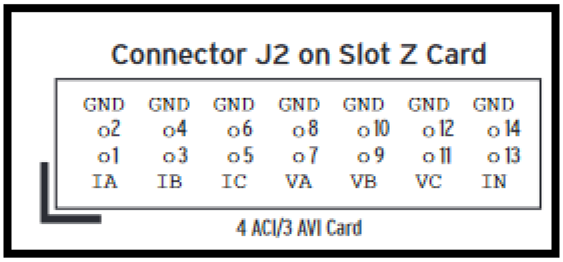

Connector J2 on Slot Z Card

GND	GND	GND	GND	GND	GND	GND
o2	o4	o6	o8	o10	o12	o14
o1	o3	o5	o7	o9	o11	o13
IA	IB	IC	VA	VB	VC	IN

4 ACI/3 AVI Card

Figure 86. SEL 751 Low-Level Test Interface.

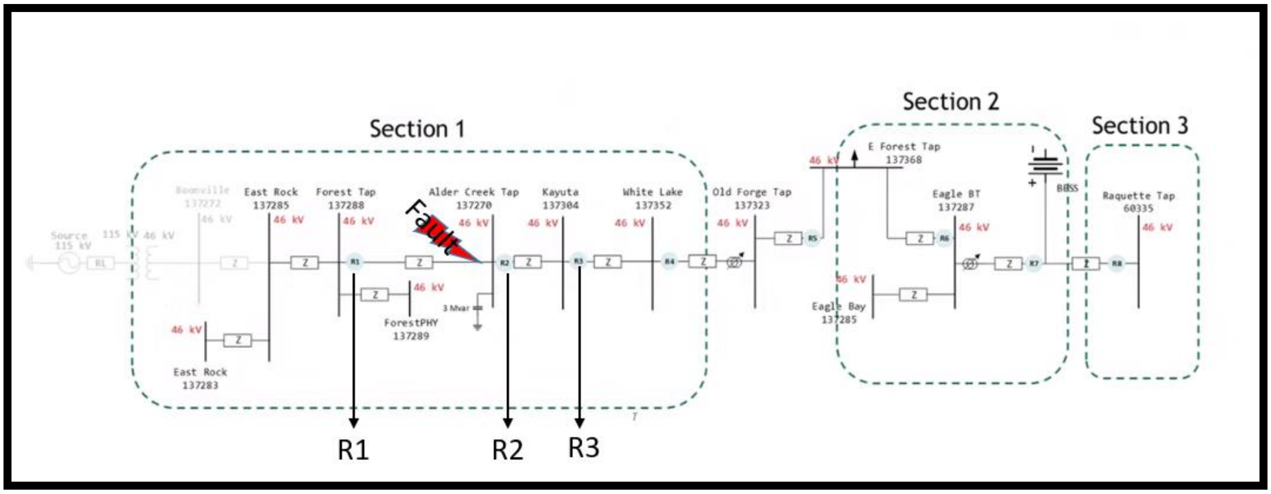

Figure 87. Relays and Fault Location for HIL Testing.

Figure 88 shows the relay locations and the fault location. The fault for test A was applied at 68.76 seconds into the simulation after the user had determined that the simulation was stable. Figure 89 shows the results for Test A post-processing the simulation data. R2 successfully detected the fault and tried to clear it. The relays each have a 3 shot reclose, as shown in Figure 89, and after that they would lock out in an open state. Out101 on the relays was used to send the open/close signal back into the OPAL-RT simulation. Figure 90 is event capture data from the SEL 751 relay that represents R2 in the HIL simulation, for the last reclose operation. During normal system conditions the trip signal remains low and Out101 will remain high. The Out101 contact on the SEL 751 is monitored by the OPAL-RT simulation with an analog input signal back into the simulation as shown in Figure 85, to control the simulation breaker. A signal greater than 1.1 keeps the simulation breaker closed and a signal less than 1 opens the breaker. Once a trip signal is issued it takes 8.3 microseconds for the Out101 contact to drop out and an additional 2 cycles for the current to go to zero as shown in Figure 90.

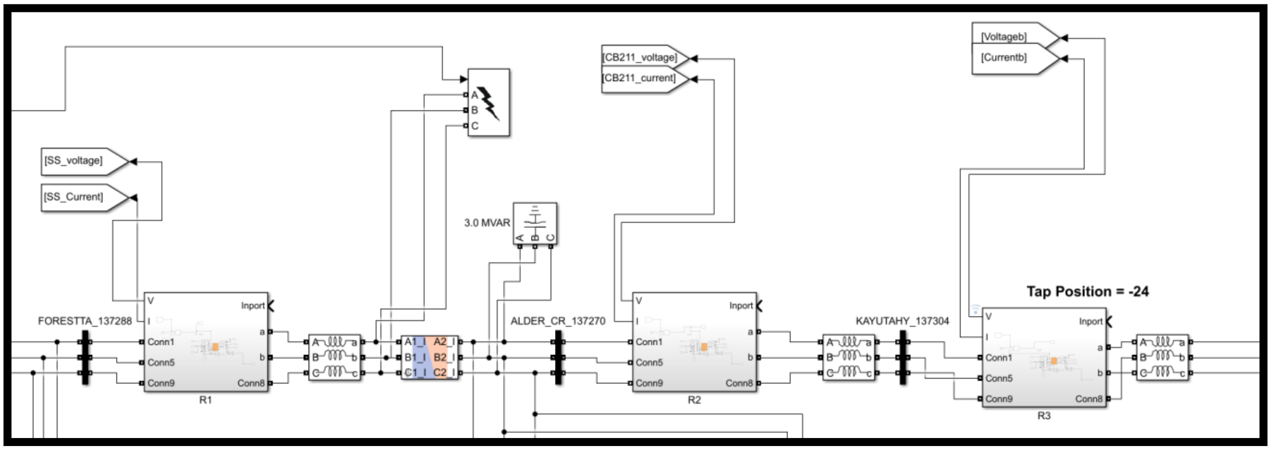

Figure 88. Relays and Fault Location in Simulink/OPAL-RT NG.

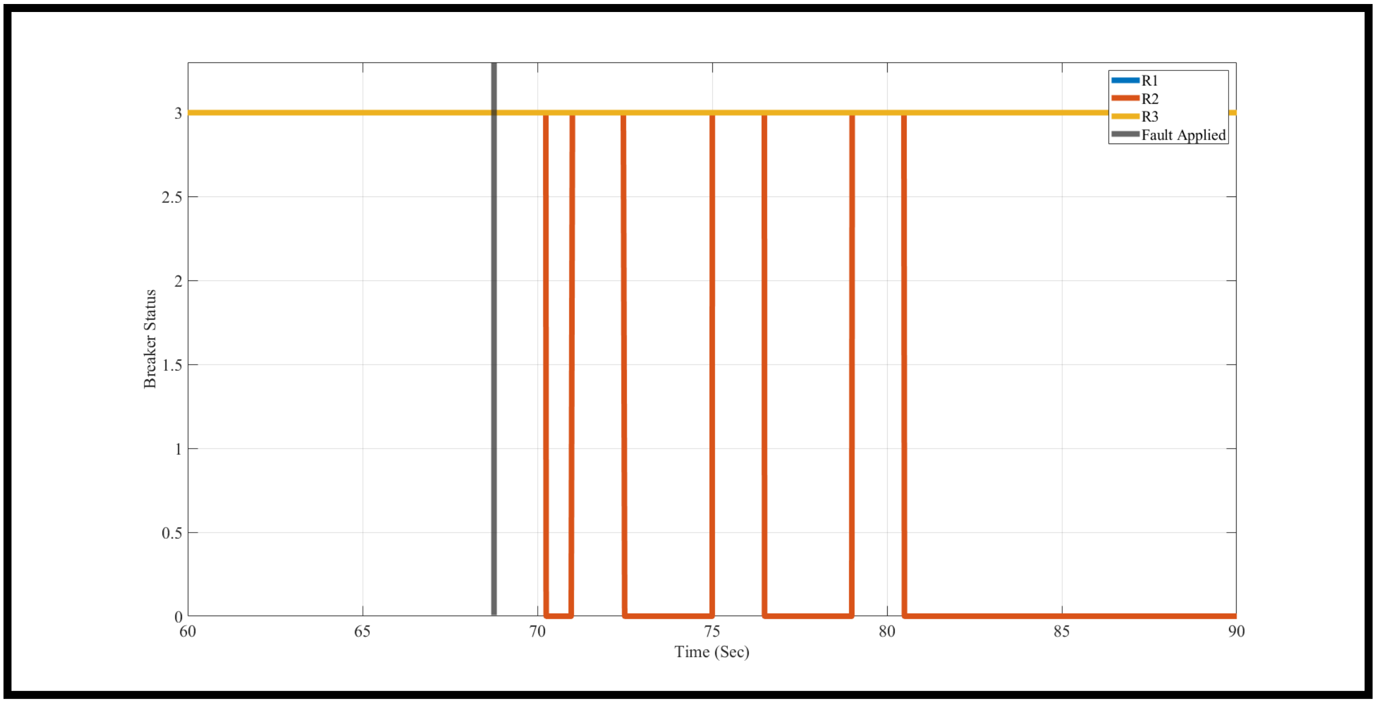

Figure 89. Test A HIL Results

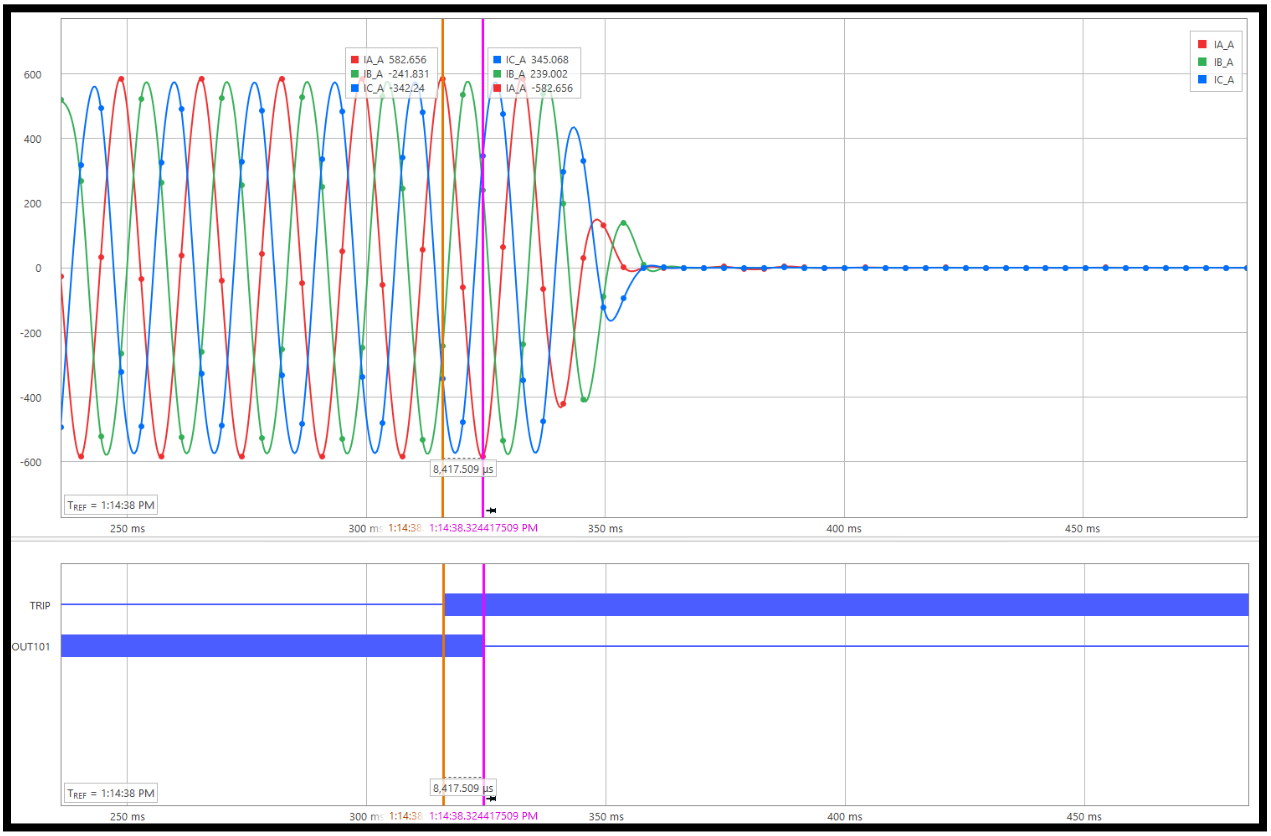

Figure 90. Test A SEL 751 Relay Event Capture Results.

A second fault was tested with HIL relays TOC protection that are connected to the OPAL-RT. An AG fault was placed to the left of R2 to test the relay setting. For this test we want R2 to try and clear the fault, and R1 and R3 not operate unless R2 fails to clear the fault.

The fault for Test B was applied at 44.976 seconds into the simulation after the user had determined that the simulation was stable. Figure 91 shows the results for Test B post-processing the simulation data. R2 successfully detected the fault and tried to clear it. The relays each have a 3 shot reclose, as shown in Figure 91, and after that they would lock out in an open state. Out101 on the relays was used to send the open/close signal back into the OPAL-RT simulation. Figure 92 is event capture data from the SEL 751 relay that represents R2 in the HIL simulation, for the last reclose operation. During normal system conditions the trip signal remains low and Out101 will remain high. Once a trip signal is issued it takes 8.3 microseconds for the Out101 contact to drop out and an additional 2 cycles for the current to go to zero as shown in Figure 92.

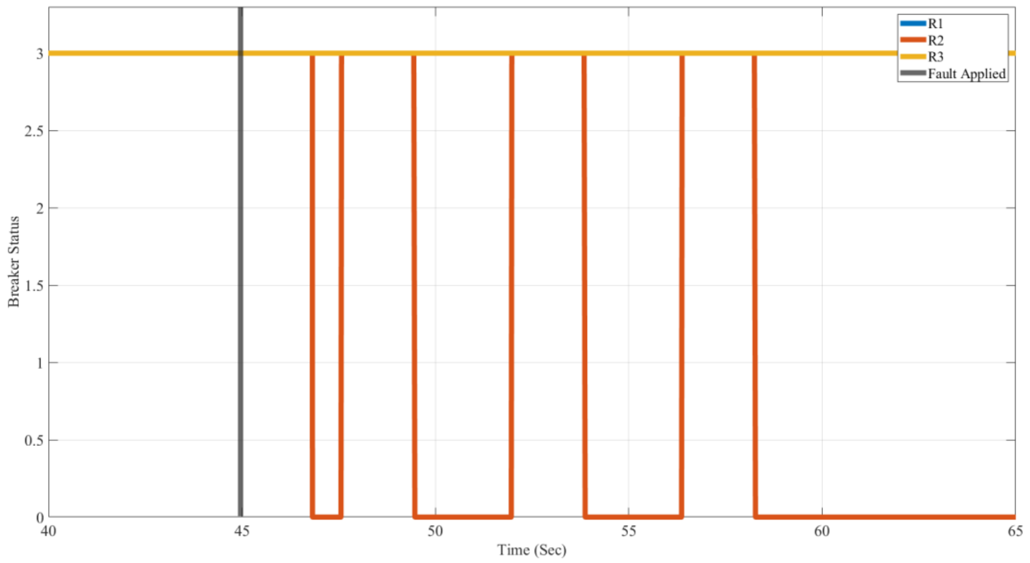

Figure 91. Test B AG Fault Test NG results

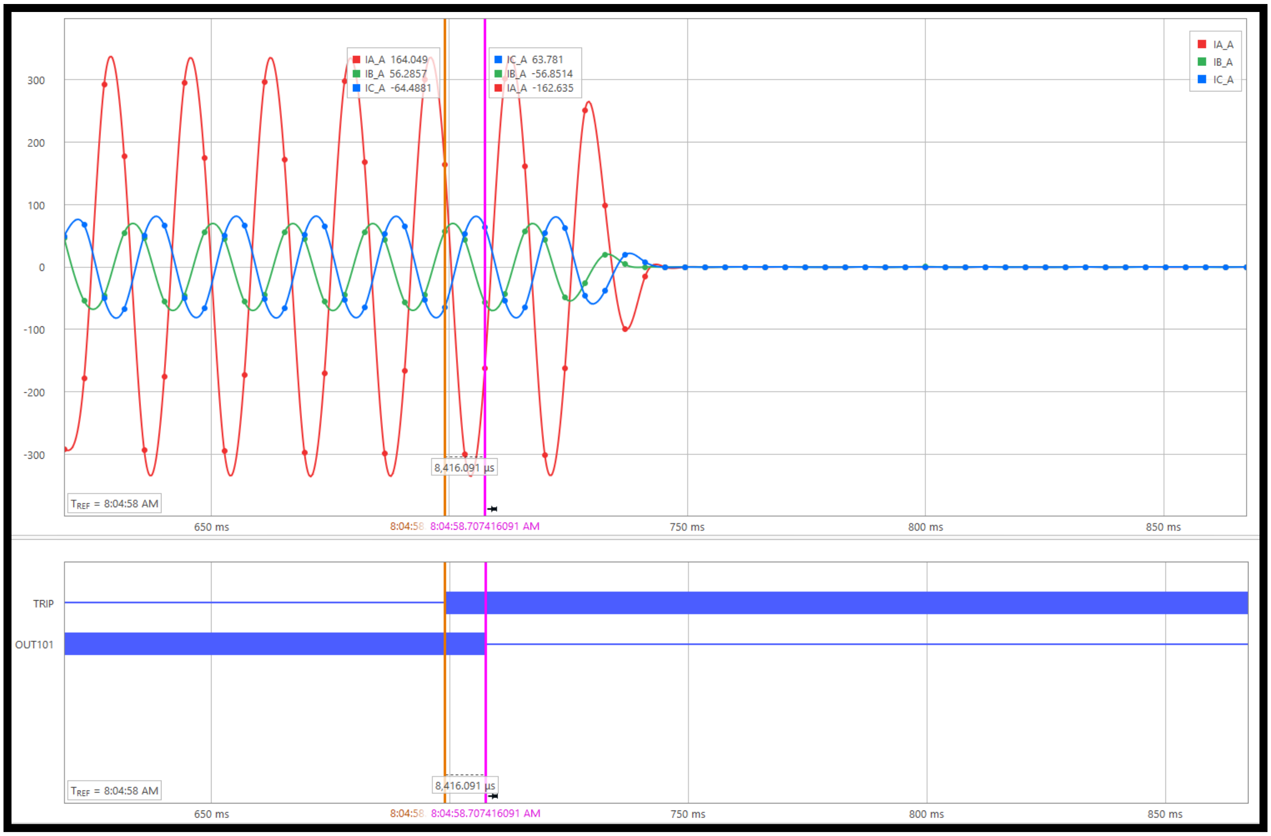

Figure 92. Test B SEL 751 Relay Event Capture Results

These results demonstrate that the NG model feeder was faulted in two separate locations and that the HIL relays using TOC protection that are connect to the OPAL-RT operated as designed. This work can be expanded further in order to consider the commercial GFMI operating simultaneously with protection relays using other types of protection. This would allow a protection engineer to design a systems that operates with reliability, security, speed and selectivity under a larger number of system conditions.

3.11. Conclusions and Next Steps

This hardware demonstration is working to overcome some of the barriers to clean resilience nodes by performing detailed analysis of the implementation. This includes developing grid-forming inverter models, conducting experimental fault testing on grid-forming inverters in the lab, developing adaptive protection schemes for inverter-based microgrids, and performing grounding and black-start studies. The methods are verified using hardware-in-the-loop testing of the control schemes and protection system. While it was shown that this very large battery system can provide enough power to black start the Central Adirondack Resiliency Microgrid Project and provide enough fault current for the protection system, future research could investigate additional methods to provide similar level of resilience with advanced protection methods that may not require as large of a battery. Future work could also investigate how to add customer-owned generation and backup systems into the microgrid controls and protection, and how to incorporate clean resilience nodes into meshed systems like downtown secondary networks. Work is ongoing with National Grid to build this resilience node in collaboration with Sandia for EMT modeling and protection testing.

REFERENCES

[1] B. Obama, *Presidential Policy Directive 21: Critical Infrastructure Security and Resilience (PPD-21),* Washington, D.C.: Executive Office of the President, 2013.

[2] National Academies of Sciences, Engineering, and Medicine, "Enhancing the Resilience of the Nation's Electricity System," National Academies Press, Washington, D.C., 2017.

[3] S. M. Rinaldi, J. P. Peerenboom and T. K. Kelly, "Identifying, understanding, and analyzing critical infrastructure interdependencies," *IEEE Control Systems Magazine,* vol. 21, no. 6, pp. 11-25, 2001.

[4] A. Castillo, C. Murphy, M. B. DeMenno, R. Jeffers, K. Jones, A. Staid, V. Vargas, B. Knueven and S. Ericson, "Resilience Metrics for Informing Decisions Associated with the Planning and Operation of the North American Energy System (SAND2020-11292)," Sandia National Laboratories, Albuquerque, 2020.

[5] Y. Y. Haimes, "On the Definition of Resilience in Systems," *Risk Analysis,* vol. 29, no. 4, pp. 498-501, 2009.

[6] H. Willis and K. Loa, "Measuring the Resilience of Energy Distribution Systems," RAND Corporation, Santa Monica, 2015.

[7] P. Gasser, P. Lustenberger, M. Cinelli, W. Kim, M. Spada, P. Burgherr, S. Hirschberg, B. Stojadinovic and T. Y. Sun, "A review on resilience assessment of energy systems," *Sustainable and Resilient Infrastructure,* vol. https://doi.org/10.1080/23789689.2019.1610600, 2019.

[8] R. Francis and B. Bekera, "A metric and frameworks for resilience analysis of engineered and infrastructure systems," *Reliability Engineering and System Safety,* vol. 121, pp. 90-103, 2014.

[9] D. V. Rosowsky, "Defining Resilience," *Sustainable and Resilient Infrastructure,* vol. 5, no. 3, pp. 125-130, 2020.

[10] C. Holling, "Resilience and stability of ecological systems.," *Annual Review of Ecology and Systematic,* vol. 4, pp. 1-23, 1973.

[11] S. W. Gilbert, "Disaster Resilience: A Guide to the Literature," National Institute of Standards and Technology, Washington, D.C., 2010.

[12] S. Hosseini, K. Barker and J. E. Ramirez-Marquez, "A review of definitions and measures of system resilience," *Reliability Engineering and System Safety,* vol. 145, pp. 47-61, 2016.

[13] I. Linkov and J. M. Palma-Oliveira, "An Introduction to Resilience for Critical Infrastructures," in *Resilience and Risk: Methods and Application in Environment, Cyber and Social Domains*, Dordrecht, Springer, 2017, pp. 3-20.

[14] M. J. Reno, S. Brahma, A. Bidram, and M. E. Ropp, "Influence of Inverter-Based Resources on Microgrid Protection: Part 1: Microgrids in Radial Distribution Systems," IEEE Power and Energy Magazine, 2021.

[15] M. E. Ropp and M. J. Reno, "Influence of Inverter-Based Resources on Microgrid Protection: Part 2: Secondary Networks and Microgrid Protection," IEEE Power and Energy Magazine, 2021.

[16] T. Patel, P. Gadde, S. Brahma, J. Hernandez-Alvidrez, and M. J. Reno, "Real-time Microgrid Test Bed for Protection and Resiliency Studies," IEEE North American Power Symposium (NAPS), 2021.

[17] S. S. Venkata, M. J. Reno, W. Bower, S. Manson, J. Reilly and G. W. Sey Jr. "Microgrid Protection: Advancing the State of the Art," Sandia National Laboratories, SAND2019-3167, 2019.

[18] S. Hossain-McKenzie, E. C. Piesciorovsky, M. J. Reno, and J. C. Hambrick, "Microgrid Fault Location: Challenges and Solutions," Sandia National Laboratories, SAND2018-6745, 2018.

[19] T. Patel, S. Brahma, J. Hernandez-Alvidrez, and M. J. Reno, "Adaptive Protection Scheme for a Real-World Microgrid with 100% Inverter-Based Resources," IEEE Kansas Power and Energy Conference (KPEC), 2020.

[20] B. P. Poudel, A. Bidram, M. J. Reno, and A. Summers, "Zonal Machine Learning-based Protection for Distribution Systems", IEEE Access, 2022.

[21] J. A. Azzolini, N. S. Gurule, R. Darbali-Zamora, and M. J. Reno, "Analyzing Hosting Capacity Protection Constraints Under Time-Varying PV Inverter Fault Response", IEEE Photovoltaic Specialists Conference (PVSC), 2022.

[22] J. Seuss, M. J. Reno, R. J. Broderick, and S. Grijalva, " Determining the Impact of Steady-State PV Fault Current Injections on Distribution Protection," Sandia National Laboratories, SAND2017-4955, 2017.

[23] J. Seuss, M. J. Reno, R. J. Broderick, and S. Grijalva, "Maximum PV Size Limited by the Impact to Distribution Protection," IEEE Photovoltaic Specialists Conference, New Orleans, LA, 2015.

[24] F. Wilches-Bernal. A. Bidram, M. J. Reno, J. Hernandez-Alvidrez, P. Barba, B. Reimer, R. Montoya, C. Carr, and O. Lavrova "A Survey of Traveling Wave Protection Schemes in Electric Power Systems" IEEE Access, 2021.

[25] M. Jiménez Aparicio, S. Grijalva, and M. J. Reno, "Fast Fault Location Method for a Distribution System with High Penetration of PV," Hawaii International Conference on System Sciences (HICSS), 2021.

[26] R. C. Matthews, T. R. Patel, A. Summers, M. J. Reno, and S. Hossain-McKenzie, "Per-Phase and 3-Phase Optimal Coordination of Directional Overcurrent Relays Using Genetic Algorithm," Energies, 2021.

[27] A. K. Summers, R. C. Matthews, T. Patel, and M. J. Reno, "Power System Protection Parameter Sensitivity Analysis with Integrated Inverter Based Resources", IEEE Photovoltaic Specialists Conference (PVSC), 2021.

[28] N. S. Gurule, J. Hernandez-Alvidrez, M. J. Reno, and J. Flicker, "Multiple Inverter Microgrid Experimental Fault Testing", IEEE Photovoltaic Specialists Conference (PVSC), 2022.

[29] J. Hernández-Alvídrez, N. S. Gurule, R. Darbali-Zamora, M. J. Reno, and J. D. Flicker, "Modeling Grid-Forming Inverters Dynamics Under Ground Fault Scenarios Using Experimental Data From Commercially Available Equipment", IEEE Photovoltaic Specialists Conference (PVSC), 2021.

[30] N. S. Gurule, J. A. Azzolini, R. Darbali-Zamora, and M. J. Reno, "Impact of Grid Support Functionality on PV Inverter Response to Faults", IEEE Photovoltaic Specialists Conference (PVSC), 2021.

[31] N. S. Gurule, J. Hernandez-Alvidrez, R. Darbali-Zamora, M. J. Reno, and J. D. Flicker, "Experimental Evaluation of Grid-Forming Inverters Under Unbalanced and Fault Conditions," IEEE Industrial Electronics Conference (IECON), 2020.

[32] R. Darbali-Zamora, J. Hernandez-Alvidrez, A. Summers, N. S. Gurule, M. J. Reno, and J Johnson, "Distribution Feeder Fault Comparison Utilizing a Real-Time Power Hardware-in-the-Loop Approach for Photovoltaic Systems Applications," IEEE Photovoltaic Specialists Conference (PVSC), 2019.

[33] N. S. Gurule, J. Hernandez-Alvidrez, M. J. Reno, A. Summers, S. Gonzalez, and J. Flicker, "Grid-forming Inverter Experimental Testing of Fault Current Contributions," IEEE Photovoltaic Specialists Conference (PVSC), 2019.
[34] S. Gonzalez, N. Gurule, M. J. Reno, and J. Johnson "Fault Current Experimental Results of Photovoltaic Inverters Operating with Grid-Support Functionality," IEEE Photovoltaic Specialists Conference (PVSC), 2018.
[35] J. Alvidrez, A. Summers, N. Pragallapati, M. J. Reno, S. Ranade, J. Johnson, S. Brahma, and J. Quiroz "PV-Inverter Dynamic Model Validation and Comparison Under Fault Scenarios Using a Power Hardware-in-the-Loop Testbed," IEEE Photovoltaic Specialists Conference (PVSC), 2018.

DISTRIBUTION

Email—Internal

Name	Org.	Sandia Email Address
Robert Broderick	8812	rbroder@sandia.gov
Summer Ferreira	8812	srferre@sandia.gov
Matthew J. Reno	8813	mjreno@sandia.gov
Michael Ropp	8813	meropp@sandia.gov
Ujjwol Tamrakar,	8811	utamrak@sandia.gov
Javier Hernandez Alvidrez	8813	jherna4@sandia.gov
Rachid Darbali-Zamora	8812	rdarbal@sandia.gov
Adam Summer	8813	asummer@sandia.gov
Technical Library	01977	sanddocs@sandia.gov

Email—External [redacted]

Name	Company Email Address	Company Name
David Lovelady	david.lovelady@nationalgrid.com	National Grid
E. Louis Seiter	edward.seiter@nationalgrid.com	National Grid
Phil Barker	pbarker@novaenergyspecialists.com	Nova Energy Specialists